Université de Montréal

Optimization and validation of a new 3D-US imaging robot to detect, localize and quantify lower limb arterial stenoses

par
Marie-Ange Janvier

Institut de génie biomédical
Faculté de Médecine

Thèse présentée à la Faculté des études supérieures et postdoctorales
en vue de l'obtention du grade de Philosophiae Doctor (Ph.D.)
en génie biomédical

Octobre, 2010

Université de Montréal

Faculté des études supérieures et postdoctorales

Cette thèse intitulée:

Optimisation and validation of a new 3D-US imaging robot to detect, localize and quantify lower limb arterial stenoses

présentée par :

Marie-Ange Janvier

a été évaluée par un jury composé des personnes suivantes :

Rick Hoge, président-rapporteur

Guy Cloutier, directeur de recherche

Gilles Soulez, co-directeur de recherche

Farida Chériet, membre du jury

Ilian Bonev, examinateur externe

Jean-François Pflieger, représentant du doyen de la FES

Résumé

L'athérosclérose est une maladie qui cause, par l'accumulation de plaques lipidiques, le durcissement de la paroi des artères et le rétrécissement de la lumière. Ces lésions sont généralement localisées sur les segments artériels coronariens, carotidiens, aortiques, rénaux, digestifs et périphériques. En ce qui concerne l'atteinte périphérique, celle des membres inférieurs est particulièrement fréquente. En effet, la sévérité de ces lésions artérielles est souvent évaluée par le degré d'une sténose (réduction >50 % du diamètre de la lumière) en angiographie, imagerie par résonnance magnétique (IRM), tomodensitométrie ou échographie. Cependant, pour planifier une intervention chirurgicale, une représentation géométrique artérielle 3D est notamment préférable. Les méthodes d'imagerie par coupe (IRM et tomodensitométrie) sont très performantes pour générer une imagerie tridimensionnelle de bonne qualité mais leurs utilisations sont dispendieuses et invasives pour les patients.

L'échographie 3D peut constituer une avenue très prometteuse en imagerie pour la localisation et la quantification des sténoses. Cette modalité d'imagerie offre des avantages distincts tels la commodité, des coûts peu élevés pour un diagnostic non invasif (sans irradiation ni agent de contraste néphrotoxique) et aussi l'option d'analyse en Doppler pour quantifier le flux sanguin. Étant donné que les robots médicaux ont déjà été utilisés avec succès en chirurgie et en orthopédie, notre équipe a conçu un nouveau système robotique d'échographie 3D pour détecter et quantifier les sténoses des membres inférieurs. Avec cette nouvelle technologie, un radiologue fait l'apprentissage manuel au robot d'un balayage échographique du vaisseau concerné. Par la suite, le robot répète à très haute précision la trajectoire apprise, contrôle simultanément le processus d'acquisition d'images échographiques à un pas d'échantillonnage constant et conserve de façon sécuritaire la force appliquée par la sonde sur la peau du patient. Par conséquent, la reconstruction d'une géométrie artérielle 3D des membres inférieurs à partir de ce système pourrait permettre une localisation et une quantification des sténoses à très grande fiabilité. L'objectif de ce projet de recherche consistait donc à valider et optimiser ce système robotisé d'imagerie échographique 3D.

La fiabilité d'une géométrie reconstruite en 3D à partir d'un système référentiel robotique dépend beaucoup de la précision du positionnement et de la procédure de calibration. De ce fait, la précision pour le positionnement du bras robotique fut évaluée à travers son espace de travail avec un fantôme spécialement conçu pour simuler la configuration des artères des membres inférieurs (article 1 - chapitre 3). De plus, un fantôme de fils croisés en forme de Z a été conçu pour assurer une calibration précise du système robotique (article 2 - chapitre 4). Ces méthodes optimales ont été utilisées pour valider le système pour l'application clinique et trouver la transformation qui convertit les coordonnées de l'image échographique 2D dans le référentiel cartésien du bras robotisé. À partir de ces résultats, tout objet balayé par le système robotique peut être caractérisé pour une reconstruction 3D adéquate.

Des fantômes vasculaires compatibles avec plusieurs modalités d'imagerie ont été utilisés pour simuler différentes représentations artérielles des membres inférieurs (article 2 - chapitre 4, article 3 - chapitre 5). La validation des géométries reconstruites a été effectuée à l`aide d`analyses comparatives. La précision pour localiser et quantifier les sténoses avec ce système robotisé d'imagerie échographique 3D a aussi été déterminée. Ces évaluations ont été réalisées *in vivo* pour percevoir le potentiel de l'utilisation d'un tel système en clinique (article 3- chapitre 5).

Mots-clés : Système d'échographie 3D, sténoses, calibration, robotique médicale, fantôme de calibration, maladies artérielles périphériques, fantômes vasculaires, athérosclérose

Abstract

Atherosclerosis is a disease caused by the accumulation of lipid deposits inducing the remodeling and hardening of the vessel wall, which leads to a progressive narrowing of arteries. These lesions are generally located on the coronary, carotid, aortic, renal, digestive and peripheral arteries. With regards to peripheral vessels, lower limb arteries are frequently affected. The severity of arterial lesions are evaluated by the stenosis degree (reduction > 50.0 % of the lumen diameter) using angiography, magnetic resonance angiography (MRA), computed tomography (CT) and ultrasound (US). However, to plan a surgical therapeutic intervention, a 3D arterial geometric representation is notably preferable. Imaging methods such as MRA and CT are very efficient to generate a three-dimensional imaging of good quality even though their use is expensive and invasive for patients.

3D-ultrasound can be perceived as a promising avenue in imaging for the location and the quantification of stenoses. This non invasive, non allergic (i.e, nephrotoxic contrast agent) and non-radioactive imaging modality offers distinct advantages in convenience, low cost and also multiple diagnostic options to quantify blood flow in Doppler. Since medical robots already have been used with success in surgery and orthopedics, our team has conceived a new medical 3D-US robotic imaging system to localize and quantify arterial stenoses in lower limb vessels. With this new technology, a clinician manually teaches the robotic arm the scanning path. Then, the robotic arm repeats with high precision the taught trajectory and controls simultaneously the ultrasound image acquisition process at even sampling and preserves safely the force applied by the US probe. Consequently, the reconstruction of a lower limb arterial geometry in 3D with this system could allow the location and quantification of stenoses with high accuracy. The objective of this research project consisted in validating and optimizing this 3D-ultrasound imaging robotic system.

The reliability of a 3D reconstructed geometry obtained with 2D-US images captured with a robotic system depends considerably on the positioning accuracy and the calibration procedure. Thus, the positioning accuracy of the robotic arm was evaluated in the workspace with a lower limb-mimicking phantom design (article 1 - chapter 3). In

addition, a Z-phantom was designed to assure a precise calibration of the robotic system. These optimal methods were used to validate the system for the clinical application and to find the transformation which converts image coordinates of a 2D-ultrasound image into the robotic arm referential. From these results, all objects scanned by the robotic system can be adequately reconstructed in 3D.

Multimodal imaging vascular phantoms of lower limb arteries were used to evaluate the accuracy of the 3D representations (article 2 - chapter 4, article 3 - chapter 5). The validation of the reconstructed geometry with this system was performed by comparing surface points with the manufacturing vascular phantom file surface points. The accuracy to localize and quantify stenoses with the 3D-ultrasound robotic imaging system was also determined. These same evaluations were analyzed *in vivo* to perceive the feasibility of the study.

Keywords: 3D-US system, stenoses, calibration, medical robotics, calibration phantom, peripheral arterial diseases, vascular phantom, atherosclerosis

Table of contents

List of tables

List of figures

List of appendices

List of abbreviations

1.5D	One and a half dimensions
2D	Two dimensions
3D	Three dimensions
*	Pondering parameter
α	Pondering parameter
β	Pondering parameter
δ	Pondering parameter
ξ	Pondering parameter
γ	Pondering parameter
ABI	Ankle brachial index
AC	Alternating current
ACE	Angiotensin-converting enzyme
A_{ref}	Reference vessel area (or diameter) in a non diseased zone
$A_{\min}$	Minimal vessel area (or diameter) in a stenotic zone
B	Reconstruction surface
CAD	Coronary artery disease
CAD-file	Computer assisted design file
CCD	Charged coupled device
CT	Computed tomography
CTA	Computed tomography angiography
CVD	Cerebrovascular disease
C_{rms}	Calibration precision
D	Diameter
DC	Direct current
DOF	Degrees of freedom
DSA	Digital subtraction angiography

$E_{i,j,k}$	Surface map reconstruction error in *i, j* and *k* directions
ECST	European carotid surgery trial
EM	Electromagnetic
FDA	Food and drug administration
FOV	Field-of-view
F/T	Force/torque
G	Lower limb mimicking phantom referential coordinate system
G^k	Ground truth position vector of target point *k* from the phantom
I	US image coordinate system
IMT	Intima-media thickness
$\overline{IntDist}$	Inter-distance accuracy
$\overline{IntDist}_{teach}$	Inter-distance accuracy in teach mode
$\overline{IntDist}_{replay}$	Inter-distance accuracy in replay mode
IVUS	Intravascular ultrasonography
IRED	Infra-red emitting diode
L	Robot workspace experimental zones index
L1, L2	Length of the first and second stenoses
LS	Inter-distance length
LDL	Low-density lipoproteins
LED	Light emitting diode
M	Target holes index of a path in a phantom
mg I/ml	Iohexol organic molecule express in terms of the concentration of Iode
$M(i, j, k)$	Surface map points of the reconstructed vessels
MIP	Maximum intensity projection
MPR	Multiplanar reconstruction
MRA	Magnetic resonance angiography

MRI	Magnetic resonance imaging
N	Sample of images
NASCET	North American symptomatic carotid endarterectomy trial
${}^{phantom}offset_{robot-base}$	The position offset of the phantom with respect to the robot base
p	Statistic probability
P	US probe coordinate system
${}^{end-effector}P_{robot-base}$	Position vector of the robot end-effector to its base referential
${}^{phantom}P_{robot-base}$	Position vector of the phantom to the robot-base
${}^{phantom}P^{i,k}_{robot-base}$	Position vector transformed into the phantom referential of target point k for the SP configuration i
${}^{SP}P_{end-effector}$	Translation vector of SP in the end-effector referential
${}^{SP}P_{robot-base}$	Position vector of the SP center of gravity to the robot-base referential
${}^{SP}P^{teach\ \ i,k}_{robot-base}$	Teach position vector with respect to the robot referential of target point k for the SP configuration i
${}^{SP}P^{replay\ \ i,k}_{robot-base}$	Replay position vector with respect to the robot referential of target point k for the SP configuration i
PAD	Peripheral arterial disease
$\overline{Ps}$	Positioning accuracy
PTA	Percutaneous transluminal angioplasty
PVR	Pulse-volume recordings
R	Robot coordinate system
ROI	Region of interest
RMS	Root-mean-square

$\overline{Rpt}$	Teach/replay repeatability
${}^{end-effector}\mathrm{R}_{robot-base}$	Euler rotation matrice that transforms the end-effector orientation into the robot referential
S1, S2	First and second stenoses
S_{area}	Stenosis quantification in area reduction
$S(i, j, k)$	Surface map points of the reference vessel geometry
SP	Spherical pointer
s_x, s_y	Scaling parameters in an image
T	SP calibration configuration positions index
${}^{P}T_{I}$	Calibration transformation of image *I* in US probe *P*
$T_{robot-base}^{phantom}$	Transformation (rotation and translation) of the phantom with respect to the robot-base referential
${}^{R}T_{P}$	Transformation of US probe *P* into the robot referential *R*
$T_{USprobe}^{robot-base}$	Transformation of the US probe with respect to the robot referential
$T_{image}^{USprobe}$	Transformation of the image with respect to the US probe
${}^{z}T_{R}$	Transformation of robot referential *R* into the Z-phantom
TRUS	Trans-rectal ultrasound
URS	Ultrasound robotic scanner
US	Ultrasound
u_k, v_k	Column and row indices for each image *k*
v/v	Volume concentration
x^{B}	Pixel of the 3D surface reconstruction

x_k, y_k ,z_k	Point in the k_{th} US image localized into the Z-phantom referential
Z	Z-phantom coordinate system
σ_i	Standard deviations of the reconstructed points for an US image i
$\sigma^2_{x\,i,j,k}$, $\sigma^2_{y_{i,j,k}}$, $\sigma^2_{z\,i,j,k}$	Variance for SP calibration configuration positions i in the x, y and z directions for the experimental zone j and target point k.
Δ	Similar triangles

To my mother, my true inspiration

'Only God Himself fully appreciates the influence of a Christian mother in the molding of character in her children.'
Billy Graham

Acknowledgments

First and foremost, I want to thank my Lord and Savior Jesus Christ for leading me the opportunity of pursuing a Ph.D. in biomedical engineering, an emerging multidisciplinary field of my highest interest. He has provided me with faith, strength, courage, perseverance and determination to fulfill this work throughout all the challenges faced in this journey. Without His utmost council this work would have never been accomplished.

I am also grateful to Dr. Guy Cloutier, my research supervisor who has welcomed me with open arms into his Laboratory of Biorheology and Medical Ultrasonics (LBUM), has directed my thesis work and has offered financial support. During the past 7 years at the M.Sc. and Ph.D. levels, he has molded me with important research skills, enlightened me to have a broader perspective for my work and encouraged me to have critical thinking. Also, because of the independence he has granted me throughout these years, I have been able to develop a sense of autonomy and confidence to carry any endeavour in my life. In addition, on various occasions he gave me the opportunity to present my work at numerous well renowned national and international conferences.

I am thankful to Dr. Louise Allard who has helped me shaped my research work into applicable contributions. She has invested a considerable amount of time and effort in directing and reviewing my research. In addition to research coordination, Dr Allard provides a framework of commitment and dedication, coupled with utmost kindness, which allowed me to persevere and develop confidence in my abilities.

This project could not have been produced without the collaboration of a multidisciplinary team of experts. I am thankful to Dr. Pascal Bigras and Dr. Simon Lessard for their counsel on robots. They both provided a strong foundation to build my project. I am also thankful to Dr. Gilles Soulez, my co-supervisor, especially for his expertise on the clinical application which was very resourceful and instrumental for my

research work. I am also grateful for his perspective and enthusiasm that were very encouraging throughout the project. Because of all of you, this project has continuity.

I have also much appreciated the collaboration and support of my fellow colleagues past and present at the LBUM laboratory. The numerous discussions shared throughout the international themed dinners have provided me with much perspective on life essentials. These precious moments I will take with me forever. I would like to thank more particularly, Boris Chayer who along with his good humour and remarkable personality has prepared most of the phantoms necessary for my project. I am also indebted to Zhao Qin, Isabelle Renaud, Dr. Claude Kauffmann, Dr. Marie-Hélène Roy Cardinal and Dr. Marianne Fenech for all their support and technical skills that benefited the advancement of my research.

On a personal level, I am grateful to my mother Arnouse, my true inspiration and biggest supporter. Her continual encouragement and love gave me the wind I needed under my wings to fly with a gaze fix at the horizon instead of the shore. Also, I could not have completed this work without the patience and understanding of my sister Florence. Your friendship has helped me grow into a better person. Finally, I want to thank all my other family members and friends that encouraged me throughout this process. Your kind words have given me the support to complete this thesis.

This work was supported in part by the Canadian Institutes of Health Research (CIHR) under grant MOP #53244 and studentship awards from the Fonds de la recherche sur la nature et les technologies du Québec, TD Canada Trust, the Institute of Biomedical Engineering at Université de Montréal, the Quebec Black Medical Association and the End of Study Grant from the Faculty of Graduate and Postgraduate Studies at Université de Montréal.

Chapter 1

Atherosclerosis

Problems are not stop signs, they are guidelines.

Robert H. Schuller

This chapter presents the clinical context behind this thesis. Atherosclerosis disease and its progression into stenotic lesions are first described, while the manifestation of this pathology in lower limb arteries follows. Various diagnostic methods of peripheral arterial disease and common therapies are also discussed. The chapter ends with a short summary.

1.1 Introduction

Cardiovascular diseases are one of the leading causes of death in developed countries and that affect particularly the elderly [1]. These pathologies rank high in terms of cost in health care [2] (both direct and indirect) to the nation's economy as their prevalence is expected to increase with the aging population.

Atherosclerosis is a cardiovascular disease that leads to the hardening and remodelling of the arterial walls due to fatty cells deposition. This process can progressively narrow the lumen and affect the arteries supplying blood to the heart (causing coronary artery disease or CAD), the brain (causing cerebrovascular disease or CVD) and/or the legs (causing peripheral arterial disease or PAD) [3-5]. This pathology is a complex process that involves endothelial dysfunction, lipid metabolic disturbances, platelet activation, thrombosis, oxidative stress production, vascular smooth muscle activation, altered matrix metabolism, remodelling, genetic factors and inflammation [6].

1.2 Pathogenesis of atherosclerosis

Narrowing of arteries caused by atherosclerosis is usually initiated when the intimal endothelium becomes dysfunctional (see Fig. 1.1) [7]. This inner membrane of arteries is

significantly responsible for the vascular equilibrium (i.e., homeostasis). In normal function, the endothelium provides a permeability barrier for nutrient delivery and waste removal, reduces clotting (i.e., coagulation or thrombosis formation) in inflammation (i.e., injury or infection) and finally regulates the vascular tone.

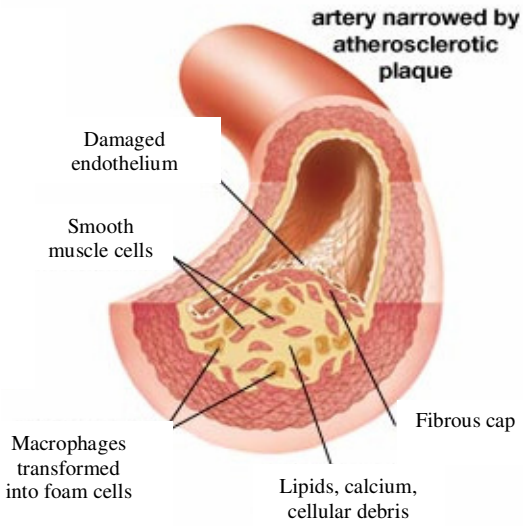

Figure 1.1: Atherosclerosis plaque progression.[1]

Endothelial dysfunction develops frequently in arterial bifurcations and branch locations [6], where disturbed blood flow occurs [7]. Low-density lipoproteins (LDL) (i.e., cholesterol) circulating in the blood stream can easily deposit in the arterial wall or be trapped in the sub endothelial space [4]. When free radicals oxidize cholesterol, the endothelial cells become intoxicated. Cigarette smoking, hypertension, diabetes mellitus and obesity are all, factors that create these toxins [7]. After damages of endothelial cells, atheroprotective mechanisms are triggered and inflammation is signalled [4]. Hence, white blood cell recruitment (i.e., monocytes, macrophages and leukocytes etc.) for massive accumulation of cholesterol are initiated, which starts the process of atherosclerosis at these sites (see Fig. 1.1).

[1] Source: http://s3.images.com/huge.96.481111.JPG (Accessed: 12/06/2009).

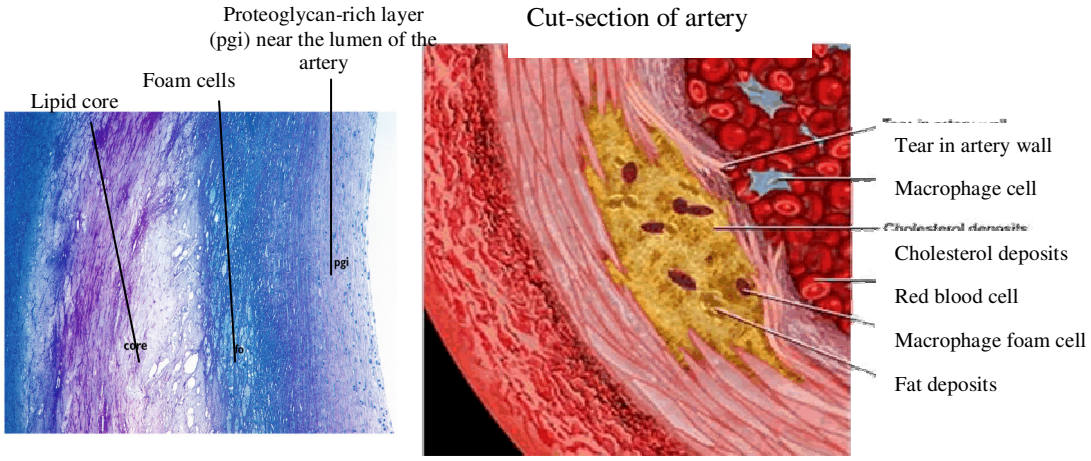

(a) (b)

Figure 1.2: (a) Histology of initial smooth muscle cells trapped into the lipid core of a type IV lesion and macrophage foam cells (fo) overlying the core on the side towards the arterial lumen.[2] (b) Atherosclerosis pathogenesis.[3]

When the white blood cells are ingested with cholesterol, they have a foamy cytoplasm. From that point, they are called foam cells, where they accumulate in the sub endothelial tissue to form an inflammatory lesion referred to as the fatty streak [6, 7]. Foam cells generate growth factors and cytokines that make them become necrotic over time [7, 8]. Cholesterol, foam cells and debris continue to adhere to the necrotic tissue in addition to a large number of smooth muscle cells filled with lipids that multiply and form an extracellular matrix. This is when the fatty streak becomes a highly cellular advanced lesion called the fibroproliferative atheroma (i.e., atheroma plaque). This lesion illustrated in Fig. 1.2a contains a lipid core covered by a fibrous cap that is growing in size [6, 8]. The complete structural disorganization and thickening of the vessel wall is showed on histology hallmarks. Important characteristics of atherosclerosis histological compositions [9] are classified in lesion types I-VIII (see Fig. 1.3).

---

[2] Source: [8] H. C. Stary "Atlas of Atherosclerosis Progression and Regression," Second ed, T. P. P. Group, Ed. London: Richmond House, 2004.
[3] Source : http://www.arnoldehret.org/images/cutsectionofartery.gif (Accessed: 10/05/2010).

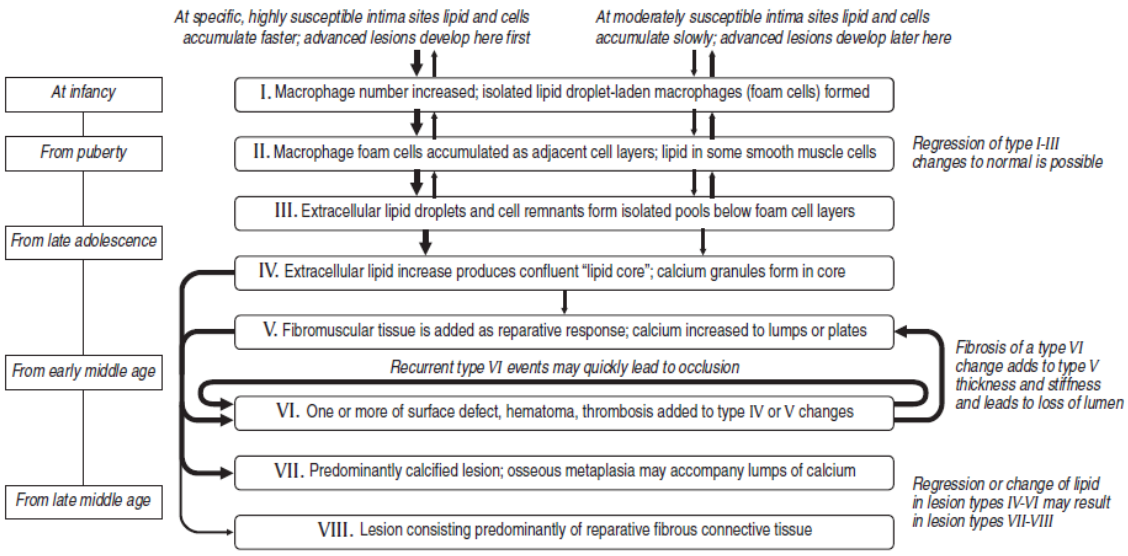

Figure 1.3: Pathways of atherosclerosis progression and regression. The order in which distinct lesion types usually develop is designated with the numerals I to VIII. The diagram lists the main histological characteristics of each sequential step (lesion type). Thick or thin arrows differentiate between the relative ease with which lesions develop in specific locations, or they indicate the relative frequency and importance of a specific pathway section.[4]

Initially, arteries will compensate for atherosclerosis growth by remodelling. Consequently, blood vessels increase in size in order to improve the vascular flow. Nevertheless, the arterial wall hardens and can no longer compensate for atherosclerosis development, thus in advanced lesions, the arterial lumen is often invaded, which narrows and decreases the arterial blood flow. These particular lesions can become more complex and calcification can occur to the atherosclerosis plaque (see Fig. 1.4).

[4] Source : [8] H. C. Stary "Atlas of Atherosclerosis Progression and Regression," Second ed, T. P. P. Group, Ed. London: Richmond House, 2004.

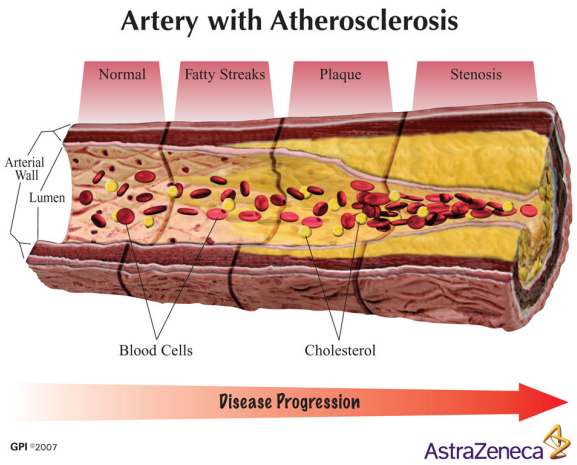

Figure 1.4: Atherosclerosis plaque progression[5]

Severe arterial events can occur if the plaque fibrous cap is disrupted [6] or obstructs the arterial wall (see Fig. 1.4). Plaque rupture can take place through different mechanisms that include inflammation [7, 8]. Exposed necrotic lipid core and subendothelial tissue lead to platelet aggregation. Subsequently, thrombus formation and flow occlusion arise. At this advanced stage, the pathology can cause a stroke or a myocardial infarction and/or limb ischemia.

1.3 Stenotic lesion characterization

Occlusions in arteries are called stenotic lesions (or stenoses). A severe stenosis is defined by clinicians as more than 50.0 % reduction of the arterial diameter. Generally, NASCET (North American Symptomatic Carotid Endarterectomy Trial) and ECST (European Carotid Surgery Trial) guidelines are used by clinicians to quantify carotid stenosis with percentage ratio on angiograms (i.e., images of the lumen artery); this method is also applicable to other arteries and imaging modalities [10-12].

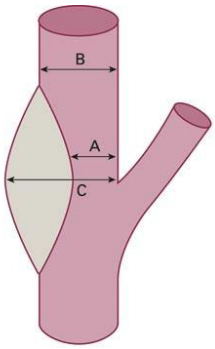

ECST-method: $\frac{C-A}{C}\cdot 100\%$

NASCET-method: $\frac{B-A}{B}\cdot 100\%$

Figure 1.5: In the guidelines to evaluate the severity of stenosis, NASCET and ECST measurement methods are used.[6]

Usually, the numerator is the narrowest diameter difference (i.e., stenosis) for both methods. The denominator is either the distal artery (for NASCET) or the estimated diameter of unseen stenosis outer walls (for ECST) (Fig. 1.5). While both methods are used for different diagnostic imaging technologies, each present their own set of errors. NASCET, the most commonly used technique, is more representative of the luminal narrowing but can underestimate the lesion in case of near occlusions or diffuse atheromatous infiltration [10, 11]. Likewise, ECST has the subjective bias of measuring an unseen artery [10]. Regardless of the method, the degree of stenosis correlates with blood flow velocity and symptoms that can be used to identify the severity of impaired arterial lesions [6, 13].

1.4 Lower limb peripheral arterial diseases

Atherosclerosis is a systematic disease that progresses in most medium-size vessels of the lower extremity, such as the aorto-iliac and infrainguinal system [9, 16-18]. This disease is more prevalent in the femoral and popliteal arteries (80 % - 90 % of symptomatic patients), tibial and peroneal arteries (40 % - 50 % of symptomatic patients), in the aorta and iliac artery (30% of symptomatic patients) [8, 14]. Atherosclerosis mainly develops in

---

[5] Source: http://multivu.prnewswire.com/mnr/uaa/37598/images/37598-hi-Athero_Progression.jpg (Accessed: 10/05/2010)

the arterial system compared to the veins because more oxygen is available in arteries to oxidized cholesterol (see lower limb vessel anatomy in Fig. 1.6). When a cardiovascular event (i.e., myocardial infarction, stroke) occurs in other vascular regions (i.e., coronary and carotid arteries), PAD is often present symptomatically or asymptomatically [3, 7, 15, 16].

Occlusions in lower limb peripheral arteries contribute to diminished blood supply, causing decreased oxygen and nutrient supply in distal tissues and muscles. If occlusions further progress and/or perpetuate, cell injury can cause severe tissue ischemia or furthermore, tissue breakdown which can lead to a cardiovascular event, amputation and even death.

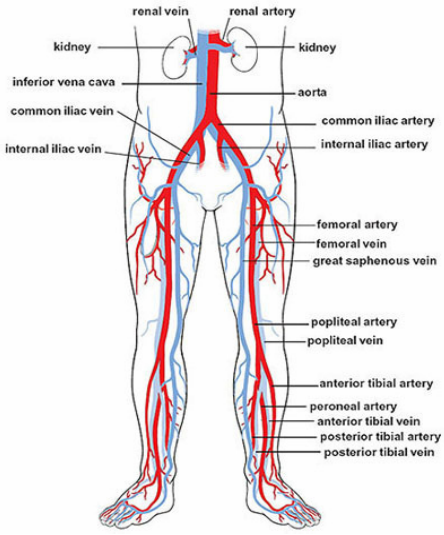

Figure 1.6: Complete anterior view of lower limb peripheral arteries and veins.[7]

1.4.1. Symptoms

Most PAD are diagnosed when severe symptoms are present because in early stages of the disease, they are usually silent [17]. When stenotic lesions are severe, intermittent claudication symptoms may appear in hips, buttocks, calves and arch of the foot and even

---

[6] Source: http://www.tidsskriftet.no/index.php?seks_id=1181296&a=fig&art_id=1181232 (Accessed: 22/07/2009).

[7] Source: http://www.vascular.westcountysurgical.com/images/pad_1.jpg (Accessed: 11/06/2009).

sometimes produce erectile dysfunction in males [7, 18, 19]. Intermittent claudication, the primary perceptible PAD symptom, is defined by leg muscle pain, cramping and fatigue brought on by ambulation or exercise, relieved at rest [8]. The location of the pain is determined by the anatomical level of the disease. A blood flow velocity increase is observed inside the stenotic lesion with flow velocity and blood pressure drops downstream of the lesion. This phenomena is amplified during exertion because of the increase of oxygen consumption requiring more blood inflow. More complex symptoms are involved in case of critical limb ischemia where ischemic symptoms are present at rest. Rest pain, minor and major tissue losses (ulceration) can be observed. In this case, the limb can be mummified with dry black toes or devitalized soft tissues covered by crust (gangrene). Moreover, metabolic abnormalities in the skeletal muscles of the lower extremity can occur [17]. However, in case of chronic disease, an extensive collateralization (i.e., microvascular growth) occurs in the lower limb arteries increasing blood downstream of the lesion. This phenomenon can alleviate the symptoms and is promoted by exercise. With disease progression, obstructions at different levels are observed with a cumulative effect on flow impairment. Thus, symptoms usually surface when one or more vessels have been severely narrowed. To rate the symptom severity, two classification systems are commonly used [20, 21]. In the Rutherford system, mild, moderate and severe claudications are categorized from 1-3 and asymptomatic patient as 0, while categories 4-6 encompass ischemic rest pain, minor to major tissue losses and critical limb ischemia (see Table 1). In the Fontaine system of classification, only 4 grades (0-III) associated with asymptomatic, moderate claudication, ischemic rest pain and critical ischemia (see Table 1) are used. It is important to note that Rutherford's classification is the clinical standard for describing clinical assessment and progress.

Table 1: Classifications of peripheral arterial diseases according to Rutherford categories and Fontaine's grades [21].

Clinical description	Fontaine's grades	Rutherford's categories
Asymptomatic	0	0
Mild claudication	I	1
Moderate claudication	I	2
Severe claudication	I	3
Ischemic rest pain	II	4
Minor tissue loss	III	5
Major tissue loss	III	6

1.4.2. Risk Factors

PAD traditional risk factors are the same as those associated with atherosclerosis in the carotid, coronary and other vascular beds. They specifically include: advanced age, diabetes mellitus, smoking, hyperlipidemia and hypertension. Generally, subjects of 65 years of age or older have higher risk for PAD development [6]. This risk increases approximately 4 times more if subjects smoke cigarettes [6, 7, 22]. In addition, PAD risk is apparently directly proportional to the dose of smoking (i.e., number of packs per year). This association is twice as strong as with coronary artery disease. Certainly, this is the single most important modifiable risk factor for PAD development. Moreover, if subjects have diabetes mellitus, they are 1.5 to 4 times more likely to develop symptomatic or asymptomatic PAD. In addition, they have an associated increase risk of cardiovascular events and premature death [6, 22]. Similarly, an elevated total cholesterol level (i.e., hyperlipidemia) increases 2 times more PAD symptoms. In fact, the prevalence of symptoms was found to be 77 % in patients with known PAD [6]. Finally, hypertension has been linked to 50 % – 92 % of patients with PAD [6]. In this case, an increase risk of stroke

and myocardial infarction independent of other factors exist with these patients [22]. Clearly, all these traditional risk factors can be modified to reduce PAD progression [23].

Non traditional risk factors also have shown to predict the prevalence of PAD. These risks include: race and ethnicity, inflammation, chronic kidney disease, genetics, hypercoagulable states and abnormal waist to hip ratio. However, not much study has been established to clearly outline their specific relationship to PAD. Black and Hispanic populations have shown to be disproportionately prevalent to PAD even after adjustments to traditional risk factors [6, 22, 23]. In addition, elevated levels of inflammatory markers (e.g., leukocytes) have already been observed in patients with atherosclerosis in other arterial systems. However, several studies suggest that high level of inflammatory markers are more specifically associated to PAD in lower limbs [6]. Furthermore, an unknown association of PAD with chronic kidney and severe renal diseases appears to exist independently of the traditional risk factors [6]. For example, PAD patients with chronic kidney disease are at increased risk for critical limb ischemia, while those with severe renal disease are at increase risk for amputation.

Yet, recently, several studies suggested an independent association between PAD and hypercoagulable states or thrombophilia (i.e., increase tendency to develop blood clot due to an abnormality) [6]. In some cases, hemostatic factors seem to be associated with premature atherosclerosis more prominently in PAD progression than for carotid artery disease. Moreover, ongoing reports of genetic predisposition to PAD also seem to suggest increased rates of CVD at an earlier age (i.e., less than 55 years) [6]. Lastly, new reports have found an association between PAD and abdominal obesity. Apparently, an increased waist to hip ratio (more than 0.966) can be associated with a 1.7 time increase risk of PAD [6].

In final analysis, PAD is a systematic atherosclerotic process that is associated with high morbidity and mortality, and significant impairment on the quality of life. However, with all well known traditional and associated risk factors, it remains underdiagnosed and undertreated [24, 25]. Moreover, most previous studies that screened PAD in the primary care settings with risk factors include patients that are already known to have PAD or another associated CVD [25]. Thus, significant benefits could be achieved in detecting

PAD patients with risk factor awareness and enhanced screening. However, a collaborative effort between patients and clinicians is necessary to recognize lower limb symptoms and diagnose PAD appropriately.

1.5 Diagnostic methods

Patients with PAD are principally diagnosed when they report lower limb pain to their clinician. Clinicians first employ questionnaires to assist them in identifying PAD symptoms where the walking distance and the lower extremity pain are evaluated [7]. It is to note that PAD also exists in patients with no evident symptoms. Thus, the first line of investigation with a clinician is usually subjective.

If PAD is suspected after the first consultation, specialized radiologists and/or vascular surgeons are normally referred to examine arterial lesions more specifically. Then, diagnostic approaches able to detect, locate and quantify stenoses in an objective manner are used. Non-invasive screening techniques such as ankle brachial index, tests & exercises and ultrasound (US) imaging are employed to assess PAD severity. To map the entire lower limb vascular tree, common invasive imaging technologies such as digital subtraction angiography (DSA), computed tomography angiography (CTA) and magnetic resonance angiography (MRA) are used [26].

1.5.1 Non-invasive screening methods

1.5.1.1 Ankle brachial index

The ankle brachial index (ABI) is the oldest non-invasive method that can accurately detect the presence and severity of PAD in primary care clinical setting [7, 8, 23, 25-27]. This technique, illustrated in Fig 1.7, is described as the ratio of systolic blood pressures measured at the ankles to the one of arms with a cuff and manometer. A threshold value less than 0.90 is an indicator for PAD.

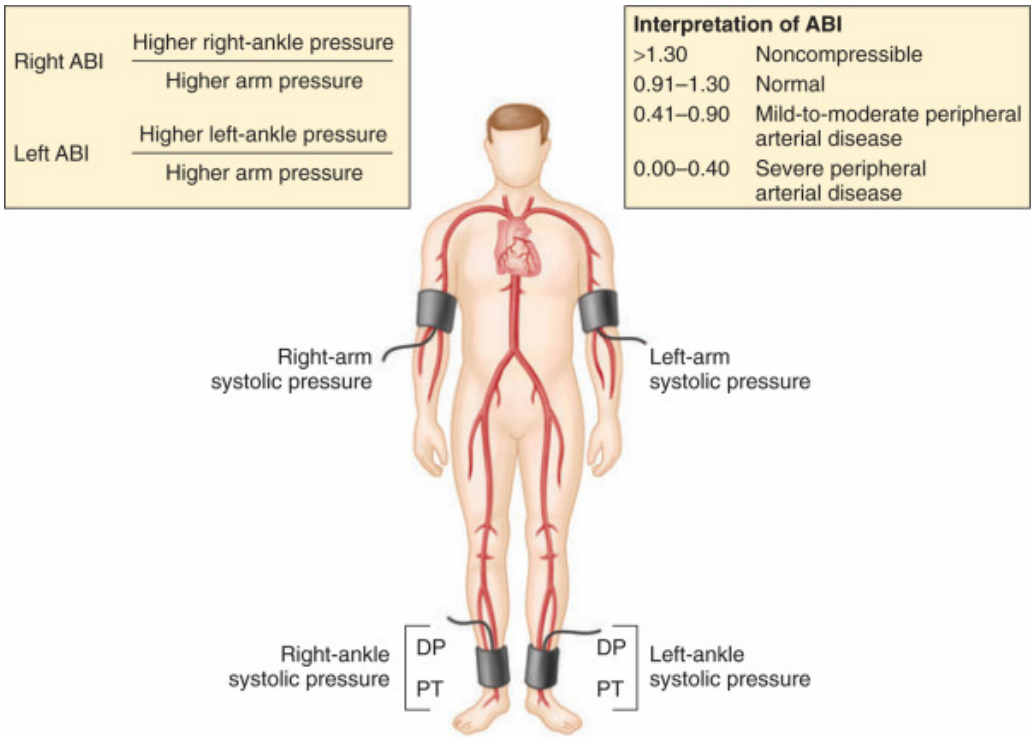

Figure 1.7: Screening of PAD with the ankle-brachial index (ABI) test. (DP = dorsalis pedis, PT = posterior tibial).[8]

ABI is a commonly accepted reference standard for PAD pre-diagnostic because it is sensitive and specific [13]. However, this technique presents limitations to detect PAD when peripheral arteries are heavily calcified. A falsely abnormal or high ABI can occur from arteries that consequently become rigid and non-compressible [7, 23]. ABI cannot diagnose PAD also in aorto-iliac disease, collateralized disease and occlusions for the same reason [28].

1.5.1.2 Tests and exercises

Usually, if the ABI is conclusive, further investigations are performed to localize lesions with either segmental pressure evaluations, pulse volume recordings or treadmill exercise training [7, 8]. For segmental pressures, lower limbs are separated in sections, and then at each level, pressure measurements are assessed (see Fig. 1.8). This approach similar

to the ABI requires a continuous-wave Doppler probe (explained later in section 1.5.1.3) that is placed on the different vessel segments. Stenoses are detected when a decrease of pressure occurs between two consecutive levels or when a discrepancy arises between pressure measurements at the same level of both limbs.

To perform pulse-volume recordings (PVR) at different levels, the same pressure measurement equipment is used and the record of plethysmographic tracing is also performed. Changes in the volume of blood flow are detected in these tracings and severe stenoses are identified when the normal peak velocity ratio (PVR) waveform becomes attenuated. Fig. 1.8 demonstrates PVR test in a patient with a symptomatic PAD on the left side with normal PVR in the right leg and decreased values in the left leg.

PAD diagnosis is also confirmed by demonstrating objectively the functional limitation of lower limbs [26]. If patients have a normal resting study and exertion symptoms, a treadmill exercise training test can be performed. During the procedure, the subject walks on a treadmill at a constant speed with a fix setting or a variable incline. This method is used as well in therapy to monitor effects on initial and absolute claudication distances.

---

[8] Source: http://www.mdconsult.com/das/book/body/148479302-3/0/1492/f4-u1.0-B978-1-4160-2805-550084-7gr1.jpg (Accessed: 08/07/2009).

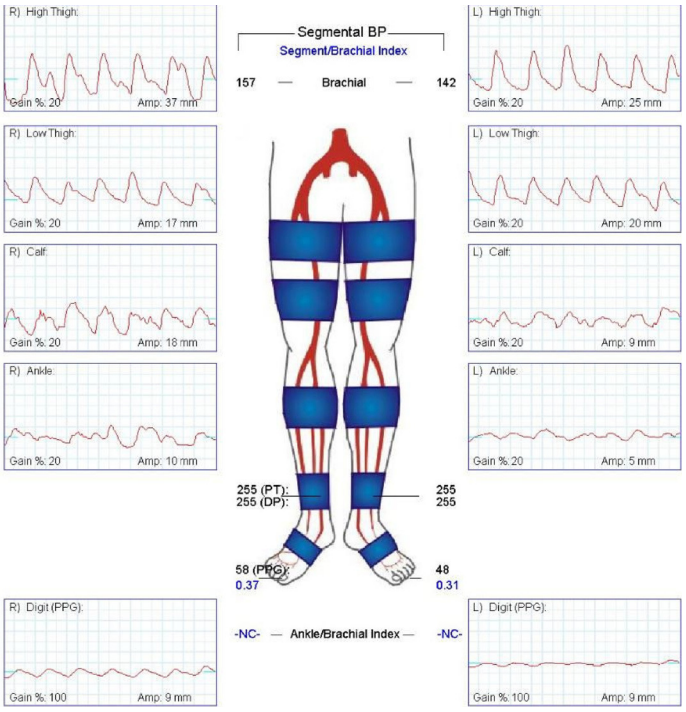

Figure 1.8: Pulse volume recordings of a patient presenting a PAD in its left leg[9].

Altogether, these tests and exercises are available options that are inexpensive and painless to provide a useful non-invasive method that can evaluate patients suspected with PAD when they present limb discomfort. However, all of the above vascular physical examinations have been severely criticized by physicians because they only quantify flow limitation but do not image the occlusive disease itself and its extension. Moreover, the reliability of screening is poorly reproducible, unreliable and difficult to interpret [29]. Thus, other non-invasive testing should be prompt to localize lesions more specifically.

1.5.1.3 Duplex ultrasound (US)

Medical diagnostic ultrasound is a modality that uses the ultrasound energy and the human tissue acoustic properties to produce an image (for further information relative to US see Appendix I). US images are produced from a 'pulse echo' technique that synthesizes a gray-scale 2D tomographic image of tissues based on the mechanical

[9] Source : [26] D. Chan, M. E. Anderson, and B. L. Dolmatch, "Imaging evaluation of lower extremity infrainguinal disease: role of the noninvasive vascular laboratory, computed tomography angiography, and magnetic resonance angiography," *Tech Vasc Interv Radiol,* vol. 13, no. 1, pp. 11-22, Mar, 2010.

interaction of short pulses of high-frequency sound waves and their returning echoes [30]. The whole image data acquisition process is performed from a US system that offers convenient real-time imaging with a transducer in contact with the human body (see Fig. 1.9).

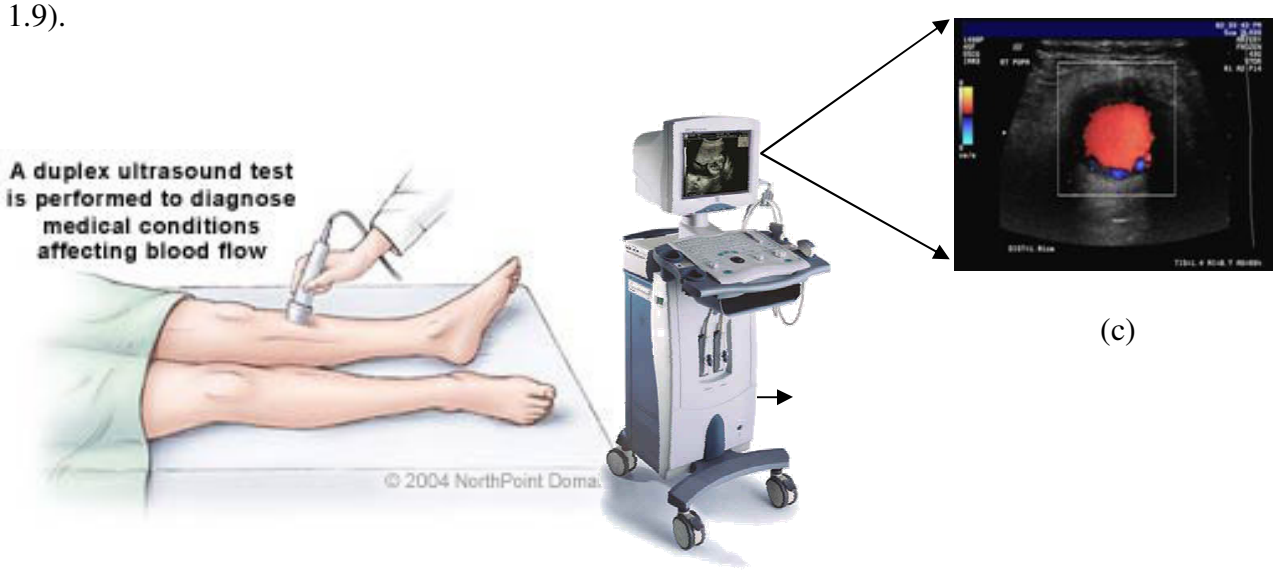

(a) (b) (c)

Figure 1.9: (a) Diagnostic US imaging system. (b) US probe scanning the lower limb (leg). (c) Color Doppler superimposed on a B-mode arterial image in cross-sectional view.[10]

This non-invasive, non-ionizing and low-cost US technology provides physicians with valuable information on vascular stenosis detection for both diagnosis and follow-up purposes. PAD severity could be analysed in multiple modes with options in B-mode, color and power Doppler that facilitate accurate blood flow quantification and localization. B-mode presents the morphology on the atherosclerotic plaque in gray scale imaging [31], and Doppler US estimates the velocity and the direction of moving blood cells based on the frequency shift principle of an US wave [30]. The US imaging system extracts Doppler information in the form of pulsed and continuous wave Doppler to output into a spectral Doppler waveform, color flow and power maps [30].

---

[10] Source: (a) http://www.csd-ultrasound.com/mindray/DP-9900.htm (Accessed: 18/06/2009),
(b) http://www.cardiosmart.org/HeartDisease/CTT.aspx?id=140 (Accessed: 09/07/2009),
(c) http://www.kvu.com.au/Doctor-Information/image012.jpg (Accessed: 29/07/2009).

To identify a stenosis, the spectral Doppler US waveform is often used. This US imaging mode displays the spectrum of flow velocities over time. The normal spectral density waveform is "triphasic" (see Fig. 1.10b). Turbulent flow patterns that depend on the vessel wall characteristics, size and shape of the vessel, and the flow rate are used to detect stenosis [30]. To visualize the vessel anatomy and analyze the blood flow, color flow imaging is often used [30]. This US imaging mode is a form of pulsed wave Doppler, where returning echoes are assigned a color coding representing their flow velocity and direction. This color mapping is superimposed on B-mode images (i.e., Duplex scanning). In this form, semi quantitative assessment of blood flow velocity is provided (see Fig. 1.10a). By convention, shades of red represent flow towards the transducer, and blue away from it. Finally, to detect and interpret subtle and slow blood flow, power Doppler imaging is used. This form of imaging relies on the total strength (amplitude) of the Doppler signal energy and ignores its direction. Thus, this imaging mode is the most sensitive to motion of the blood flow.

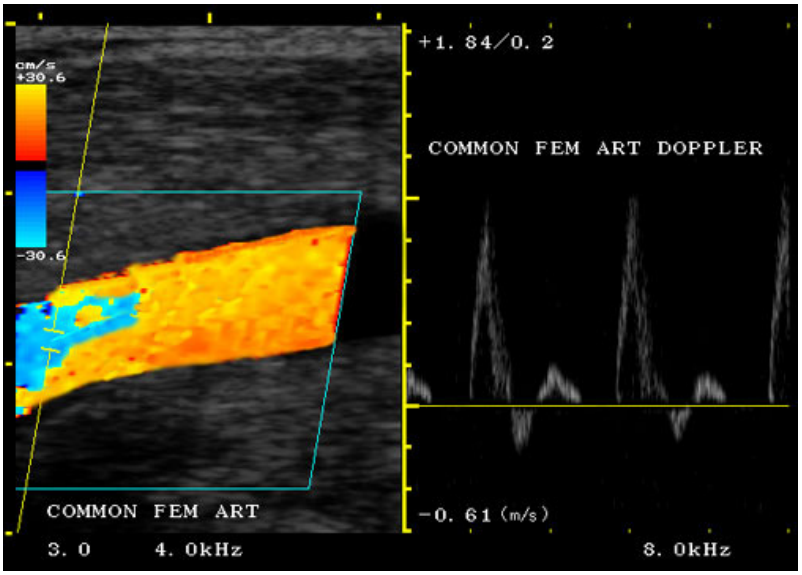

(a) (b)

Figure 1.10 : Duplex scanning: a) longitudinal view of the common femoral artery in pulsed wave Doppler US. b) Corresponding spectral density waveform.[11]

---

[11] Source: http://www.terarecon.com/gallery/images/us_5cfa_color_dopp.jpg (Accessed: 16/06/2009).

However, all these analyses have limited accuracy in tortuous and densely calcified arterial segments. Furthermore, it is not easy to visualize the entire lower limb vascular tree within an acceptable time frame using color-flow or power Doppler US. Moreover, assessment of atherosclerotic disease with conventional B-mode 2D-US images is highly operator dependant because of the high variability encountered with 2D freehand US methods when imaging a 3D anatomy [32]. A complete 3D representation of lower limb vessels over long segments, usually starting from the abdominal aorta within the abdomen, following with iliac, femoral, and then with popliteal arteries to end in the tibial vessels of the calf, is required for comprehensive therapeutic planning (i.e., specific diameter and length of angioplasty balloons or stents).

1.5.2 Invasive diagnostic methods

1.5.2.1 Digital subtraction angiography (DSA)

Digital subtraction angiography is a fluoroscopy technique that allows real-time x-ray imaging of blood vessels with high temporal resolution [30]. Basically, the x-ray tube, filters and collimation are the components that altogether create a beam of x-ray photons of well-defined intensity; penetrability and spatial distribution that include an image intensifier and computer technology (see Fig. 1.11a). To visualize the lumen of blood vessels, this technique uses radio-opaque contrast agent injected into the blood with a guide wire and catheter inserted through the femoral artery. Then, radiologists can evaluate the anatomy of blood vessels by subtracting bones and other organs from previously acquired frames in order to view only the vessels filled with contrast agent. Patients have to remain motionless during the entire procedure.

DSA is the standard of reference for evaluating lower limb arterial diseases [12]. Angiograms provide the best image quality that outlines the entire lower limb vessel anatomy in 2D projections and identifies areas of narrowing (see Fig. 1.11b). Stenosis quantification is performed on diameter reduction ratios only [33]. Angiography is also

primarily used during therapeutic interventions (e.g., arterial angioplasty) as it offers real-time imaging.

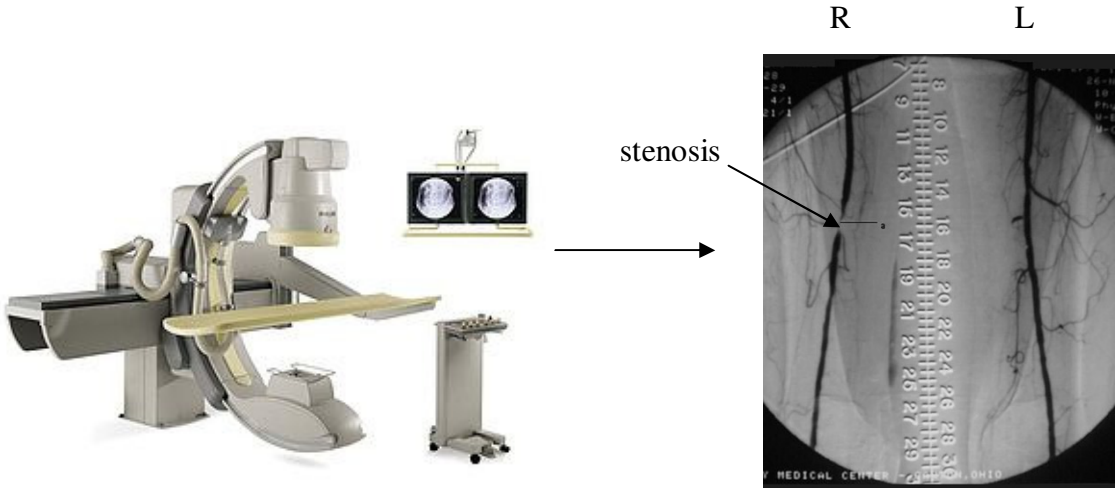

(a) (b)

Figure 1.11: DSA diagnosis: (a) the fluroscopic equipment and (b) an angiogram of lower limb arteries with a stenosis on the right leg.[12]

Nevertheless, DSA is an invasive ionizing procedure of substantial costs associated with potential morbidity [15]. The main complications of DSA examinations are thromboembolic events, bleeding from the puncture site, vascular injury, and exposure to radiation and toxicity related to iodinated contrast dyes [34]. Bed rest of 1 day is usually required after the procedure is completed to avoid putting stress on the arterial puncture. Furthermore, information on the morphology of the atherosclerotic plaque with this method is incomplete since DSA images only the lumen of the vessel and is usually two dimensional. This method is also known to often overestimate the length of lesions and to not always show all patent lower limb vessels (below-knee vessels may be difficult to identify, especially if the injection is not made selectively) [19, 29].

---

[12] Source: (a) http://en.wikipedia.org/wiki/X-ray_image_intensifier (Accessed: 16/06/2009),
(b) http://www.rjmatthewsmd.com/Definitions/peripheral_vascular_disease.htm (Accessed: 09/07/2009).

1.5.2.2 Computed tomography angiography (CTA)

Computed tomography angiography is a medical imaging technique used to visualize arterial and venous vessels. Its principle is based on computed tomography, which combines x-rays with computerized analysis for imaging [30]. Basically, x-ray beams are passed from a single rotational axis into the targeted area of the body at several different angles to obtain projection images that are after assembled by a computer into 3D memory matrix. Fig. 1.12a shows the CT scan equipment. CTA necessitates the injection of iodine contrast agent that is inserted with a needle into a peripheral vein. The computer software permits 3D imaging performed by multiplanar reconstruction (MPR) in stacking axial slices or alternatively by maximum intensity projection (MIP), surface or volume rendering techniques based on the threshold value of radiodensity chosen by the operator.

(a) (b)

Figure 1.12: (a) A CTA medical imaging equipment. (b) A 3D surface rendered view of lower limb arteries with CTA.[13]

CTA replaces conventional angiography in many PAD imaging studies [22]. In the assessment of symptomatic lower extremity arterial disease, the diagnostic performances of CTA and DSA are quite similar [12]. In fact, CTA involves minimal risk compared to DSA since it is less invasive (i.e., exposes the patient to less ionizing radiations and do not

[13] Source : (a) http://www.mckweb.com/Services/Pages/Diagnostic%20Imaging%20Services.aspx (Accessed 03/07/2009),
(b) http://www.maconcvi.org/pad.html (Accessed: 03/07/2009).

require arterial puncture) [26]. Furthermore, CTA has a lower cost than DSA for diagnosis, improvement in quality of images and acquires volumetric images. Thus, 3D visualization of the arteries is possible from multiple angles and planes from a simple acquisition [26] (see Fig. 1.12b). Moreover, compared to DSA, CTA takes less time (a few seconds) to acquire images and it is less expensive [15, 16].

In addition, current high-speed, multidetector CTA techniques allow for direct evaluation and measurement of lumen diameters. Thus, stenoses can be quantified in millimetres and further derived in ratio percentages [33]. CTA also has a limited scan coverage and a good resolution [10, 12, 27]. Furthermore, it has the capability to visualize calcification and metallic implants such as endovascular stents or stent grafts [35]. Likewise, disagreements between conventional DSA and CTA results often occur in smaller arteries, particularly below the knee [12]. Moreover, several studies report decreased accuracy in severely calcified arteries and the use of a relatively large amount of intravenous contrast is a real concern for patients with reduced renal function [12, 26]. Thus, CTA might be insufficient to image accurately the entire vascular tree. Henceforth, DSA examination can be necessary to complement suboptimal CTA examinations for appropriate treatment planning.

1.5.2.3 Magnetic resonance angiography (MRA)

Magnetic resonance angiography [36] is a technique to image blood vessels based on magnetic resonance imaging (MRI). MRI generally provides the ability to manipulate and adjust tissue contrast with increasingly complex pulse sequences [30]. Moreover, it has the capability to accurately determine the position from the nuclear magnetic resonance signal and thus create an image. Fig. 1.13 shows an MRI system and an example of a lower limb image from this system.

Gadolinium contrast-enhanced magnetic resonance angiography is a non-invasive, non-ionizing, three-dimensional technique that has emerged as a front-line imaging approach for comprehensive evaluation of PAD [26, 37, 38]. The contrast medium is normally injected into a vein and images are acquired through the arteries within a 15-25 seconds apnea (breath-hold). Thus, if the patient remains perfectly still, high quality images

are acquired with a stack of slices that represents the 3D volume of the entire body; where slices of the vessels of interest can be selected. Display of this 3D representation is performed with a rendering method, i.e. a maximum intensity projection (MIP) that computes pixels at the highest value for display on screen. The resulting images are comparable with conventional angiography [22, 38] (see Fig.1.13b). Furthermore, MRA provides precise measurements of arterial stenoses and occlusions that are required for the planning of therapeutic interventions [26, 37, 38]. Thus, in the clinical setting, MRA can be extremely helpful in diagnosis as well as subsequent management of patients with PAD. However, artefacts present challenges in MRA for diagnostic accuracy due to signal loss from in-plane saturation and turbulent flow. Artefacts are also caused by metallic clips and stents [26]. In addition, compared to CTA, MRA seems poorer in resolution, is far more expensive and the technology is often less available for scanning PAD [35]. Moreover, MRA images mainly the vessel lumen and tends to overestimate the degree of stenosis [23, 35]. Other limiting factors with this modality in patients are claustrophobia, the rare occurrence of systemic nephrogenic fibrosis in case of renal failure and contradictions related to metal implants or pacemakers.

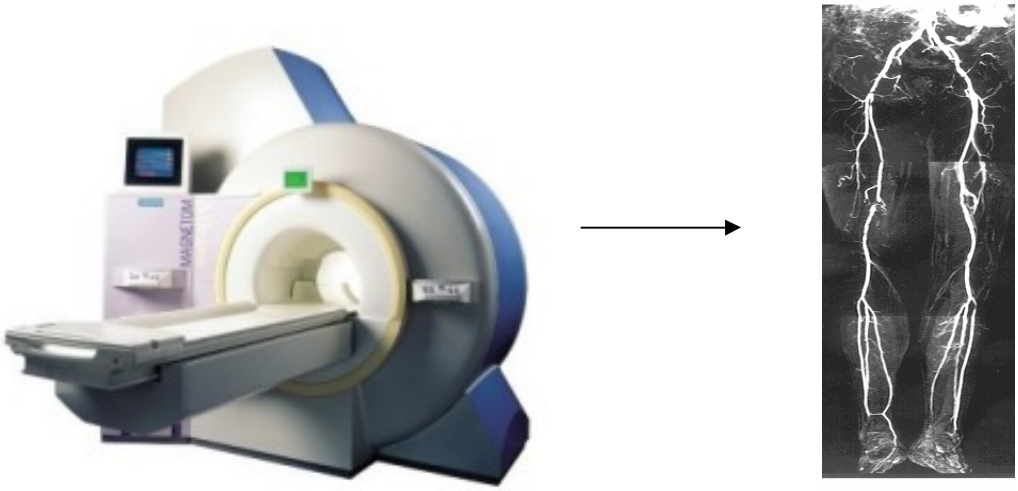

(a) (b)

Figure 1.13: (a) MRI system. (b) MRA combined views of different portions of the lower limb anatomy presented into one simple view.[14]

[14] Source: (a) www.mri-equipment.com/MRI.cfm (Accessed: 17/06/2009),
(b) http://www.freepatentsonline.com/6564085.html (Accessed: 16/06/2009).

1.5.2.4 Other technologies

Diagnosis procedures at the cellular level are also emerging. They regard not only the symptomatic, but focus on the early asymptomatic phase of the disease as well [39]. For example, research on the vascular inflammation process is of interest because its importance in atherosclerosis is well established. However, limited data exist on the relationship between vascular inflammation and the severity of PAD despite several findings [40]. Thus, this might be of importance in future diagnosis and treatment of the disease.

Other alternatives are intravascular ultrasonography (IVUS) and angioscopy which are both invasive techniques that can visualize the vessel wall from inside the lumen [27]. The IVUS technique allows a visualization of the atherosclerotic plaque with a high spatial resolution important to identify arterial lesions and its relation with vessel wall that cannot be depicted on DSA. It can also be beneficial to plan an appropriate therapy. Indeed, this technology has shown promise particularly for the monitoring of endovascular interventions (e.g., angioplasty or stent deployment). Nevertheless, segmenting IVUS images is challenging because the data is quite large and the IVUS is susceptible to artefacts especially in calcified arteries [41].

Finally, physicians largely rely on the clinical examination to identify patients needing further testing to diagnose PAD. They depend on imaging technologies to assess quantitatively, the location and severity of the lesion. Thus, based on the diagnosis, proper therapeutic planning can be achieved.

1.6 Therapeutic interventions

Therapeutic goals in PAD are basically to preserve or restore a distal circulation allowing daily activities in claudicant patients and prevent limb loss in critical limb ischemia. The treatment also aims to improve the patient's quality of life by reducing or eliminating symptoms and pain when legs are exerted [7, 19]. Early treatment of PAD is critical because benefits are then optimized [42]. At first, when PAD is suspected or diagnosed and risk factors are assessed, primary PAD management focuses on the reduction of the risk of cardiovascular events by modifying risk factors aggressively (i.e., diabetes mellitus, smoking, hyperlipidemia and hypertension), as suggested by the American Heart Association for CAD [43, 44]. This includes smoking cessation, exercise therapy, antiplatelet therapy as well as adequate blood pressure (i.e., hypertension), glucose and lipid control (i.e., dyslipidemia with statin drugs) [7, 42-44]. However, because this disease is mainly asymptomatic, in most cases, diagnosis is completed at an advanced stage when stenoses are severe. As a result, frequent invasive therapeutic interventions need to be planned and achieved in order to relieve PAD symptoms with balloon angioplasty, stents and surgical revascularization [18]. Specific details on all these treatments follow.

1.6.1 Medical treatment

The amount and the duration of tobacco use correlate directly with PAD development and progression [22, 45]. Thus, smoking cessation is the most important modifiable risk factor that can increase long-term survival in patients with PAD, reduce the severity of claudication and relieve associated pain [46]. Many clinicians advice patients to quit smoking and make use of nicotine replacement therapy combined with antidepressants (e.g., bupropion) to prolong the cessation rate [22, 36, 45]. Of course, this treatment option consists of modifying behaviour by counselling and by a short-term tobacco dependence pharmacotherapy. However, smoking cessation is a short term therapy that remains difficult to maintain long-term [46]. Thus, alternative methods should be considered.

Clinicians also advise exercise trainings to improve limb function. Exercise therapy programs can significantly improve the walking time and ability of patients affected with intermittent claudication [45]. The programs involve the combination of walking, stair climbing, cycling and dynamic & static leg exercises to near-maximal pain with 2-3 sessions of 30 minutes per week over a period of 6 months [46-48]. By the end of the program (after no more exercises are performed), walking distances are doubled and this improvement can last for up to 15 months [27]. Because unsupervised exercises have rarely shown to offer meaningful clinical benefits [46], a financial support for a PAD rehabilitation program must be available with trained personnel for this method to be successful. Accordingly, supervised exercises can produce significant results that are equivalent to invasive surgical treatments [36, 44]. However, the patient needs to be motivated.

At last, the most common and straightforward therapy are pharmaceuticals. Antiplatelet therapy is the cornerstone strategy for pharmacological intervention in PAD (with the exception of patients who suffer bleeding disorders) [45]. These drugs prevent ischemic events in lower limbs and like most PAD drugs, they also prevent secondary vascular events to occur (e.g., cardiovascular morbidity and mortality) [8, 49]. Also these drugs can modify the platelet activity which causes thrombus formation that can result in cardiovascular events. Aspirin is the most popular affordable antiplatelet agent prescribed by clinicians. The benefits associated to this drug are: delayed progression rate, reduce surgical need for an intervention and prolonged effectiveness of an invasive treatment (e.g., revascularization procedures with graft) [24, 36].

Also, patients with PAD normally have CAD and CVD that are associated to diabetes mellitus, hypertension and hyperlipidemia [36, 44]. To prevent atherosclerosis systematic complications (e.g., stroke, heart attack or death), therapies target on the control of risk factors such as blood pressure reduction (i.e., with β-blockers, angiotensin-converting enzyme inhibitors (ACE)), aggressive LDL cholesterol lowering (e.g., with statins) and glycemic control. Other pharmacologic treatments are also available to potentially relieve symptoms and improve walking distance (e.g., cilostazol, etc...) [7, 8, 25]. Also, it is known that a dysfunctional endothelium plays a crucial role in all stages of

atherosclerosis. As a result, many PAD upcoming therapeutic interventions are focusing on endothelial dysfunction prevention and healing [24].

In final analysis, PAD patients should be approached like coronary and carotid diseases with the above non-invasive treatments. Nonetheless, many patients with PAD are not receiving optimal medical management because the perceptions and knowledge of risk-reduction pharmacotherapy are poor among vascular surgeons [27, 36, 42, 50].

1.6.2 Invasive treatment

Invasive therapy provides the most immediate benefit to symptomatic patients with severe PAD. Common endovascular interventions are percutaneous balloon angioplasty and stenting whereas surgical management includes bypass revascularization and lastly, amputation [22]. Since they are less invasive, catheter-based methods are more frequently used [17] (see Fig. 1.14) and require appropriate imaging to plan the intervention [33]. These invasive procedures are indicated for advanced PAD limiting patient life style that had an inadequate response to non-invasive therapy or patient presenting a risk of limb loss.

Percutaneous transluminal angioplasty (PTA) is the preferred initial treatment for patients with disabling claudication since it is the least invasive procedure [51]. Benefits associated with this method over other surgical interventions are lower initial morbidity and mortality, shorter hospital length stay and decreased trauma [7]. It is performed on vessel lesion segments of less than 10 cm in length mostly on femoropopliteal stenotic lesions [48, 51]. To have a favourable outcome with this procedure, the stenotic lesion needs to be proximal with a good distal run-off. Initial success rate of PTA are > 90 %, however, subsequent failure rates remain high because platelet thrombus formation produces restenosis (40 to 60 % in the femoropopliteal segment after 2 years) and reocclusion [8, 52]. Besides, PTA success rates are highly operator-dependant. Thus, this technique is usually used aggressively in clinical centers that manage a large volume of patients [51]. In addition, this approach offers short term (6 months) benefits compared to exercise therapy, but have similar long-term (24 months) advantages than the latter [27].

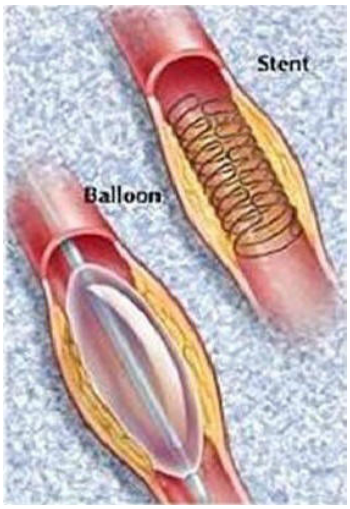

Figure 1.14: Invasive therapeutic interventions: balloon angioplasty and stenting.[15]

Intravascular stents were developed to provide a long-term radial force to support the vessel after angioplasty and to prevent elastic recoil with improved patency [22, 53]. Metallic stents can be placed at many different arterial sites (e.g., coronary, iliac and femoral arteries) to prevent restenosis. In addition, a significant improvement in patients with claudication symptoms can be seen after iliac-artery stenting where a 4 year patency rate increase of 12 % for stenoses and 7 % for occlusions, respectively, were reported compared to angioplasty alone [27]. Moreover, a 39% failure risk reduction was shown [27]. However, this method is limited because in-stent restenosis still represents a major limitation [54, 55]. Restenosis occurs as a vascular reaction to catheter-induced vessel injury that stimulates vessel wall proliferation more prominent in smaller vessels. To control this problem, it is necessary to avoid over sized stents, since the rate of restenosis is directly correlated with the arterial lumen obtained immediately after angioplasty. Other alternatives include fabricating pharmacologic therapeutic stents, where the vessel proliferation is inhibited locally [55]. Nevertheless, this type of stent is restricted to large vessels (i.e., 3.0-3.5 mm diameters).

Surgical revascularization is reserved for patients with critical limb ischemia (i.e., limb-threatening) [17, 22]. This treatment is highly recommended to heal ischemic ulcers

[15] Source: www.strokeupdate.co.uk/news.htm (Accessed: 16/06/2009).

and prevent limb loss. Most of ischemic limbs can be revascularized with bypass surgery for patients with long aortoiliac or superficial femoral artery occlusions that are unsuitable for angioplasty and stenting [27]. Five year patency rates of 80.0 % – 90.0 % and 70.0 % are reported for the aortobifemoral and femoropopliteal bypasses, respectively [27]. Even so, the limited length of the aortoiliac or the superficial femoral artery, the unavailability of autogenous (self-generating) veins or the irreversible gangrene may limit this procedure and if graft occlusion occurs; lower-limb ischemia may become a worse threat to the limb [22].

Immediate and long-term survival rates are higher in patients having revascularization rather than amputation for limb threatening ischemia. At this advanced stage of the pathology, the infection can threaten the patient's life [22]. Amputation is the last recourse when tissue loss can no longer be saved. In this case, the surgery is graded too risky, life expectancy is very low and/or there is functional limitation in the leg [22, 48]. Most medical and surgical interventions present programs that can prevent amputation, however, it remains an acceptable option for patients facing a prolonged course of treatment and a poor prognosis for a successful outcome.

In conclusion, surgical interventions directed toward PAD require additional imaging modalities that can clearly locate the lesions with accurate stenosis quantification and occlusion detection in order to define the target vessel for bypass surgery [33]. Furthermore, pharmaceuticals can be combined with these interventions, in order to minimize symptoms and disability, slow down local disease progression, reduce systematic cardiovascular morbidity/mortality and improve the durability of the surgical intervention [18].

1.7 Summary

At an early stage, before symptoms become apparent, the potential to treat atherosclerosis is high. In fact, significant disease progression can frequently be turned into disease regression [56]. To achieve this goal, it is critical to first screen PAD on symptomatic patients with precise information on the location and on the morphology of stenotic lesions using a standard method. Intermittent claudication symptoms are generally

associated with stenoses or occlusions of the iliac or femoro-popliteal arteries [8]. Claudication in the calf is commonly due the disease in the femoral arteries. Staggeringly, 75.0 % of patients with this symptom are underdiagnosed despite its significant impact on life expectancy, functional status and on the quality of life [8]. Particularly, PAD is an important marker given the strong correlation that exists to CAD and CVD, who are both linked to stroke, heart attack and death [22, 45, 46]. The population is poorly informed about symptoms and consequences of PAD (i.e., definition, risk factors, limb symptoms, amputation risks and cardiovascular risk events) [57]. In fact, only one third of patients having PAD symptoms report them to their physicians [7]. Therefore, they frequently loose the opportunity to initiate primary care with their general practitioners. Thus, it is essential that physicians are proactive in identifying intermittent claudication in patients.

In that matter, proper diagnostic tools need to be offered in order to allow clinicians to select a treatment plan that can alleviate pain, improve functional ability and reduce the future risk of cardiovascular events when PAD symptoms are present [13]. Presently, imaging technologies provide the best option to enable stenosis/occlusion location and quantification for an appropriate therapeutic intervention (pharmaceutical, endovascular or surgical) in asymptomatic and symptomatic patients. Duplex US can provide non-invasively this information without any additional visits to the clinic at first consultation and sometimes based on this sole imaging reference, angioplasty treatments and even surgical revascularisation can be planned [27, 58, 59]. Clinically, DSA is the standard to plan invasive therapy (surgical or endovascular interventions) and it is used as well to visualize calf arteries of patients with severe proximal stenoses and calcified vessels difficult to detect with duplex US [27, 60]. However, it presents its own set of challenges as the procedure is invasive for the patients. MRA and CTA provide more additional information than angiography for preoperative planning, but they are expensive, not easily accessible and present risks linked to the toxicity of contrast agents (CTA, MRA) and can be contraindicated.

Compared to other diagnostic imaging technologies, US imaging is an excellent diagnosis tool for detecting and quantifying lower limb stenoses. It is the least invasive method that is the safest for clinical investigation of the arteries with no ionizing radiation

and no known adverse effects compared to MRA, CTA and DSA. Moreover, this convenient technology has the lowest cost and is the most routinely used in clinic to offer real-time imaging in an anatomical region of interest. Already, many clinical reports showed agreement in grading severe stenoses for duplex US compared to angiography and MRA [61-63]. The echogenicity of atherosclerotic lesions in B-mode also permits classification, detection of plaque morphology and stenosis identification [64]. Also, functional information on the hemodynamics of stenoses is made available with Duplex US. Nonetheless, in US imaging measures depend on the US probe angle of insonation, the variability among observers and the limited accuracy in multi segmental arterial lesions [26, 44, 56, 58, 59, 65].

Additionally, US imaging does not provide a vascular road map of lower limb steno-occlusive disease which is necessary to indicate the length and localization of stenotic lesions for therapy planning. Usually, preoperative planning treatment in patients with symptoms of lower limb PAD is based on duplex US imaging, exclusively done by dividing the leg into arterial segments [60] or by prevalent imaging modalities that can render the entire map of lower limb vessels (e.g., DSA, MRA and CTA). It is known that atherosclerotic lesions develop preferentially at curved and bifurcated regions of the artery [31]. These sites are often difficult to access with an US probe to render an appropriate view and are challenging to reproduce even with a skilled clinician. Thus, poor visualization and quantification of stenoses are consequently inevitable with 2D-US imaging. This is even more so in lower limbs, due to the length of the vascular bed to be imaged. However, many 2D slice views acquired at arbitrary orientations and positions can analyse and reproduce more accurately the geometry of interest when they are summed up together in the form of a 3D representation. Consequently, a 3D reconstructed model of lower limb vessels can improve diagnostic confidence and offer the possibility of monitoring systematically the extent of atherosclerotic disease**.** Furthermore, a 3D-US imaging technology that can render correctly the entire vascular tree of lower limbs offers the best option to define precisely the stenosis degree.

In this context, the main objective of the present thesis was the development of a 3D-US imaging method based on a robotic scanning system for the application in hand. The following chapter summarizes the current knowledge on 3D-US imaging technologies. The rest of this thesis is presenting, in three consecutive chapters, our robotic strategy to address this issue. A discussion and conclusion conclude this document.

Chapter 2

Literature Review of 3D-US Imaging systems

It is the tension between creativity and skepticism that has produced the stunning and unexpected findings of science.

Carl Sagan

This chapter presents the literature review behind 3D-US imaging systems. First, basic 3D-US imaging system principle are revised, then sensorless and sensorbased tracking systems are described, followed by robotic developments. For each system, the clinical application is explained as well as the advantages and limitations of the technology. Thereafter, the hypothesis and objectives are stated and the thesis is outlined.

2.1 3D-US imaging system

3D-US systems offer the best potential to precisely locate and quantify atherosclerotic lesions. This technology allows direct visualization of 3D anatomy where 2D slice views can be generated at arbitrary orientations. Volume and other 3D-based measurements can be obtained more accurately than in 2D [66]. For academic and industrial research, 3D-US offers opportunities to visualize the entire volume of the scanned area [66, 67]. Already, many successful systems were developed and validated in various clinical applications notably obstetrics, cardiology, and vascular imaging to increase diagnosis confidence [68]. Thus, a physician has the possibility to perform different image post-processing after patient volume scanning such as generation of multiplanar (MPR) or volume rendering (VR) reformations and re-evaluate the diagnosis

with experts across networks at remote locations [68]. Nonetheless, to have an expending use in clinic, 3D-US performance needs to be equal or surpass the current 2D-US methods.

There exist several acquisition methods to generate a volume from a region of interest. In most cases, a series of image planes are acquired from the volume and the major difference in 3D-US technologies comes from the specific method used to locate the position of the slice within the volume [68]. Most existing techniques focus on tracking the probe position in freehand (with or without position sensors) and by using a mechanical or robotic approach. For each strategy proposed, many developments were reported in the literature. The following sections will discuss these approaches employed to locate 2D-US image planes in a volume for 3D-US reconstruction. In our application, an accuracy of 1.0 mm or less is required for the position measuring system to generate a high-quality volume data.

2.2 3D Sensorless systems

2.2.1 Pseudo tracking

Most commercially available US scanners can produce 3D-US images by stacking 2D slices together to reconstruct a final 3D result [69] (i.e., pseudo-tracking). In this matter, the acquisition sequence is important because the acquired tomographic images are assembled in 3D regardless of orientation and positioning of the US probe. However, pseudo-tracking is limited particularly to scan linear geometries since positions of 2D-US images are not tracked. In addition, it does not guarantee that distances are reliable and should not be used to measure arterial geometry (e.g., distances and areas, etc.) [70].

2.2.2 Decorrelation techniques

3D-US can be acquired by finding the separations of a frame pair by using information on the acquired US images themselves. Basically, this sensorless approach attempts to estimate the relative 3D position and orientation of a probe in space by analyzing the speckle (i.e., reflected spatial energy pattern that comes from the interaction of a coherent energy source with scatterers) in the US image using decorrelation or linear

regression [70-73] (see Fig. 2.1). The degree of decorrelation in the speckle is proportional to the distance between the two images and depends on many transducer parameters including the degree of focusing and depth. By using a pre-calibrated decorrelation curve, this approach can compute the elevation separation.

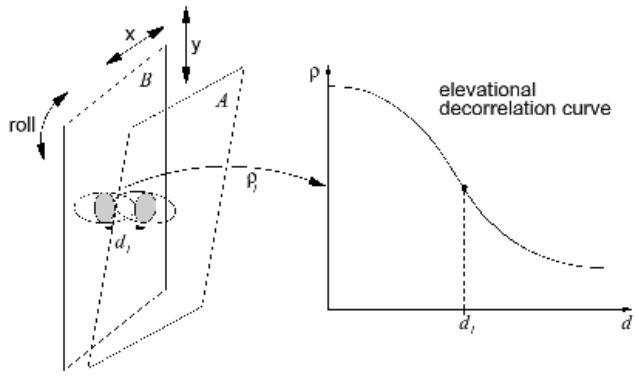

Figure 2.1: Speckle decorrelation technique.[16]

Nevertheless, this method depends on the speckle to be fully developed [74]. In reality, tissue contains regions of coherent scattering that decorrelate at a slower rate than regions with fully developed speckle. Moreover, other sources can cause speckle decorrelation such as noise, in-plane motion, transducer rotation, tissue compression and physiological motion; all these factors might appear as elevation movement [74]. In addition, most decorrelation techniques do not provide the direction of the B-scans; it assumes the probe motion is monotic with no intersecting frames. Given these limitations on position accuracy, most studies agree that sensorless methods are far from being optimal use in clinical applications [71-74].

2.2.3 Integrated position sensors and 3D probes

Alternate methods integrate position sensors within the transducer probe. These bulky probes can brush a volume at different orientations, where a special mechanism inside the probe is used to sweep the plane of the B-scan through a volume of interest. The

[16] Source : http://svrwww.eng.cam.ac.uk/~ahg/cp3dus/speckle_decorrelation.gif (Accessed: 23/07/2009).

probe movements are usually mechanically produced by a motor that can rotate, translate or sweep in a linear, wedge and freehand direction [75] (see Fig. 2.2). This method is easy of use and can produce standardized volumes for a densely sampled data without irregular gaps since all angles and locations between slices are exactly known [76]. In addition, the volume of data acquired (stack of 2D images) is immediately available after acquisition, without the need of subsequent reprojection or processing. When needed, post processing and generation of multiplanar views from the volumic acquisition can be easily done [30]. This approach has been used in numerous clinical research applications such as the carotid arteries, heart, foetus, kidney, eye, prostate and breast but also for endoscopic ultrasound acquisition such as transrectal, endovaginal or transesophageal imaging [70, 76].

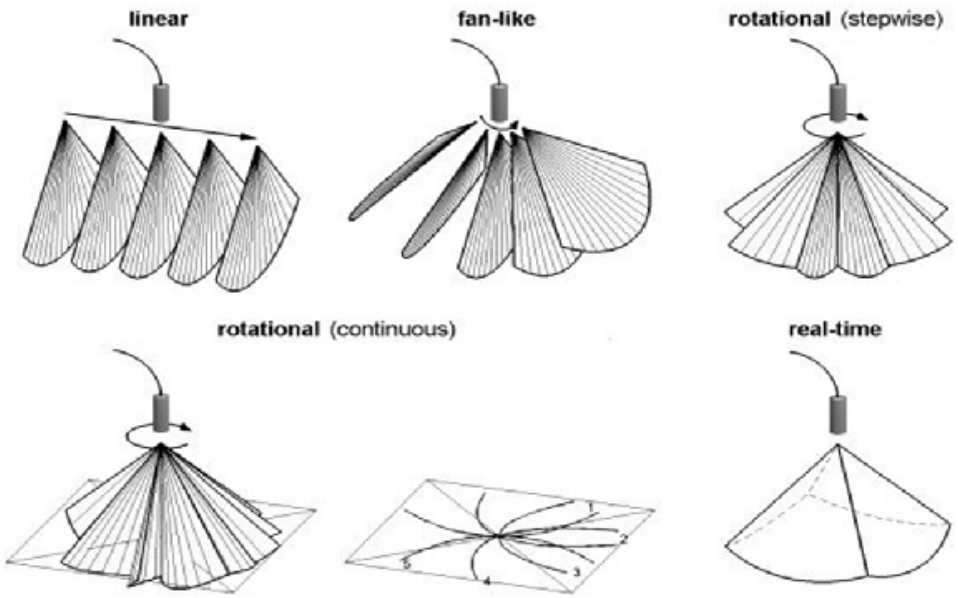

Figure 2.2: Integrated position sensor probes.[17]

Nevertheless, the mechanical scan technique is sensitive to the scanning protocol. Thus, a priori knowledge on the geometry must be known precisely to avoid misinterpretation caused by distortions and patient motion from rapid 2D image successions. The 3D image produced is not isotropic because of the poor elevation resolution of the transducer (i.e., the direction perpendicular to the US image plane) and the

[17] Source:http://www.escardio.org/communities/EAE/3d-echo-box/3d-echatlas/background/PublishingImages/Reconstruction-methods/Linear-fanlike.gif

scan spacing (i.e., distance between US image planes) [70, 77]. Moreover, this method requires the considerable expense of a dedicated machine and is limited to a maximum volume dictated by hardware constraints in the probe [78]. This relatively small field-of-view (FOV), restricts scanning with this probe to only small regions of interest due to the high computed time required to generate a volume and the mechanical limitations [75]. Thus, it is not possible to cover the entire lower limb vessels and produce an accurate 3D representation with these approaches [70].

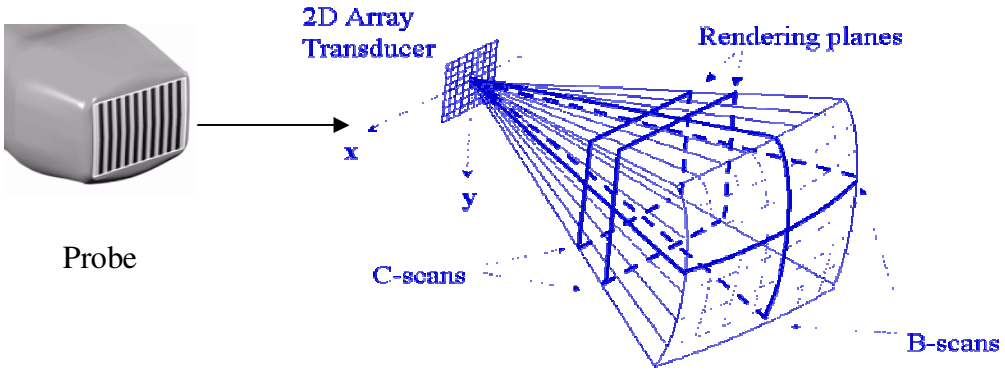

Figure 2.3: 2D linear probe array and the process to acquire a 3D volume is shown.[18] B-scans lie in the x-y plane, while the C-scans (coronal planes or B-scans) lie in the elevation direction.

3D-US probes usually consist of multiple linear array transducers (five to seven rows 1.5D or 2D) (see Fig. 2.3) that have the ability to steer and focus the beam in the elevation direction (C-scans) to permit precise imaging in 3D [30]. These probes are also large, heavy and expensive in comparison to 2D probes [71, 79]. This technology can also be used to acquire real-time 3D volumes (i.e., 4D) [67]. In fact, this approach is often used in echocardiography to provide and allow correct anatomical examination of the heart structure with the aid of computerized software [80]. The major benefit accorded to 3D probes is a comprehensive view of cardiac valves and congenital abnormalities, along with immediate feedback for surgical interventions in intraoperative and postoperative settings [81, 82]. More specifically, it has shown great potential to become a new clinical standard in the assessment of the severity of mitral stenosis by means of accurate mitral valve area

[18] Source:http://www.ntnu.no/eksternweb/multimedia/archive/00009/1D2DArray_150_150_9928a.gif and http://www.4engr.com/images/research/b1a1bbc1e891b19f5ea4453cb95e1dbd.gif (Accessed: 23/07/2009).

measurements [83].

However, complex acquisition, lengthy data analysis and high associated cost have limited the use of 3D echardiography in daily clinical practice [80, 84]. Moreover, their resolution is said to be poorer in the elevation direction because it is dependant on the transducer element width; however compared to regular transducer arrays, they have a reduced signal-to-noise ratio [30, 84]. In addition, the scanning protocol is clinically different as the 3D probe is required to be held steadily over a volume of interest which is relatively very small (i.e., 1 cm x 1 cm with maximum depth of 2 cm). For all these factors, 3D-US probes cannot be used to evaluate lower limb arteries which are made of long vessel segments.

2.3 3D Sensor based systems

Sensor based 3D-US freehand systems include positioning information of the US probe from tracking devices. Many approaches have been developed for freehand scanning that allows the user to manipulate the transducer without significant constraints [70]. Each 2D image located in space is then used to reconstruct the sampled volume in a manner that minimizes distortions and maximizes accuracies. Moreover, since the scanning geometry is not predefined, it is imperative that the acquisition of images and positions have no significant gaps. This can be achieved by scanning the anatomy at a constant speed appropriate for the frame rate of the ultrasound scanner. Of the techniques available, five major basic positioning sensing systems have been outlined: articulated arms, acoustics, step motors, electromagnetic fields, optics and hybrids.

2.3.1 Articulated arm

The first forms of tracking system were made of articulated arms. The US probe was mounted on a multiple joint mechanical arm system, where potentiometers located at each joint of the movable arms provide information on the relative rotation of the arms [70]. The relative position of an US image was determined from the combination of the relative angulations of the joints. Accuracy of US image positioning lower than 0.4 mm has been reported with short arm links and reduced moveable joints [85]. Commercially available systems integrate arms with only three potentiometers in order to achieve

sufficient accuracy, while reducing arm size and flexibility (see Fig. 2.4) [84]. This method is mostly common in telemedicine applications [85]. Objects can be tracked at high frame rate and low latency with minimal interference with the enclosing environment. However, this approach is too rigid to be used with US probes because of its limited range of movement. Finally, angle measurement errors increase with the number of joints and the cumulative length of the arms [71, 86].

Figure 2.4: Articulated arm[19]

2.3.2 Acoustics

The oldest form of freehand tracking makes use of acoustic positioning systems. Basically, this approach exploits the sound-emitting devices (e.g., spark gaps) that are mounted on the US probe and small microphones for sound detection. The position and orientation of the transducer are determined in real-time from the known speed of sound in air, the measured time of flight of the sound pulse from the emitters on the transducer to the fixed microphones. This system performance has a manufacturing stated accuracy of 0.1 % in the distance from the sound emitter to the microphone. Combining the tracking system with a 2.5 MHz phased array US system, the performance was found to be less than 0.4 % in error for a 5.08 cm distance in a 3D pin model [87]. This approach has been used to measure left ventricular ejection fraction (to determine the systolic function) where the

[19] Source : http:// http://www.electricsco.com/detail115682-hydraulictappingmachine.htm (Accessed: 14/12/2010)

results were found to be comparable and even superior to the standard method of equilibrium radionuclide angiography [88]. However, these systems are affected by variation of temperature, pressure and humidity [71]. In addition, they require a constant line of sight between the speaker and the microphones [76]. Thus, with these restrictions, this method is not optimal for the lower limb scanning.

2.3.3 Linear step motors

Linear scanning of US using a step motor is a simple form of US probe tracking. In this approach, an external mechanical localizer translates the US probe linearly in order to acquire parallel 2D images (see Fig. 2.5). Since the spatial sampling interval is known, the reconstruction can be pre-computed and obtained immediately after a linear scan is performed [70]. This method has been successfully implemented in many carotid artery applications to measure the plaque volume using B-mode, color Doppler and power Doppler images [77, 89-92]. Because of its restricted range of motion, this method is not optimum for lower limb artery scans.

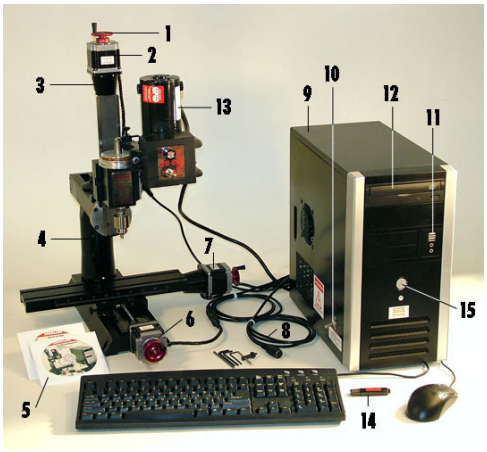

Figure 2.5: Linear Stepper Motor System (Sherline Products Inc., Vista, CA, USA)[20]

[20] Source : http://www.sherline.com/images/InstConex4.jpg (Accessed: 19/04/2010)

2.3.4 Electromagnetic sensors

Electromagnetic positioning is the most popular tracking method used in 3D freehand ultrasound systems [71]. This approach is based on the spatially varying magnetic field from a source transmitter (generated by either AC of DC current) where a receiver mounted on the transducer measures its intensity. The sensor is composed of three orthogonal coils that capture these signals and transform them into position and orientation information relative to the source [76]. Manufacturers claim positioning accuracy between 0.76- 1.8 mm for popular device brands such as Fastrack (Polhemus) (see Fig. 2.6) and Flock of Birds (Ascension) [71], however, system performance in locating a point target precisely was found experimentally to be within 1.7-3.5 mm [86, 93, 94]. This technology has been used extensively in research because of the great freedom of motion advantage it offers to track the US probe without constraint to linear motion and line-of-site. Moreover, freehand 3D-US system software which allows accurate acquisition of the raw data and immediate visualization of slices through the data is provided with the Stradx free-shared package [95]. Vascular applications include the left ventricle [86], the carotid artery [96-101], the saphenous vein grafts [102-104] and the vertebral artery [105]. Nevertheless, this technology is limited in clinical use because it is susceptible to noise and errors up to 8.4 mm in positional measurements due to electromagnetic interference from metallic objects (e.g., aluminum and similar low-permeability/high-conductivity metals such as the US probe and materials from the surgical environment) [93, 106, 107]. This distortion can be reduced by maximizing the distances from the transmitter (> 120 mm) to the interfering equipments because in the near range systematic errors tend to increase [106]. This associated inaccuracy is not optimal for clinicians who desire a constant positional accuracy performance from 3D-US system of the order of 1.0 mm [84].

Figure 2.6: AC electromagnetic tracking device by Polhemus (Polhemus Inc., Colchester, USA)[21]

2.3.5 Optical sensors

Optical methods use multiple cameras to track markers distributed on a predefined rigid structure in its line of sight [71, 84]. A minimal of three markers is necessary to determine the position and orientation of the rigid body in space. Additional markers can be added to improve the measurement accuracy and the camera visibility. The markers are either infrared light - emitting diode (IREDs) in active tracking mode or infrared light reflectors in passive tracking mode. In active mode, the IREDs emit light at predefined frequencies and the system of cameras detects the location of the emitters by triangulation. Whereas in passive mode, emitters inside the housing of the camera fire infrared light at the highly reflective spheres and the cameras localize them from the reflection detected from the spheres. This mode is very sensitive to large positional errors. The most common systems used are the two-camera model of Polaris by NDI (Northern Digital, Toronto, ON, Canada) and the three-camera model of Optotrack also by NDI or the FlashPoint 5000 (Boulder Innovation Group Inc., Boulder, CO, USA) [71]. Manufacturer claim positioning accuracies with this technology between 0.10-0.76 mm [71] and in laboratory setting to 1.40 mm [108]. The great advantage of this device is being insensitive to the metallic and electromagnetic noisy surgical environment. This technology was tested in various clinical applications such as percutaneous pericardial puncture [109], brain shift [108], stereotactic ultrasonography [110], image-guided surgery [84] and 3D mapping of the brachial plexus [111]. Even so, the main disadvantage of optical tracking is the need to maintain an unobstructed line of sight between the markers and the cameras. Positional errors up to

[21] Source: http://www.inition.co.uk/inition/images/product_mocaptrack_polhemus_fastrak.jpg (Accessed: 19/04/2010)

6.67 mm can be recorded by this device if markers are not optimally visible [112]. Thus, the limited freedom of movement and variable positional accuracy in a cluttered clinical setting make this choice of tracking device not optimal for lower limbs.

Figure 2.7: Optical tracking system with 2 cameras from Polaris NDI (Northern, Digital, Toronto, ON, Canada)[22]

2.3.6 Hybrid sensors

Hybrid sensors attempt to compensate for the shortcomings of each tracking technology (e.g., ultrasonic, magnetic and optical tracking sensors with accelerometers) by combining several multiple measurements to produce precise and robust results [113]. To satisfy registration accuracy requirements, most of them integrate magnetic sensors that are known to be very robust but unreliable in positional readings with an optical tracking system to compensate its errors on location [114, 115]. This kind of hybrid sensor offers many advantages because it can track multiple targets without restrictions of line-of-sight and can correct magnetic distortions [116, 117]. Improvements in the average positional error can be reduced by a factor of 3 with both technologies; the average position error with the optical tracking system was found to be 2.1 mm whereas it was 6.1 mm solely with the magnetic tracker [115]. This system has been applied mostly in augmented reality systems, where it is necessary that objects appear at the same physical location for all users of the system [115]. Hybrid sensors have also been used in autonomous navigation of mobile robots and material handling in virtual environments [117]. Finally, a 3D-US system with

[22] Source : http://www.tech-ex.com/images/products/0008/8580_2008819154957.jpg (Accessed: 19/04/2010)

an augmented reality visualization has been tested in laparoscopic surgery and ultrasound-guided needle biopsies [116, 118]. The main limitations of this approach are the need for an additional calibration procedure to integrate each tracking system to each other and the high computation time.

2.4 US robotic developments

Robotic systems represent a promising approach for lower limb artery imaging as they simultaneously control and standardize the 3D-US acquisition process for long scanning distances and complex geometries. In addition, they are viewed as an accurate and repeatable technology enabling generation of reliable 3D volumes with a potential to improve clinical management [119]. Many medical US prototype robots have been developed distinctively to explore these advantages. Main areas of development are presented below.

2.4.1 Telemedicine

Robotized telemedicine is a research area in US imaging that permits medical experts to perform highly skilled (i.e., operator-dependant) tasks from a center remotely located to a patient [120, 121]. Tele-operated robotic chains acquire real-time US images for medical diagnosis over the abdominal area of a remote patient with a light-weight or parallel manipulator [120]. The real probe is placed on the slave robot end-effector where its control is transmitted from a remote location with tracked movements of the expert's hand during a scan with a fictive probe. To correct probe positioning, the system is monitored via videoconference between the expert and the operator.

Different systems exist in tele-ecography with specialized applications in research. The most notable developments are discussed. TERESA is a project with a tele-operated system conceptualized to follow up on astronauts' cardiovascular system in microgravity environment or to perform a quality US exam on a geographically distant patient [122]. It make use of a fictive probe and an electromagnetic tracker to control at distance a 4 degree of freedom (DOF) light-weight mechanical robot that enables positioning of the US probe according to 3 degrees in rotation and one translation along the probe axis. The OTELO

project consists of a mobile tele-echography system that employs an ultra-light robot design to achieve reliable US imaging at an isolated site distant from a specialist clinician [120, 121]. The system is configured with a pseudo-haptic fictive probe in which the medical expert interacts to control a 6 DOF light-weight robotic system with a strain gauge force sensor embedded in the probe holder to measure the contact force (see Figure 2.8). The TER tele-operated system is one of the more recent developments where a new architecture design for a low-weight portable slave robot that is cable-driven, nonrigid in structure is proposed [123, 124]. A haptic PHANTOM device in the master site provides total control of the echographic probe with a realistic perception of the normal force of contact on the patient's skin. This system also is distinctively actuated by the movements of the patient's abdomen.

Figure 2.8: OTELO: the mobile tele-echography system using an ultra-light robot[23]

ORB, another system, used a two-axis joystick to control a parallel robot design applied over a patient's abdomen, where angle and position of the probe are monitored by 4 miniature force sensors fixed at the side plate of the probe holder [125, 126]. While, all these developments seem promising, tele-echography systems primary concern is to support a robust communication link where data can be exchanged between the two stations safely between patients and experts that include US images, robot controls and tracking information with a suitable bandwidth [127]. Most research efforts aim to improve the

[23] Source : http://wwwlasmea.univ-bpclermont.fr/jnrr03/I/I11-OTELO-Patient-Expert_p.jpg (Accessed: 28/04/2010)

telecommunication aspect by streaming wirelessly in real-time medical images of quality [128-130]. Moreover, in these systems, the impact of position errors of the slave robot is less important for medical experts since no 3D-US reconstruction is envisioned. The error in probe positioning can be corrected by the physician based on the feedback given by the echographic image rather than the position of the real probe on the patient's surface [123]. Given the limited accuracy of these systems for 3D applications and their architecture not adapted to perform scanning on lower limbs and acquire 3D-US data, they cannot be applied to our clinical application.

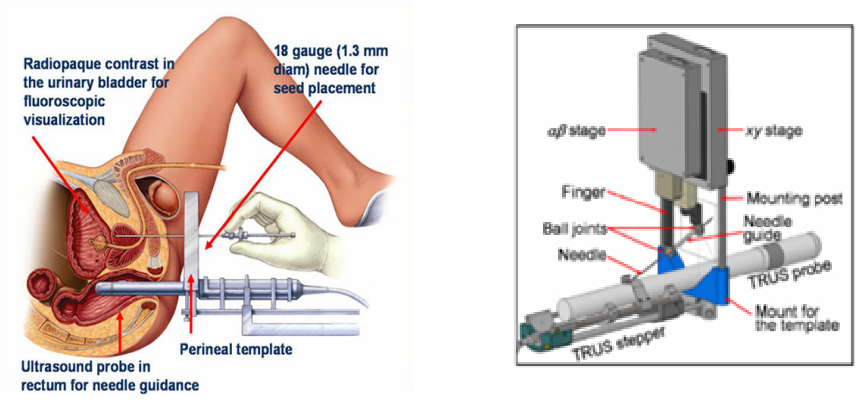

(a) (b)

Figure 2.9: (a) Brachytherapy treatment performed manually[24]. (b) Robotic system for brachhytherapy[25].

2.4.2 Brachytherapy

Prostate cancer has recently gained much attention in US robotic developments because of brachytherapy, a successful treatment with low side effects and high benefits [131]. This method localizes irradiation of the prostate gland by the insertion of radioactive seeds using hollow needles inserted through the perineum of the patient in the lithotomy position with a trans-rectal US (TRUS) guidance (see Fig. 2.9a) [132]. This intervention distributes uniformly radioactive doses throughout the entire volume of the prostate without overdosage then minimizing side-effect on adjacent organs. Normally, a template is used to

[24] Source : http://www.urologyassociates.com.au/uploads/31417/ufiles/prostate_cancer_brachytherapy.jpg (Accessed: 02/05/2010).
[25] Source : http://www.na-mic.org/Wiki/images/thumb/b/b0/ProstateDiagram.png/200px-ProstateDiagram.png (Accessed : 02/05/2010).

insert manually the needles under ultrasound guidance along a grid of horizontal lines [132]. However, the mobility of the prostate and surrounding tissues make this task difficult. Robotic systems were developed to standardize this procedure. This robotic system integrates a positioning system and a driver for the TRUS, thus allowing needle positioning to insert the seed [131, 133, 134]. Planning of the needle trajectory can be performed firsthand to guide and control its insertion [135, 136] with less than 1.0 mm targeting errors [134, 137]. Also, software developed with these systems permit 3D-US images of the organ acquired with a mechanical rotation of the probe [134, 136]. However, these robotic systems, normally small in architecture, can only accommodate TRUS probes and needles for rotation and positioning.

2.4.3 Cardiovascular diseases

Cardiovascular disease prevention is another research area that benefited greatly from US robot developments. Hippocrate represents a first example where a robotic system was developed to manipulate US probes on the patient's skin with an exerting effort to scan the carotid and femoral arteries (see Fig. 2.10) [138-140]. The objective of this system was to enhance clinician capabilities in terms of accuracy, reproducibility and force control in order to generate a 3D vessel reconstruction and volume quantification of atheromatous plaques. This robotic system can record successive 2D acquisitions with a constant force at a regular step and a cardiac synchronization to generate a 3D reconstruction of the vessel.

Figure 2.10: Hippocrate robot[26]

[26] Source : http://www.emeraldinsight.com/fig/0490300110002.png (Accessed: 02/05/2010)

The architecture is a 6 DOF serial manipulator with revolute joints suspended above the patient's bed for efficiency and safety; other security controls are also included. The movements of the robot are guided by a graphical user interface and a force/torque position controller. Clinicians can manually handle the robot in 'teaching mode', and in 'replay mode', the robot can reach the pre-defined taught path. A high repeatability of 0.05 mm and 0.5 mm absolute accuracy are claimed with this robot. However, these measures have not been tested thoroughly and the preliminary 3D reconstruction of the carotid artery was poor [140]. To our knowledge, no follow-up studies exist to support the efficiency of this design, except its use in holding a probe to evaluate brachial artery wall shear rate [141]. It was also tested to improve skin harvesting process in robotized reconstructive surgery [140, 142].

Another approach developed at the University of British Columbia was a visual servoing method to track in real-time the carotid artery [143, 144]. The motivation behind this design was to minimize the occurrence of musculoskeletal disorders secondary to ergonomic problems associated with prolonged periods of probe holding leading to a stress on the cervical spine, shoulder and arm of the operator. This tele-operated system consists of a master hand controller (joystick/haptic interface), a slave manipulator carrying the US probe and a computer control [106, 145]. The operator can remotely position the US probe at a relative position to the patient's body where the motion of the robotic arm and the hand controller are simultaneously based on measured positions and forces, acquired US images along with taught positions and force trajectories.

Figure 2.11: UBC image-guided robot-assisted diagnostic ultrasound[27]

An algorithm that detects the boundary of the carotid artery and determines its center of gravity is tracked in real-time to control the robot. Also for safety controls, the 6 DOF robotic arm was designed light-weight with limited force capability, counter-balanced with backdrivable joints. To control the US probe only 3 DOF are possible because of the US image servoing where one axis is reserved for motion and others for the image plane. The robot's tracking algorithm has been tested on a US phantom composed of 3 aligned tubes and the neck of 1 patient. It has reconstructed in 3D the mimicking vessels with less than 0.7 mm average absolute error and showed great potential for the carotid artery [146]. The feasibility of the tele-operated remote examination through the internet was also demonstrated successfully. However, the architecture of this robot is limited to small recti-lined segments such as the carotid artery.

In the cardiovascular sector, most developments have been so far oriented towards architectural control and safety designs. While meeting design and safety requirements are significantly important for US medical robotics, this does not necessarily guarantee that clinical needs are met. Consequently, it is very important that new medical hardware and software designs are validated. In just the past decade, some surgical robot prototypes have been FDA approved (e.g., ROBODOC, DaVinci, etc.). However, US medical robots have not yet been approved. This certifies that improvements for patient care and safety are still needed in US medical robots to ensure that the technology matures.

---

[27] Source: http://www.ece.ubc.ca/~tims/Ultrasound/index.html (Accessed: 03/05/2010).

2.5 Prototype 3D-US medical robot

Recently, a new medical 3D-US robotic imaging system was developed by our team [147, 148] to provide accurate 3D-US scanning of lower limb vessels. This 3D-US imaging robotic system includes three principal components: the computer workstation, the robotic arm and the US scanning system. An overview of this system is shown in Figure 2.12. Our robotic arm is managed through custom made software installed on the computer workstation. Namely, the robotic arm carries the US probe to scan a volume. Then, B-mode or color Doppler images are acquired with corresponding probe positions for 3D-reconstruction.

This robotic system offers a great alternative for 3D-US imaging and quantification of lower limb stenoses. This is particular by true for the detection and the quantification of long tortuous arterial segments in lower limbs (approx. 80 cm in length) that require high positioning accuracy. Accurate 3D representation generated by this robotic system should be higher than 3D freehand systems since the volume is regularly sampled. In addition, it is thought to provide a satisfactory level of resolution comparable to other 3D imaging modalities given it incorporates a robotic arm to track 2D-US images. Most importantly, detection and quantification of stenosis performance should be enhanced with this new technology from the 3D reconstructed models of patients' lower limb vessels. Furthermore, therapy planning and follow up of diseased vessels can be more optimally managed.

Figure 2.12: The 3D-ultrasound (US) robotic imaging system. The F3 CRS robotic arm carries a probe from an US system (GE Vivid-5).

2.7 Objectives

The general objective of this thesis is to optimize and validate our prototype medical 3D-US imaging robotic system to localize and quantify arterial stenoses in lower limbs. At first, the performance of this system is evaluated without US images in terms of position and distance accuracies as well as repeatability with a lower limb-mimicking phantom. Secondly, with US images, the optimal calibration transform to register the B-scan into the robot's coordinate system for the most accurate 3D-US vessel representation is assessed. Then, the robotic system ability to localize and quantify stenoses is investigated *in vitro* on a replica of PAD and *in viv*o, on a patient with PAD disease. These results were compared to the one obtained with a clinical diagnostic imaging technology.

2.7.1 Thesis plan

The principal achievements of the thesis are presented in the form of scientific papers.

Chapter 3. This chapter introduces the first paper of our study and presents the performance evaluation of our medical robotic 3D-ultrasound imaging system. The prototype medical robot's architecture and operation are described in details. The robot's positioning and inter-target accuracies are assessed throughout the robot workspace with a lower limb mimicking phantom.

Chapter 4. In this chapter the second paper is presented. The validation of 3D reconstructions of a mimicked femoral artery with the ultrasound imaging robotic system is performed. A Z-phantom calibration procedure is showed and characterized to obtain the best 3D vessel representation. An *in vitro* femoral artery is used as gold standard.

Chapter 5. The third paper is given in the fifth chapter. The 3D-US imaging robotic system feasibly to localize and quantify lower limb arterial stenoses is performed. A short realistic multimode vascular phantom was used to evaluate *in vitro* the system's performance to represent a 3D vessel, to localize and quantify stenoses. Analyses were compared to the CTA, the clinical gold standard for 3D vascular imaging. The clinical feasibility to evaluate these parameters is also investigated *in vivo* on long lower limb vessels.

Chapter 6. We summarize the results of the thesis and put them in perspective to current work and discuss potential future work.

Annexes. We present US image characteristics, the conference proceedings related to work in chapters 3, 4 and 5 as well as the authorization from the editors for the reproduction of published papers.

Chapter 3

Performance evaluation of a medical robotic 3D-ultrasound imaging system

I'll be more enthusiastic about encouraging thinking outside the box when there's evidence of any thinking going on inside it.

Terry Pratchett

3.1 Forward

This chapter presents the published paper in the journal *Medical Image Analysis* by the authors Marie-Ange Janvier, Louis-Gilles Durand, Marie-Hélène Roy Cardinal, Isabelle Renaud, Boris Chayer, Pascal Bigras, Jacques de Guise, Gilles Soulez and Guy Cloutier[28].

This paper describes the methods used to evaluate the clinical performance of the robotic system. In most 3D-US imaging systems, the US probe positioning accuracy (i.e., tracking) is the cornerstone for anatomy models to be reconstructed accurately in 3D. Thus a lower limb mimicking phantom was conceptualized to simulate the vessels over long and tortuous segments starting from the iliac artery down to the popliteal artery below the knee. After, registration of this phantom in the robot referential, the robotic system, repeatability, positioning and inter-target accuracies (i.e., difference between measurements and ground true values) for the clinical evaluation of lower limb vessels were evaluated throughout the

[28] The co-authors Louis-Gilles Durand, Pascal Bigras and Jacques de Guise are responsible for the idea concept of the prototype medical 3D-US robot to detect lower limb arterial stenoses. Boris Chayer designed the lower limb-mimicking phantom. Isabelle Renaud provided expertise for the calibration algorithm and Marie-Hélène Roy Cardinal helped in editing and organizing the manuscript. The co-authors Gilles Soulez and Guy Cloutier also initiated the idea concept of the robotic US scanner and were the supervisors of the thesis.

robot workspace. A preliminary 3D vessel reconstruction was performed and stenoses were evaluated.

3.2 Abstract

3D-ultrasound (US) imaging systems offer many advantages such as convenience, low operative costs and multiple scanning options. Most 3D-US freehand tracking systems are not optimally adapted for the quantification of lower limb arterial stenoses because their performance depends on the scanning length, on ferro-magnetic interferences or because they require a constant line of sight with the US probe. Robotic systems represent a promising alternative since they can control and standardize the 3D-US acquisition process for large scanning distances without requiring a specific line of sight. The performance of a new prototype medical robot, in terms of positioning and inter-target accuracies (i.e., difference between measurements and ground truth values) was evaluated with a lower limb mimicking phantom throughout the robot workspace. The teach/replay repeatability (i.e., difference between taught and replayed points) was also assessed. A mean positioning accuracy between 0.46 mm and 0.75 mm was found on all scanning zones. The mean inter-target distance accuracy varied between 0.26 mm and 0.61 mm. Teach/replay repeatability below 0.20 mm was also obtained. Additionally, a 3D reconstruction of in-vitro stenoses was performed with the robotic US scanner. The quantification error of a 80 % area reduction (AR) stenosis was 3.0 %, whereas it was -0.9 % for a less severe 75 % AR stenosis. Altogether, these results suggest that the robot may be of value for the clinical evaluation of lower limb vessels over long and tortuous segments starting from the iliac artery down to the popliteal artery below the knee.

3.3 Introduction

Atherosclerosis is the major cause of peripheral arterial disease [149], which leads to progressive narrowing of lower limb arteries [27, 51]. Atheromatous infiltration in PAD is usually diffuse with more than one stenosis affecting adjacent vessels. Different PAD evaluation strategies are used in clinical practice. The ankle/brachial systolic blood pressure ratio measured with a cuff and a manometer is the oldest non-invasive index still utilized to

assess the global disease of lower limb vessels [150]. Pulsed-wave Doppler ultrasound (US) and color Doppler flow imaging are the most popular non-invasive imaging techniques currently in use to investigate the severity of specific lesions along the lower limb vascular tree [151, 152]. Nevertheless, in most centers, a pre-intervention mapping by digital subtraction angiography [36], magnetic resonance angiography [36] or computed tomography angiography (CTA) is necessary to provide a complete 3D representation of the lower limb vessels to plan an appropriate therapy [51]. With these 3D imaging methods, the scan is performed over long segments usually starting from the abdominal aorta within the abdomen, following with iliac, femoral, and then with popliteal arteries to end in the tibial vessels of the calf. Although these imaging technologies yield high image resolution and 3D rendering, they still do not exhibit the same benefits of US that is low-cost, non-invasive, non-ionizing, safe and painless. Additionally, US presents multiple options for the diagnosis such as blood flow information with color Doppler, angiographic images with power Doppler and atherosclerotic plaque visualization with B-mode scanning. However, conventional 2D-US assessment of atherosclerotic disease highly depends on the observer [89]. As a result, many 3D-US systems were developed and validated in various clinical applications notably obstetrics, cardiology, and vascular imaging to increase the US diagnosis confidence [75].

3D-US systems are based on two-dimensional arrays, mechanical localizers and freehand scanning with or without position sensing. Sensorless 3D-US systems include 2D linear array transducers (3D probes) [30] speckle decorrelation techniques [70] and pseudo-tracking [153]. Only small volumes can be scanned using 3D probes. In speckle decorrelation techniques, the transducer is moved manually and speckle motion measurements are used to determine the distance between 2D images. The decorrelation algorithm used to predict the correct distance thus strongly relies on small constrained movement of the US probe. This technique can provide 3D-reconstruction if the image spacing is accurately determined and if the US transducer parameters are well known. Yet, since this approach does not guarantee accurate distances, it is not used to measure organ size, area nor volumes. Pseudo-tracking is an option available on many US systems today. This mode produces a 3D reconstruction from a 2D image sequence acquired during a manual linear scan. However, it does not provide an accurate 3D reconstruction since

positions of 2D-US images are not tracked. Therefore, this approach is limited to scan regular geometries since a tortuous volume would be misrepresented as a linear one.

Sensor based 3D-US freehand systems include positioning information from tracking devices that are used to locate each 2D image in space and to reconstruct the sampled volume [71]. Optical tracking exploits properties of light to follow Light Emitting Diode (LED) markers distributed on a rigid structure with charged coupled device (CCD) cameras. Electromagnetic (EM) tracking measures the magnetic field between a transmitter attached to the US probe and a receiver. Limitations of optical systems are mainly the requirement of a constant line of sight [85, 112], and those of EM sensors are errors induced by metallic object interference and a variable performance depending on the scanning distance [85, 106, 154, 155]. Additionally, uneven volume sampling generated by the 3D-US freehand tracking method adds uncertainty to the reconstruction. Consequently, these devices are not well suited for lower limb vessel imaging, where the detection and quantification of long and tortuous arterial segments requires a high precision. In fact, a robust positioning accuracy of approximately 1 mm is likely needed for a tracking device to provide a competitive 3D-US quality analysis of stenoses in lower limb arteries.

Robotic systems represent a promising approach for stenosis quantification as they simultaneously control and standardize the 3D-US acquisition process for long scanning distances and complex geometries. Medical prototype robots have been developed to explore this advantage. For example, Hippocrate, a low-power robot actuated by slow stepper motors, is a force feedback medical robot that allows US and tonometry measurements with heart rate synchronization [140]. While preliminary *in vivo* results looked promising, the main innovation of this system was the development of a force controller with design strategies selected to meet safety requirements imposed by medical applications. To our knowledge, no follow-up studies can be found on this robot in the literature. Furthermore, no evaluation of the robot accuracy has been performed. Other systems such as an image-guided control instrument [146] and a tele-robot [156] were developed for 3D-US scanning. The first system was designed for the tele-examination of carotid arteries on short rectilinear paths. The control of the US probe movement is shared between the operator, the robot controller and the US image processor. This system

produces autonomous tracking of the vessel contour in real-time scans to compensate for the physiological motion of an artery during probe motion along a 1D trajectory. Thus, the US probe movement is controlled in 3 degrees of freedom (DOF) that are constrained to lie in the US observation plane. Nevertheless, this robot operates within a limited range in the robot workspace and is restricted to straight line objects of interest (i.e., no tortuous curved objects) to obtain visual information. Certainly, the principal accomplishments of this robot remain the development of ultrasound visual servoing and control that enable a remote assistance for tele-operation. The second design is a tele-robotic system also with remote control assistance to facilitate hand-eye coordination necessary to perform echographic examination over the abdomen of pregnant women. It is to note that most developments have been so far oriented towards architectural control and safety designs. However, it is very important that new medical hardware and software designs be validated to meet specific clinical needs.

To provide accurate 3D US scanning of lower limb vessels, a prototype medical robot was recently developed by our team. A teach mode that enables the learning of a "freehand" scan, and a replay mode to reproduce the manually taught path are available. These features, which are also present in Hippocrate, accommodate specific scan routes with controlled speed. In addition, when coupled to an US probe, the system captures and stores images with their registered 3D spatial location at uniform spacing in replay mode. Furthermore, the robot was designed to have a constant high accuracy over its entire workspace. Thus, a clinician can integrate their regular scanning operation for each patient's leg by manually teaching a scan path to the robot. The robot replays the path over the leg and acquires 2D images for 3D reconstruction. The reconstructed vessel segments consequently remain within the US image plane obtained on a pre-determined trajectory for each patient scan. A sub-objective of this study was to use a double-stenosis vascular phantom to evaluate the feasibility of accurate quantification of stenoses in 3D with the prototype robotic scanner.

3.4 Materials

3.4.1 Prototype medical robot

The robot includes three principal components: the computer workstation, the robotic arm and the US scanning system. An overview of this system is shown in Fig. 3.1. The robotic arm is managed through a custom made software installed on the computer workstation. Namely, the robotic arm carries the US probe to scan a volume. Then, B-mode images are acquired with corresponding probe positions for 3D-reconstruction.

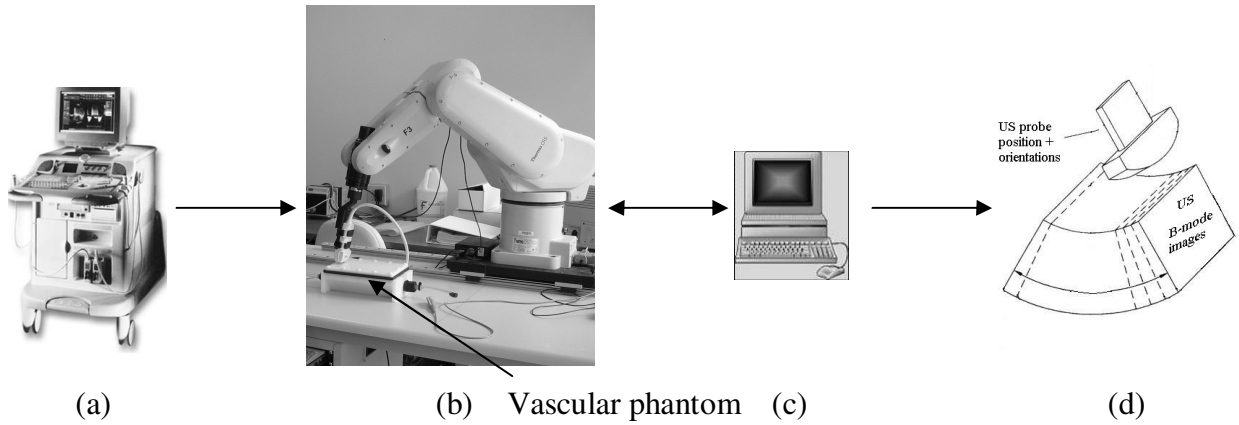

Figure 3.1: The 3D-ultrasound (US) robotic imaging system. The F3 CRS robotic arm (b) carries a probe from an US system (GE Vivid-5) (a). The robotic arm is moved through the user interface software on the workstation (c). 2D US images are tagged with the US probe positions acquired from the robotic arm (d). In this example, a vascular phantom is scanned.

The URS software (Ultrasound Robotic Scanner, Integral Technologies Inc., Laval, Québec, Canada), which runs on the workstation, provides a user interface to access and set-up the robot controls, movements, parameters and tasks. This specialized software was developed in Visual C++ and run under Windows. This higher control architecture allows three operative states for the robotic arm: teach, replay and idle modes. In teach mode, the operator manually moves the robotic arm while the robot controller uploads the real time arm positions to the workstation; the positions are then saved in a trajectory file. Thereafter, in replay mode, the saved trajectory file is sent back to the robotic arm into movement commands. The replayed trajectory is executed at constant speed and contact pressure with the patient or object to be scanned. The last robot arm state is the idle mode where the operator can freely handle manually the arm without trajectory file processing. Also, the

software limits any tool attached to the robotic arm to a maximum linear speed of 50 mm/sec in addition to a maximum applied force (i.e., 100 N in the normal direction and 50 N in the transverse directions). Finally, the workstation communicates with the robot controller according to the RS-232 protocol.

The robot controller (CRS C500C, CRS Robotics Corporation) provides safety circuits, power and motion control for the robotic arm. It drives the motors in each joint, keeps track of motor position through feedback from encoders, computes trajectories and stores robot applications in memory. The modules implemented in the robot controller consist of the lower architecture control level. These modules were all written in the RAPL-3 programming language. They translate the position commands and move the arm as requested by the workstation. Additionally, the robot controller triggers the image acquisition and sends the corresponding arm position to the workstation.

The robotic arm is an industrial robot (F3 Articulated Robot, CRS Robotics Corporation, Burlington, Ontario, Canada). Note that many groups have used CRS industrial robots to develop specialized light-weight precision tasks. In particular, medical applications include image-guided surgery [157] and 3D transrectal ultrasound-guided prostate brachytherapy [133]. Our industrial manipulator is an articulated robotic arm designed for light payload applications (3 kg). Moreover, applications that require complex and flexible movements are recommended for this particular model. Our unit has 6 DOF with absolute encoders in each arm joint that provide continuous information on the arm stance and position to the robot controller. In our system, the robotic arm moves the US probe with commands from the workstation and information that comes from the force/torque sensor.

The force/torque sensor (F/T) (ATI, Industrial Automation, Apex, NC, USA) connected to the robotic arm is a key element of the 3D US scanner system. This sensor allows easy handling and precise positioning of the robot manipulator by the operator. Manual handling of the robotic arm is possible because the F/T sensor reports all forces and torques applied to the robot controller. This information is then transmitted to the workstation where forces and torques are converted into positioning information to move the arm and generate the trajectory file in teach, replay and idle modes. Additionally, in

replay mode, the workstation employs force feedback. This is performed with repetition of the same applied US probe pressure to the patient and safe monitoring of the threshold contact force.

The robotic system assures patient security through many safety controls. Two control schemes of watchdog mechanisms were added to the system in case of failure: one at the customized software and the other at the robot controller. The watchdog monitors continuous digital signals sent from the robot controller and the workstation. If the robot controller or workstation goes out of control or does not respond, the emergency stop (E-stop) is activated. Its activation immediately removes power from the robotic arm and fail-safe brakes are automatically engaged to prevent movements due to gravity. Moreover, the software monitors singularities of joint configurations, joint limits and tracks errors between desired and current positions. Furthermore, there is a maximum limit set for the US probe pressure and linear scanning speed. Also, three additional E-stop buttons, which can be manually triggered, are available in the robot operating workspace. Other safety designs include the operator button that needs to be pressed throughout the entire replay mode to ensure the monitoring of the replayed trajectory. It is to note that the Hippocrate robot as well contains similar security features [140].

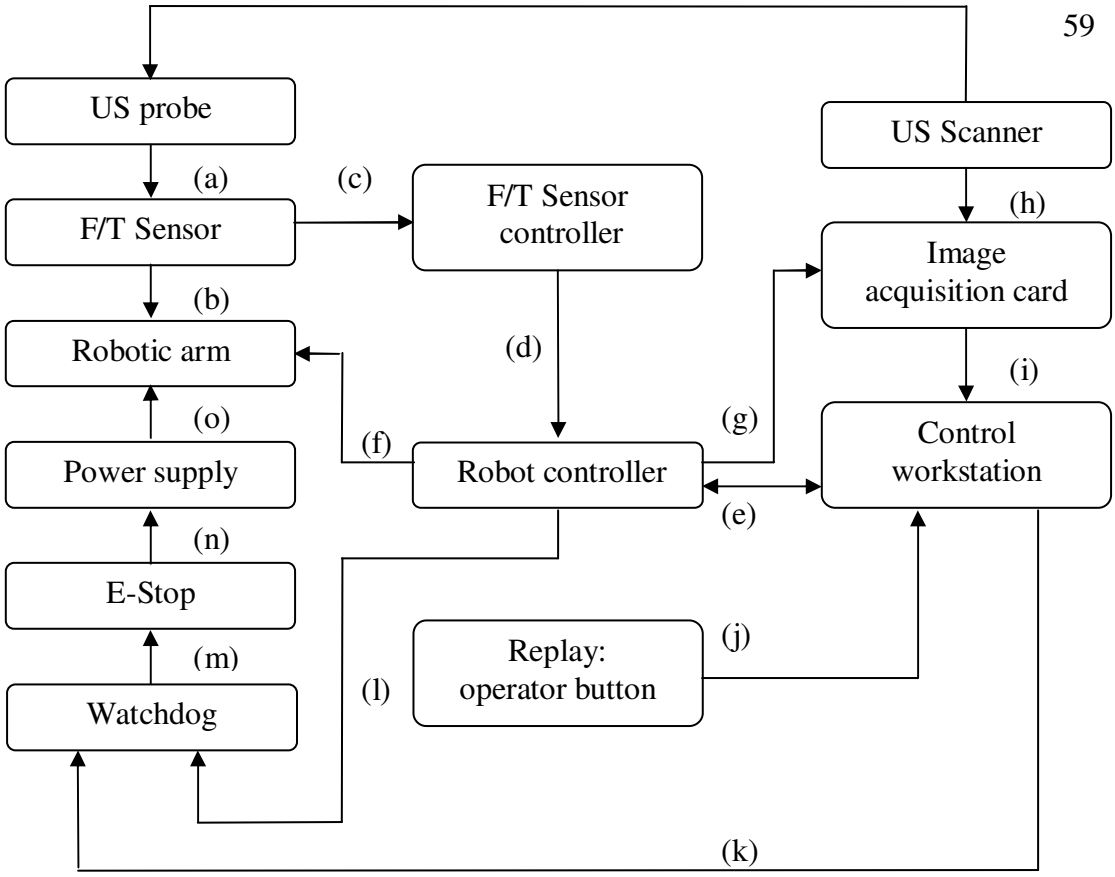

Figure 3.2: The 3D-ultrasonic robotic system block diagram. The US probe is attached to the force/torque (F/T) sensor (a) incorporated in the robotic arm (b). In teach mode, forces and torques applied to the sensor are sent to the F/T sensor controller (c) then to the robot controller (d). The robot controller translates forces and torques into positioning information that are transmitted and saved unto the control workstation (e). In replay mode, the workstation transfers the saved trajectory to the robot controller (e). The robot controller translates this trajectory into robotic positions and commands the robotic arm to move (f). At the same time, the robot controller uploads in real time the US probe location to the control workstation (e) and triggers the image acquisition card (g). 2D images are thus simultaneously acquired from the US scanner (h) and saved into the control workstation (i). Safety control is assured in replay mode with the operator button that monitors the robot movements and sends the information to the control workstation (j). Additionally, if any of the control workstation (k) or the robot controller modules fail (l), a watchdog mechanism activates the emergency stop (m) (E-stop). The E-stop activation automatically removes (n) all the power supplied to the robotic arm (o).

The last principal component is the US scanner. It provides images of a scanned volume in any available modalities (e.g., B-mode, color Doppler, power Doppler). Any US scanner for which it is possible to attach the US probe to the F/T sensor handle on the robotic arm can be used. In its current form, the robotic system provides its own digitization of US images. 2D-US images are captured at uniform spacing with an image acquisition card (PCI-1411, National Instrument, Austin, Texas, USA) mounted in the workstation. These US images are then digitized in 480 x 640 pixels format from the scanner video output. Simultaneously, US probe positions of the robotic arm are associated

to the acquired 2D-US images and saved into the workstation for 3D-reconstruction. Fig. 3.2 shows the complete 3D-US robotic system block diagram.

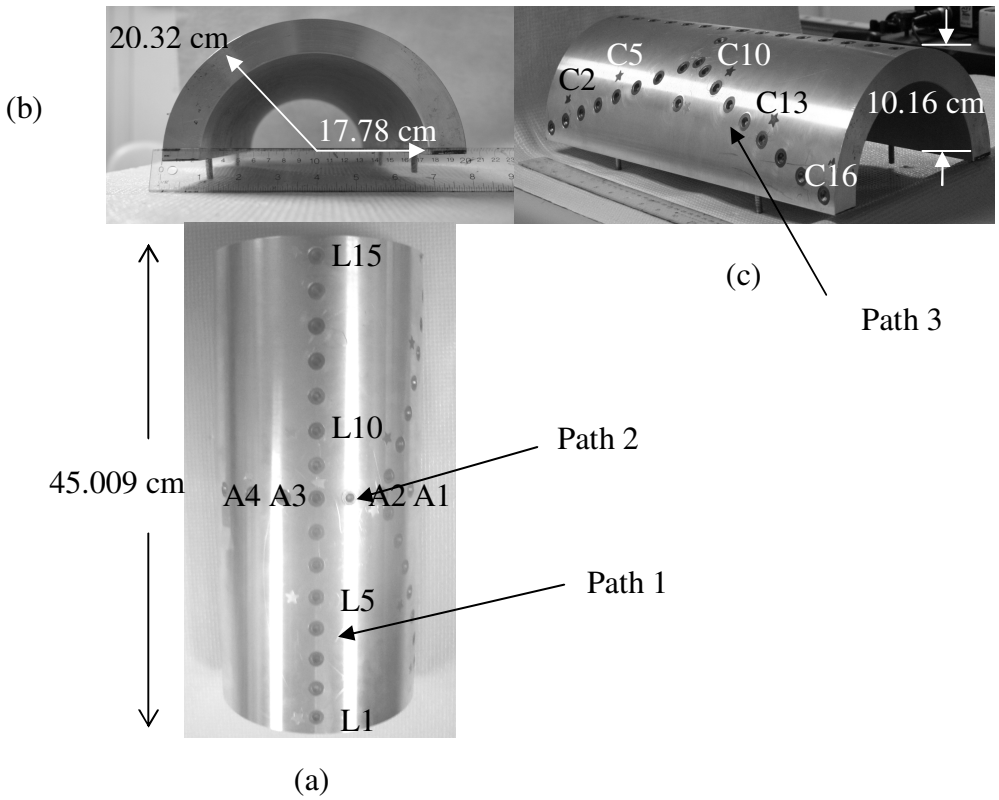

Figure 3.3: The lower limb mimicking phantom, top (a), axial (b) and side (c) views. The three paths represent classical lower limb vessel scanning trajectories. The phantom contains a total of 37 holes which serve as target points for the robotic spherical pointer (SP, see Fig. 3.4). A total of 13 holes were selected for the accuracy and teach/replay repeatability measurements. Path 1 is linear with 4 selected targets (L1, L5, L10 and L15). Path 2 represents the arc path with 4 selected targets (A1, A2, A3 and A4) and path 3 is curved with 5 targets (C2, C5, C10, C13 and C16). Each target point is labelled according to the corresponding path: L for linear, A for arc and C for curved.

3.4.2 Phantom model

A phantom was specially designed to assess the accuracy of the robot arm to position a spherical pointer (SP) within holes manufactured on a leg mimicking geometry. Fig. 3.3 shows the phantom where dimensions correspond to the upper half of a thigh and where holes are arranged in three different paths. The paths match classical US lower limb vessel scanning trajectories. They were designed in linear, arc and curved fashions (see Fig. 3.3). Paths 1, 2 and 3 contain 15, 6 and 16 holes, respectively. Each hole was manufactured with a precision of 0.03 mm, a 8.38 mm diameter and a 4.19 mm depth. To avoid

redundancy in the 3D space explored by the SP, the phantom was designed without collinear and coplanar points.

The SP at the robot end-effector replaced the US probe for the accuracy and teach/replay repeatability testing. Fig. 3.4 shows the SP added to the robotic arm where the spherical end fits tightly within the phantom holes. Various orientations were possible when the SP was in contact with the phantom target points. Even though the center of the SP was constrained to the center of a phantom hole, infinite configurations of the robot joints were possible. This method, also referred as the single endpoint contact method, is usually the preferred approach for robot calibration [158, 159].

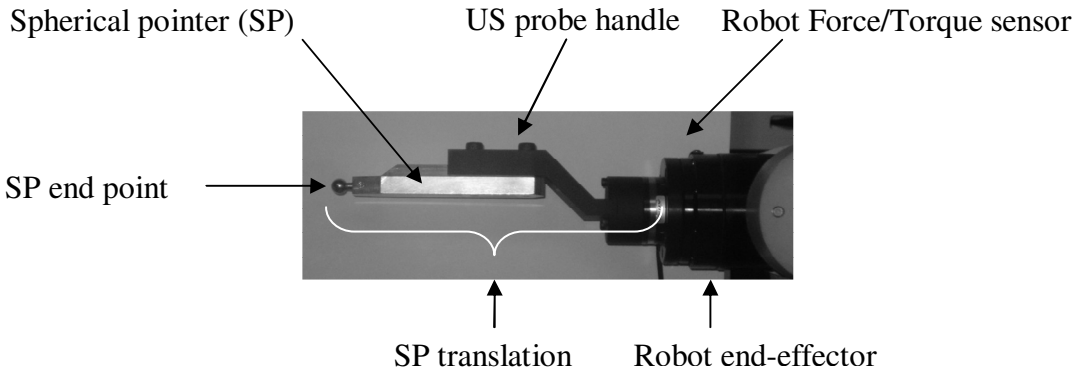

Figure 3.4: The spherical pointer used to determine the performance of the robotic US scanner. The SP is rigidly attached to the US probe handle that is linked to the robot end-effector. The SP translation is a vector that is estimated to make the SP center of gravity known in the robot referential.

The phantom was centrally positioned and fixed within each of five designated experimental zones in the robot workspace, as illustrated in Fig. 3.5. The orientation of the leg phantom in each experimental zone is given as well in Fig. 3.5a. The experimental zones were chosen to allow the identification of optimum operating areas in the robot workspace. Likewise, selected zones and phantom orientations were chosen to correspond to the expected scan positions of a patient lower limb during a clinical exam.

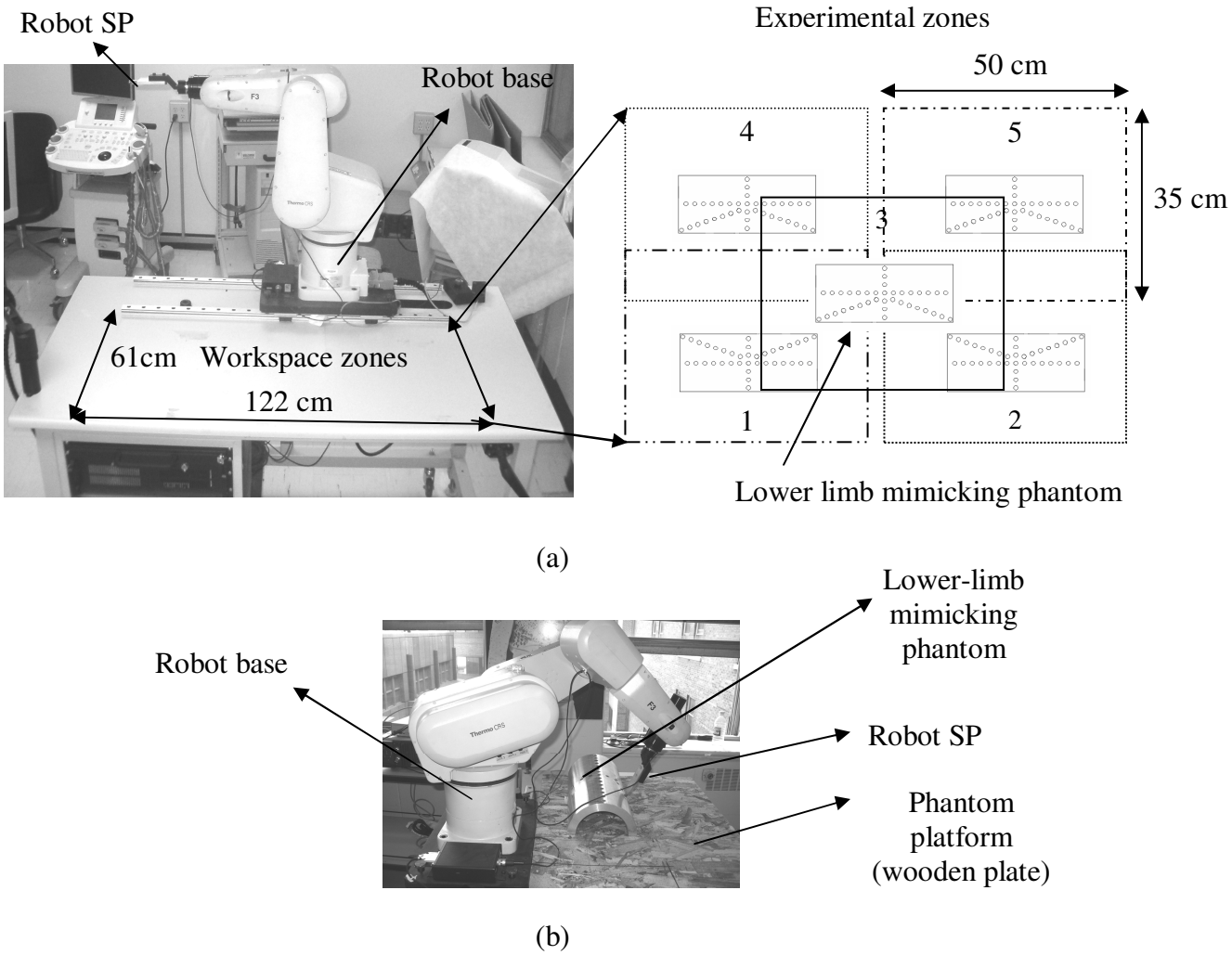

Figure 3.5: (a) The designated experimental zone in the robot workspace. The lower limb mimicking phantom was positioned in five different zones where the patient leg is most likely to be placed. (b) The phantom rigidly attached to the platform (wooden plate) with the robot spherical pointer (SP) inserted in one of the semi-spherical holes micro-machined in the phantom.

3.5 Methods

In order to evaluate the robot performance, the methods required to relate the coordinate system of the robot, to that of SP and of the phantom, as identified in Fig. 3.6. Because the SP was not considered in the robot referential, a calibration procedure was thus needed to determine the SP center of gravity with respect to the robot referential. Thereafter, the performance of the robot could be evaluated with the SP. It was quantified in terms of positioning and inter-distance accuracies (i.e., difference between measurements and ground truth values) with the phantom target points, and in term of teach/replay repeatability of the measures (i.e., difference between 'teach' and 'replay' points).

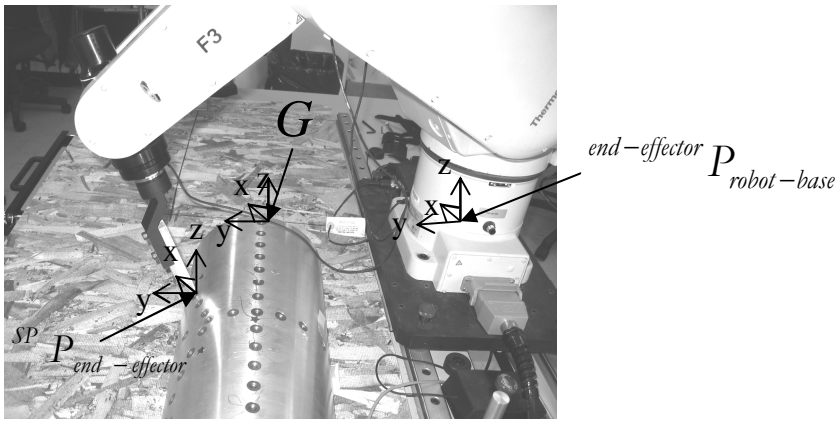

Figure 3.6: The three referential coordinate systems in this study: the robot ${}^{end-effector}P_{robot-base}$, the spherical pointer (SP) ${}^{SP}P_{end-effector}$ and the phantom G.

3.5.1 SP calibration

The robot reports the Cartesian position and orientation of its last joint or wrist, also referred as the end-effector. The SP coordinates could be transformed with respect to the base of the robot because the orientation and position of the end-effector were known. To perform the SP calibration, its translation with respect to the end-effector was calculated by using the following equation [93, 160, 161]:

$$ {}^{SP}P_{robot-base} = {}^{end-effector}P_{robot-base} + \left({}^{end-effector}R_{robot-base} \times {}^{SP}P_{end-effector} \right), \qquad (1) $$

where ${}^{SP}P_{robot-base}$ defines the unknown position vector of the SP center of gravity with respect to the robot referential, ${}^{end-effector}P_{robot-base}$ represents the known position vector of the robot end-effector in the base referential, ${}^{end-effector}R_{robot-base}$ describes the known Euler rotation matrices that transform the end-effector orientation in the robot referential, and ${}^{SP}P_{end-effector}$ is the unknown translation vector of SP in the end-effector referential. The positions P are 3x1 vectors and the rotation matrix R is 3x3. When a specific phantom target hole is reached several times with different tool configurations, Eq. (1) becomes over determined. Unknowns can thus be solved using the least-square method. Once the SP vector ${}^{SP}P_{end-effector}$

was estimated, the SP position for following experiments could be calculated in the robot referential with Eq. (1).

To perform the SP calibration, the robot arm was operated manually in idle mode. In each experimental zone of the robot workspace, two holes on phantom path 1 were randomly selected. For each hole and zone, the SP was rotated manually to 32 different positions distributed in a hemispherical pattern around each selected phantom target pivot. Cartesian position and orientation of the robot end-effector were then recorded for each SP configuration. The ${}^{SP}P_{end-effector}$ vector was estimated with Eq. (1) for each experiment (2 phantom holes in each of five robot workspace zones for a total of 10 estimated SP translations). The mean value of this vector was used as the SP translation for subsequent performance assessments.

3.5.2 SP calibration precision

A precision metric was evaluated since subsequent performance measurements to be reported below also depend on the SP translation precision. The precision was defined as the ability to locate the same point in space with small position variations. Since it is not physically possible to locate the origin of the robot coordinate system because it is inside the robot base, it was not possible to accurately measure the location of any object in the base coordinate system using rulers [155, 161, 162]. Thus, a point position acquired with the robot could not be compared with its true physical location. The SP precision $\overline{S}$ was computed by using:

$$\overline{S} = \frac{1}{TLM} \sum_{i=0}^{T} \sum_{j=0}^{L} \sum_{k=0}^{M} \sqrt{{\sigma_x}^2{}_{i,j,k} + {\sigma_y}^2{}_{i,j,k} + {\sigma_z}^2{}_{i,j,k}} \,, \qquad (2)$$

where $\sigma^2_{x\,i,j,k}$ is the variance for T=10 SP calibration configuration positions i in the x direction for the experimental zone j and target point k. This definition applies as well for the y and z directions. The average precision was calculated for L=5 zones, M=2 target holes randomly chosen among the selected path 1 (see Fig. 3.3a for the selected target point options) for a total sample size of 100 points. It is to note that the data collected for the SP

calibration was not used to assess the average SP precision.

3.5.3 Performance evaluation of the robot

The relative positioning accuracy, the inter-distance accuracy, and the teach/replay repeatability in locating the SP were assessed. The robot referential first needed to be transformed into the phantom coordinate system, as described earlier by Eq. (1). For that purpose, the position of the selected phantom points indicated in the legend of Fig. 3.3 was acquired with four different SP orientations randomly chosen ($T = 4$ in this case); a sample mean was computed for each target point. These mean values corresponded to the phantom theoretical central positions of the holes in the robot referential. In the phantom coordinate system, the ground truth position of each hole was known from the computer-assisted-design (CAD) file used to manufacture the mimicking leg. The translation offset between the phantom ground truth and the theoretical target points in the robot referential was then calculated. The offset ${}^{phantom}offset_{robot-base}$ was determined for all selected target points in each zone and it was averaged to obtain the position of the phantom with respect to the robot base. The translation value is different in each zone and consequently it had to be recomputed when the phantom was moved. With ${}^{phantom}offset_{robot-base}$ known in each zone, the phantom points targeted with the robot arm could be transformed into the phantom referential by using:

$$ {}^{phantom}P_{robot-base} = {}^{SP}P_{robot-base} + {}^{phantom}offset_{robot-base}, \qquad (3) $$

where ${}^{phantom}P_{robot-base}$ defines the 3x1 position vector of the center target point of the hole acquired with the robot and transformed into the phantom coordinate system, ${}^{SP}P_{robot-base}$ is the 3x1 position vector of the SP center of gravity with respect to the robot referential, and ${}^{phantom}offset_{robot-base}$ is the 3x1 translation offset vector to position the robot base in the phantom referential. It can be recalled that Fig. 3.6 illustrates the three referential objects of this study: the robot, the phantom and the SP.

3.5.3.1 Position and inter-distance accuracies

The robot positioning and inter-distance accuracies were evaluated with the leg mimicking phantom on a total of 13 target points (see Fig. 3.3). The same targets were evaluated in each robot experimental zone and for each hole, taught and replayed data were collected. In teach mode, the operator manually moved the SP to a phantom target point. The robot arm then replayed the taught path to reach the same target. Data collection consisted of the Cartesian position and orientation of the robot end-effector (using $T = 4$, as mentioned earlier). The robot end-effector position and orientation for all collected data were transformed into the robot referential with Eq. (1). Data positions were then transformed from the robot referential into the phantom coordinate system with Eq. (3).

The relative positioning accuracy $\overline{Ps}$, calculated with Eq. (4), is the mean distance between the phantom ground truth point positions and the phantom points collected with the robot SP and transformed in the phantom referential. The inter-distance accuracy $\overline{IntDist}$, given by Eq. (5), evaluates the robot error in segment length measurements; it is the mean absolute error between the length separating phantom ground truth neighbor points and the length separating the corresponding target points collected with the robot SP:

$$\overline{Ps} = \frac{1}{TM}\sum_{i=0}^{T}\sum_{k=0}^{M}\left\| G^k - {}^{phantom}P^{i,k}_{robot-base} \right\| , \qquad (4)$$

$$\overline{IntDist} = \frac{1}{T(M-1)}\sum_{i=0}^{T}\sum_{k=1}^{M-1}\left| \left\| G^{k+1} - G^k \right\| - \left\| {}^{phantom}P^{i+1,k+1}_{robot-base} - {}^{phantom}P^{i,k}_{robot-base} \right\| \right| . \qquad (5)$$

In Eqs. (4) and (5), G^k defines the 3x1 ground truth position vector of target point k obtained from the CAD file of the designed phantom, ${}^{phantom}P^{i,k}_{robot-base}$ describes the 3x1 robot target point position vector transformed into the phantom referential of target point k for the SP configuration i, $T = 4$ corresponds to the different SP configurations taken around the target point, and $M = 13$ is the number of selected phantom target points. $\overline{Ps}$ and $\overline{IntDist}$ were evaluated in each robot workspace zone ($L = 5$). The inter-distance accuracy $\overline{IntDist}$ was computed for only neighbor target points pair in a specific path (e. g.,

in path 1, inter-distance pairs included L1-L5, L5-L10 and L10-L15). As a result, a smaller data sample was used for this evaluation.

3.5.3.2 Teach/replay repeatability

The teach/replay repeatability is the distance between the robot teach and replay points. It was assessed with the data collected for the robot accuracy measurements. For this analysis, it was not necessary to know the translation of the data in the phantom coordinate system; the collected data were only transformed into the robot referential with Eq. (1). The teach/replay repeatability $\overline{Rpt}$ was calculated with:

$$\overline{Rpt} = \frac{1}{TM}\sum_{i=0}^{T}\sum_{k=0}^{M}\left\| {}^{SP}P_{robot-base}^{teach\ \ i,k} - {}^{SP}P_{robot-base}^{replay\ \ i,k} \right\| \qquad (6)$$

where ${}^{SP}P_{robot-base}^{teach\ \ i,k}$ is the teach position vector with respect to the robot referential of target point k for the SP configuration i, ${}^{SP}P_{robot-base}^{replay\ \ i,k}$ represents the replay position vector with respect to the robot referential of target point k for the SP configuration i, $T = 4$ is the number of SP configurations, and $M = 13$ is the number of target points. $\overline{Rpt}$ was evaluated in each robot workspace zone ($L = 5$).

3.5.3.3 Statistical analyses

Multiple pairwise comparisons with Bonferonni tests were performed on accuracy and teach/replay repeatability results to evaluate differences among the robot operating zones and phantom paths. All statistical analyses were performed with the SPSS statistical software (version 13.0, SPSS Inc., Chicago, IL).

3.5.4 3D-US reconstruction of a vascular phantom from a robot scan

The performance of the 3D-US robotic system for the reconstruction of a vessel was evaluated by using a symmetric cylindrical vascular phantom of known length with two consecutive stenoses of 80 % and 75 % area reductions. The fabrication phantom ground truth values were obtained from micro-caliper measurements performed on the low-melting

point vessel lumen prototype. Fig. 3.7 shows the vascular phantom box and lumen mold. A complete description of the fabrication process, characteristics and geometric accuracy of the phantom is available in [163].

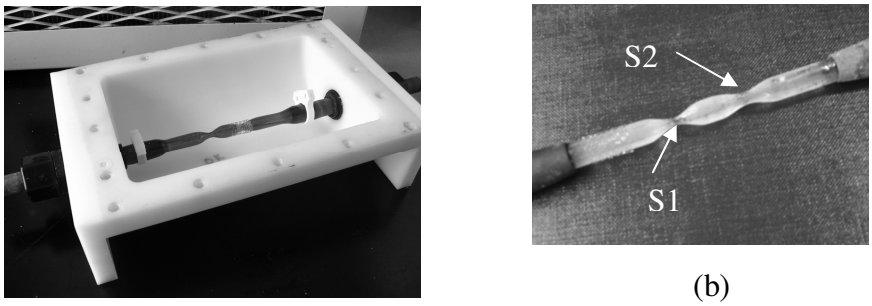

(a) (b)

Figure 3.7: The symmetric cylindrical vascular phantom. (a) The lumen mold of the vascular phantom with double stenoses is shown without the box top cover and the agar-mimicking tissue material used to fill the phantom. (b) A view of the lumen mold alone is shown, labels S1 and S2 correspond to the first and second stenoses with 80 % and 75 % area reductions, respectively. The sugar-based lumen mold is removed when the fabrication process is completed by introducing the phantom in water. This allows producing a vessel with two stenoses that is filled with degassed water for ultrasound scanning.

For the current evaluation, the vascular phantom was placed in zone 3 of the robot workplace (see Fig. 3.5) and scanned along its length. The robotic system was coupled to an US scanner equipped with a 10 MHz linear array probe (Model FPA, Vivid-5 US system, General Electric, Chicago, IL, USA). In order to reconstruct the vascular phantom accurately, a 3D-US calibration was first performed by using a cross-wire phantom. Thereafter, the quantification of the diameter and area reduction of stenoses was performed on the reconstructed volume obtained from US images captured with the robot system.

3.5.4.1 Calibration with a cross-wire

To locate US images within the robot coordinate system, it was necessary to find the transformation (rotation and translation) of the US image plane with respect to the probe position. This was achieved with a cross-wire calibration phantom made with two crossed threads suspended in water. Several scans were performed with a wide range of US probe angles and positions. The intersection of the two wires was aligned in the US image for a specific depth. The center of the intersection was manually segmented and considered as the origin of the phantom coordinate system to solve the following equation [71]:

$$\begin{pmatrix} 0 \\ 0 \\ 0 \\ 1 \end{pmatrix} = T_{robot-base}^{phantom} \cdot T_{USprobe}^{robot-base} \cdot T_{image}^{USprobe} \cdot \begin{pmatrix} s_x \cdot u_k \\ s_y \cdot v_k \\ 0 \\ 1 \end{pmatrix}, \qquad (7)$$

where $T_{robot-base}^{phantom}$ is the unknown transformation (rotation and translation) of the cross-wire phantom with respect to the robot referential, $T_{USprobe}^{robot-base}$ represents the known transformation of the US probe with respect to the robot referential for an acquired image, and $T_{image}^{USprobe}$ is the unknown transformation of the image with respect to the US probe. For each image *k,* u_k and v_k represent the column and row indices with respect to the B-scan origin; s_x and s_y are defined as the scaling parameters in mm/pixel estimated from the B-scan depth settings. A Levenberg-Marquadt iterative algorithm was employed to compute the unknown parameters since the cross-wire position is undefined in the robot referential. Once the calibration matrix $T_{image}^{USprobe}$ is determined, all cross-wire points in the acquired images were reconstructed in the robot referential with Eq. (7) to assess the calibration precision C_{rms} :

$$C_{rms} = \sqrt{\frac{\sum_{i=1}^{N} \sigma_i}{N}}, \qquad (8)$$

where σ_i is the standard deviations of the reconstructed points for an US image *i* among a total of *N* images.

3.5.4.2 3D-US reconstruction

A US scan with quasi-parallel planes of the phantom was taught and replayed by the robot. B-mode images (480 x 640 pixels) were captured, digitized and stored on the workstation. Images were cropped to a region of interest and then segmented by using a fast-marching method based on gray level statistics and gradients adapted from [41]. It provided an outline of the phantom vessel wall boundary. Each segmented contour pixel position (u_k, v_k) was then mapped to the reconstruction volume *B* with the calibration matrix $T_{image}^{USprobe}$, their respective scaling factors (s_x, s_y) and with the corresponding US

probe transformation parameters $T_{USprobe}^{robot-base}$. Thus, each pixel x^B of the 3D surface reconstruction was expressed by the following equation:

$$x^B = T_{USprobe}^{robot-base} \cdot T_{image}^{USprobe} \cdot \begin{pmatrix} s_x \cdot u_k \\ s_y \cdot v_k \\ 0 \\ 0 \end{pmatrix}. \quad (9)$$

The transformed contours were re-sampled on a rectangular grid and interpolated to provide a 3D surface rendering.

3.5.4.3 Quantification of stenoses

Stenoses were evaluated from the 3D-reconstruction. The reconstructed volume was re-sliced perpendicularly to the longitudinal axis of the vessel. A mean diameter and an area were computed for each cross-section. From this data set, 10 samples in regions where the area was maximum were used to compute the average dimension of the reference vessel A_{ref}. In regions where the area was minimum (within stenoses), one value was used to compute the average diameter and area of the reduced stenosis $A_{\min}$. Stenoses in the 3D volume were quantified according to the following equation:

$$\% \text{ of reduction} = 100 \times \left(\frac{A_{ref} - A_{\min}}{A_{ref}} \right). \quad (10)$$

The quantification error for both stenoses was determined and compared to the fabricated phantom ground truth values obtained from micro-caliper measurements.

3.6 Results

3.6.1 SP calibration

The SP translation magnitude ${}^{SP}P_{end-effector}$ in Eq. (1) was estimated as 194.33 ± 0.36 mm. The corresponding translation position coordinates, which represent the SP center of gravity in the *x*, *y* and *z* directions with respect to the robot end-effector, are listed in Table 2.

Table 2: Spherical pointer (SP) calibration results

SP	Position vector			Magnitude
${}^{SP}P_{end-effector}$	X	Y	Z	$\left\|{}^{SP}P_{end-effector}\right\|$
Mean (mm)	-12.05 ± 0.64	-1.38 ± 0.27	194.50 ± 0.35	194.33 ± 0.36

${}^{SP}P_{end-effector}$ is the estimated translation vector of the SP in the end-effector referential.

3.6.2 SP calibration precision

The mean SP precision according to Eq. (2) was found to be 0.57 ± 0.30 mm for the five experimental zones. This mean was calculated with 100 collected points in the robot workspace. Fig. 3.8 presents the histogram of the distance between each target position acquired with the SP and the corresponding mean target position. Most data acquired at different angulations of the SP resulted in a precision below 1 mm.

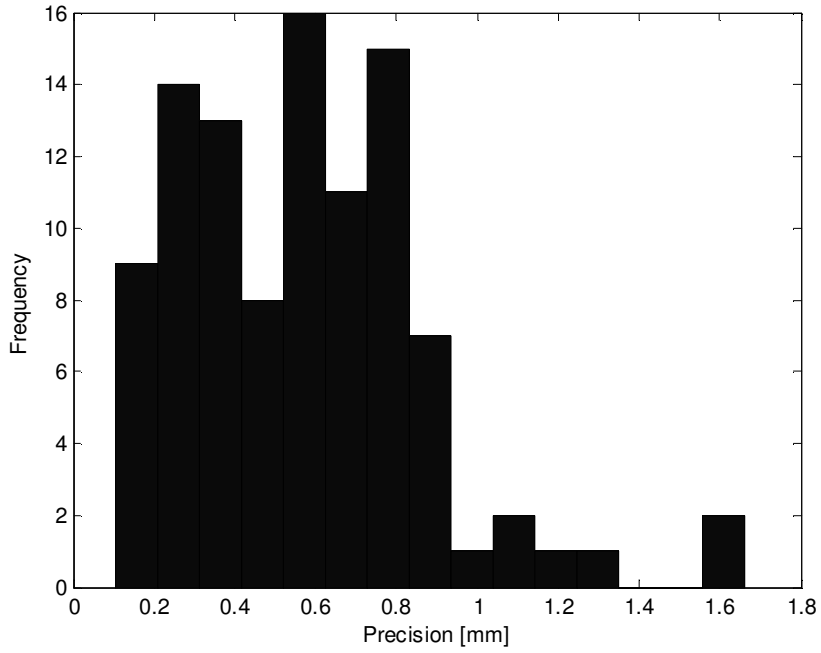

Figure 3.8: The precision histogram of the robot scanner determined by using the spherical pointer. For the five experimental zones, a mean of 0.57 ± 0.30 mm was found.

3.6.3 Performance evaluation

3.6.3.1 Positioning accuracy

The mean relative positioning accuracy calculated with Eq. (4) was 0.60 ± 0.29 mm in teach mode, while it was 0.62 ± 0.29 mm in replay mode. Ninety five percent of the data points (248 instead of 260 samples) was collected in teach and replay modes given that some holes were not reachable by the robot. Table 3 details the positioning accuracy within each designated experimental zones and different phantom paths for teach and replayed points. Statistically significant differences were found between the robot experimental zones ($p < 0.05$) for both $\overline{Ps}_{teach}$ and $\overline{Ps}_{replay}$ measurements. The pairwise comparisons revealed a significantly higher positioning error in zone 1 compared to zones 2 and 5 ($p < 0.001$ and $p < 0.05$, respectively). Furthermore, over all robot workspace zones and for both $\overline{Ps}_{teach}$ and $\overline{Ps}_{replay}$, a statistically significant difference between phantom paths 3 and 1 was found ($p < 0.05$) with the smallest error in the linear path (path 1). However, no statistically significant difference was found between the teach and replay positioning accuracy over all zones and phantom paths ($p = 0.67$).

Table 3: Robot positioning accuracy

Experimental zones	Phantom paths	$\overline{Ps}_{teach}$ (mm)	$\overline{Ps}_{replay}$ (mm)	Sample size (N)
Zone 1	1	0,69 ± 0,26 *	0,69 ± 0,28 *	12
	2	0,74 ± 0,33	0,75 ± 0,33	16
	3	0,69 ± 0,30 *	0,70 ± 0,30 *	16
	mean	0,71 ± 0,29 ξ, δ	0,72 ± 0,30 ξ, δ	44
Zone 2	1	0,46 ± 0,27 *	0,59 ± 0,30 *	16
	2	0,46 ± 0,18	0,49 ± 0,19	16
	3	0,55 ± 0,28 *	0,60 ± 0,29 *	20
	mean	0,50 ± 0,25 ξ	0,56 ± 0,27 ξ	52
Zone 3	1	0,48 ± 0,19 *	0,47 ± 0,18 *	16
	2	0,64 ± 0,26	0,60 ± 0,28	16
	3	0,72 ± 0,35 *	0,73 ± 0,34 *	20
	mean	0,62 ± 0,29	0,61 ± 0,29	52
Zone 4	1	0,61 ± 0,27 *	0,61 ± 0,27 *	16
	2	0,52 ± 0,29	0,49 ± 0,25	16
	3	0,72 ± 0,37 *	0,75 ± 0,42 *	20
	mean	0,63 ± 0,32	0,63 ± 0,34	52
Zone 5	1	0,54 ± 0,25 *	0,56 ± 0,22 *	16
	2	0,63 ± 0,21	0,62 ± 0,23	16
	3	0,56 ± 0,24 *	0,55 ± 0,22 *	16
	mean	0,58 ± 0,23 δ	0,58 ± 0,22 δ	48
All zones	Total mean	0,60 ± 0,29	0,62 ± 0,29	248

$\overline{Ps}$ is the relative mean positioning accuracy which defines the mean distance between ground truth and robot measured phantom points. It was calculated in the robot teach ($\overline{Ps}_{teach}$) and replay ($\overline{Ps}_{replay}$) modes. δ and ξ indicate statistically significant differences between experimental zones from pairwise comparisons with $p < 0.05$ and $p < 0.001$, respectively. * signifies that a statistically significant difference between paths was found over all robot workspace zones for both teach and replay modes with $p < 0.05$.

3.6.3.2 Inter-distance accuracy

The mean inter-distance accuracy computed with Eq. (5) in teach mode ($\overline{IntDist}_{teach}$) was 0.43 ± 0.32 mm, whereas for the replay mode, $\overline{IntDist}_{replay}$ was 0.42 ± 0.33 mm. Seventy eight percent (188 over 240 holes) of the data points was used for the robot inter-distance accuracy measures in teach and replay modes. This is due to the fact that this evaluation was limited to neighbor targets located on a specific path and because of the limited reach of the robot to some holes. Table 4 shows the inter-target distance accuracies. For both $\overline{IntDist}_{teach}$ and $\overline{IntDist}_{replay}$, statistically significant differences were observed between the robot operating zones ($p < 0.05$). The pairwise comparisons showed that the inter-target measurement error in zone 4 was significantly higher than in zones 2

and 5 (both with $p < 0.05$). Furthermore, for both $\overline{IntDist}_{teach}$ and $\overline{IntDist}_{replay}$, no significant differences occurred between phantom paths ($p = 0.24$) and between teach and replay modes ($p = 0.60$).

Table 4: Robot inter-distance accuracy

Experimental zones	Phantom paths	$\overline{IntDist}_{teach}$ (mm)	$\overline{IntDist}_{replay}$ (mm)	Sample size (N)
Zone 1	1	0,56 ± 0,43	0,54 ± 0,41	8
	2	0,52 ± 0,23	0,51 ± 0,22	12
	3	0,32 ± 0,16	0,32 ± 0,14	12
	mean	0,45 ± 0,29	0,45 ± 0,27	32
Zone 2	1	0,37 ± 0,13	0,44 ± 0,22	12
	2	0,34 ± 0,28	0,35 ± 0,29	12
	3	0,29 ± 0,21	0,31 ± 0,21	16
	mean	0,33 ± 0,21 δ	0,36 ± 0,24 δ	40
Zone 3	1	0,33 ± 0,17	0,33 ± 0,15	12
	2	0,37 ± 0,28	0,35 ± 0,29	12
	3	0,57 ± 0,35	0,59 ± 0,35	16
	mean	0,43 ± 0,30	0,44 ± 0,30	40
Zone 4	1	0,34 ± 0,27	0,34 ± 0,25	12
	2	0,57 ± 0,52	0,61 ± 0,43	12
	3	0,63 ± 0,55	0,61 ± 0,53	16
	mean	0,44 ± 0,40 δ	0,47 ± 0,36 δ	40
Zone 5	1	0,26 ± 0,18	0,40 ± 0,30	12
	2	0,48 ± 0,35	0,50 ± 0,35	12
	3	0,27 ± 0,28	0,26 ± 0,27	12
	mean	0,34 ± 0,29 δ	0,38 ± 0,32 δ	36
All zones	Total mean	0,43 ± 0,32	0,42 ± 0,33	188

$\overline{IntDist}$ evaluates the robot error in segment length measurements; it is the mean absolute error between the length separating phantom ground truth neighbor points and the length separating the corresponding target points collected with the robot spherical pointer (SP). It was calculated for the robot teach ($\overline{IntDist}_{teach}$) and replay ($\overline{IntDist}_{replay}$) modes. δ indicates a statistically significant difference between experimental zones on pairwise comparisons with $p < 0.05$. No statistically significant difference was found between phantom paths.

3.6.3.3 Teach/replay repeatability

Finally, the teach/replay repeatability computed with Eq. (6) was 0.10 ± 0.22 mm. Table 5 summarizes the robot teach/replay repeatability measurements. No significant differences occurred between robot workspace zones ($p = 0.78$) and between different paths ($p = 0.98$) within each zone.

Table 5: Robot teach/replay repeatability

Experimental zones	Phantom paths	$\overline{Rpt}$ (mm)	Sample size (N)
Zone 1	1	0,13 ± 0,18	12
	2	0,08 ± 0,10	16
	3	0,04 ± 0,02	16
	mean	0,09 ± 0,13	44
Zone 2	1	0,18 ± 0,05	16
	2	0,05 ± 0,06	16
	3	0,12 ± 0,22	20
	mean	0,12 ± 0,26	52
Zone 3	1	0,06 ± 0,04	16
	2	0,16 ± 0,31	16
	3	0,05 ± 0,05	20
	mean	0,09 ± 0,18	52
Zone 4	1	0,04 ± 0,02	16
	2	0,15 ± 0,15	16
	3	0,20 ± 0,40	20
	mean	0,14 ± 0,30	52
Zone 5	1	0,10 ± 0,23	16
	2	0,07 ± 0,08	16
	3	0,07 ± 0,15	16
	mean	0,08 ± 0,16	48
All zones	Total mean	0,10 ± 0,22	248

$\overline{Rpt}$ is the mean teach/replay repeatability which defines the distance between the robot teach and replay points. No statistically significant difference was found between the different zones and paths.

3.6.4 3D-US reconstruction of a vascular phantom from a robot scan

3.6.4.1 Calibration with the cross-wire phantom

The calibration matrix $T_{image}^{USprobe}$ was computed with 62 images at a depth of 6 cm with a cross-wire. The calibration precision C_{rms} achieved was 2.5 mm (see Eq. (8)).

3.6.4.2 3D-US reconstruction

The phantom with two stenoses was scanned also at a depth of 6 cm. A total of 83 images was captured to reconstruct the vascular phantom. Images were segmented and re-sampled in a 20 x 20 x 300 grid. The surface rendering achieved with the 3D-US system is shown in Fig. 3.9.

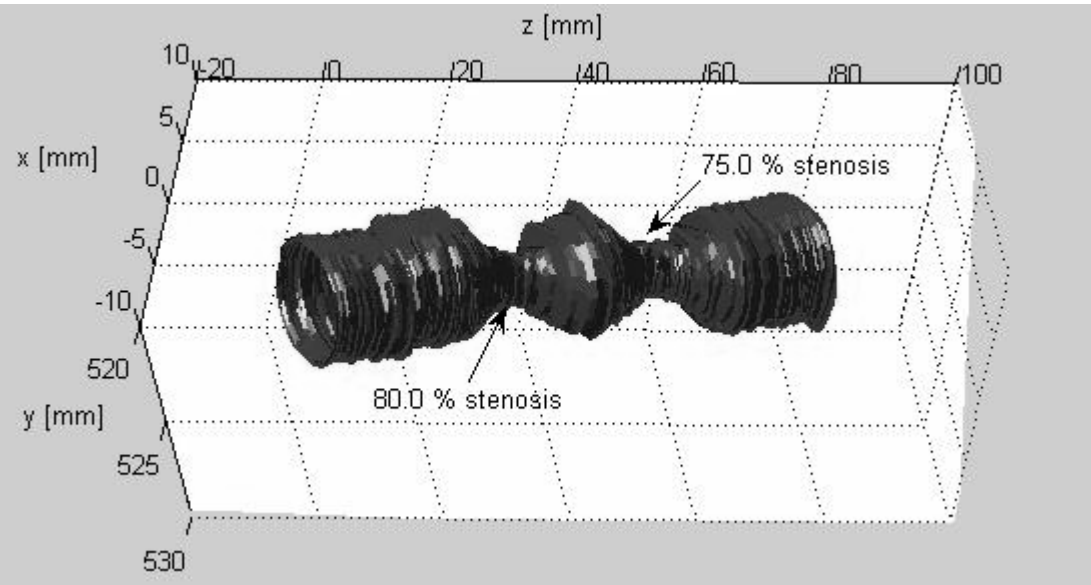

Figure 3.9: The 3D–ultrasound reconstructed phantom with double stenoses. Quantification errors of 3.0 % and -0.9 % were found for the 80 % and 75 % area reduction stenoses, respectively.

3.6.4.3 Stenosis evaluation

Table 6 shows quantification errors of 3.0 % and -0.9 % for the 80 % and 75 % stenoses, respectively. Additional details on diameter measurements and 3D reconstruction of the phantom are given in Table 6.

Table 6 : Vascular phantom 3D reconstruction results

Vessel parameters	In-vitro phantom	3D reconstruction	Error between the phantom model and the 3D reconstruction
Normal lumen wall diameter	7.98 ± 0.20 mm	7.08 ± 0.36 mm	- 0.90 ± 0.16 mm
1st stenosis diameter	3.57 ± 0.20 mm	2.93 mm	- 0.64 mm
1st stenosis area reduction ratio	80.0 %	83.0 %	3.0 %
2nd stenosis diameter	3.99 ± 0.20 mm	3.62 mm	- 0.37 mm
2nd stenosis area reduction ratio	75.0 %	74.1 %	-0.9%

3.7 Discussion

3.7.1 SP calibration and precision

The SP calibration resulted in a low variability of 0.36 mm (Table 2). Additionally, the precision was close to 0.6 mm over the whole robot workspace indicating an accurate calibration procedure (see Fig. 3.8). This means that the location of an image acquired with an US probe rigidly attached to the robotic arm handle is expected to be accurately found anywhere in the robot workspace. To assure an accurate SP calibration and constant precision, the robot arm had to be periodically re-homed. This is due to gradual drift in and out of calibration after long periods for which the robot was not operated.

3.7.2 Performance evaluation

3.7.2.1 Positioning accuracy

The positioning accuracy was below 0.75 mm for both teach and replay modes (see Table 3). Evermore, it was comparable to the precision of the SP calibration. This observation proves again the consistency of the robot, where the relative positioning accuracy reflects the precision of the robotic arm combined to the precision of the SP calibration procedure. Furthermore, zone 1, the furthest to the robotic arm, showed the worst mean positioning accuracy, as shown in Table 3. When zone 1 was compared to zones 2 and 5, which had the best mean positioning accuracy with values below 0.63 mm, a statistically significant difference was found. The poorer accuracy was due to the mechanical stress in the robotic arm to reach the phantom target points within zone 1. A smaller sample number of 11 target points was indeed used in zone 1 because some targets were out of reach to the robotic arm. While the robot offered an overall acceptable accuracy in its workspace, an optimum setting would be where the robotic arm can reach its target such as in zone 2 or zone 5. Therefore, for a 3D US scan, a patient leg could be placed anywhere in the robot workspace, but the robotic arm positioning accuracy would be better for a leg located within an area closer to its reach.

Concerning the robot scanning paths, the statistical analysis singled out a difference between paths 1 and 3. This can be observed in Table 3 specifically in zones 3 and 4, where path 3 showed a significant higher positioning error then path 1. Consequently, scanning of tortuous lower limb arterial segments, such as modeled with the curved scanning path 3, does increase the mechanical stress on the robotic arm, however the difference in the positioning accuracy was nevertheless low (≤ 0.20 mm).

3.7.2.2 Inter-distance accuracy

The inter-distance accuracy was found satisfactory within all robot workspaces (mean accuracy of 0.43 ± 0.32 mm in teach mode and 0.42 ± 0.33 mm in replay mode). In fact, absolute mean distances were always ≤ 0.63 mm. The inter-distance accuracy in Table 4 showed differences between zones. Zone 4 had the largest variations between 0.34 mm and 0.63 mm, and zones 2 and 5 again corresponded to the optimal regions with the lowest variations between 0.26 mm and 0.48 mm. However, no differences were found between the phantom paths. Hence, in the robot workspace, the optimum zones to perform inter-distance evaluation are again zones 2 and 5 where the mean inter-distance accuracies stayed ≤ 0.48 mm. The inter-distance measure is an important parameter as it evaluates the robot error in segment length measurements, which can condition the choice of a therapy (surgical bypass or endovascular approach) and the selection of the length of an angioplasty balloon or a stent.

In both positioning and inter-distance accuracies, the taught and replayed points showed similar results. This confirms, as expected, that the robot can repeat with high accuracy a manually taught trajectory. This is important since the robot can replay at a constant speed the desired scan path for any given patient leg at a high accuracy for 3D reconstruction.

3.7.2.3 Teach/replay repeatability

The robot teach/replay repeatability reported in Table 5 was found slightly higher than the value specified by the manufacturer, which is 0.05 mm. The higher teach/replay repeatability that reached 0.20 mm might be explained by the calibration procedure of the

robot SP. Because the SP was not a fixed component of the robotic system, it became necessary to transform its physical length into the robot referential with Eq. (1). The calibration procedure estimated the SP translation from the robot end-effector. Thereafter all robot point targets were computed with the SP translation estimation to obtain their location in the robot referential. Hence, since SP was involved in all measures of performance, this aspect might explain the difference observed between our study and the manufacturer's specification.

3.7.3 Comparison to other systems

Precision and inter-distance accuracies obtained in this study were better in comparison to other 3D-US freehand systems evaluated with similar methods. The precision of these systems was measured as the standard deviation around a target point, which is similar to Eq.(2), and distance accuracies were evaluated according to known phantom inter-target lengths, measurements with a ruler or other referential systems such as robots. The most popular position localizers in 3D-US systems are optical systems and EM sensors.

Optical systems are known to provide the best level of position tracking accuracy. The optical Polaris system (NDI, Waterloo, Ontario, Canada) provided inter-distance errors as low as 0.193 ± 0.167 mm with a precision of 0.059 ± 0.047 mm for a 1 m distance between the camera and the localized object [164]. However, these results were obtained only for optimal placement of the optical reflectors with respect to the tracking camera. If not, position accuracies as large as 6.67 mm and mean inter-distance accuracies of 3.55 mm ± 1.51 mm were achieved [112]. These last measurements were obtained by using four different optical systems to evaluate the position of a point target on a phantom that was reached with different orientations. In the current study, even though our robot showed an optimum scanning zone and path to reach the best positioning accuracy, and an optimum zone to measure the inter-distance accuracy, the spatial precision was not severely compromised when working in other zones and paths. This would not be the case for optical trackers because the position of the camera would not be optimum to scan, for example, path 1 on the top surface of the phantom and path 3 on its side.

EM position trackers offer the benefit of unrestricted range of motion. However, the accuracy is variable because of their sensitivity to metallic environments and because the transmitter needs to be near the receiver to achieve a good precision. In the literature, there exist discrepancies in the reported precisions and inter-distance accuracies of these devices. Precisions varying between 0.61 mm and 1.7 mm, and inter-distance accuracies varying between 0.05 mm and 1.7 mm, were found for the EM Flock-of-Bird (Ascension Technology, Burlington, Vermont, USA) at distances between the emitter and receiver below 61 cm [85, 93, 160, 161]. When comparing the Fastrack (Polhemus, Colchester, Vermont, USA) with the Flock-of-Bird system, RMS inter-distance accuracies ranging from 0.21 mm to 1.7 mm, and from 0.16 mm to 1.3 mm were measured, respectively with both systems, at a distance of 30 cm [85]. In worst case scenarios, for example in clinical settings with EM interferences, inter-distance accuracies as large as 6.4 ± 2.5 mm (Flock-of-Bird) and 3.2 ± 2.4 mm (Fastrack) were obtained for a 9 cm distance between the emitter and receiver [106]. For lower limb vessel imaging applications, a setting with metallic objects (e.g., US probe, hospital bed) and typical scanning lengths varying between 50 and 100 cm are expected. Consequently, our robot with a precision of 0.57 ± 0.30 mm (see Fig. 3.8) and an inter-distance accuracy of 0.42 ± 0.33 mm (see Table 4) is thus superior to that of approaches using localizing systems since a constant performance can be achieved in all workspaces.

When compared to the few existing robotic 3D-US systems, our design demonstrated its suitability for the proposed clinical application. An articulated mechanical arm for 3D-US imaging had a mean positioning error of 0.7 mm [165] compared to the position accuracy of 0.62 ± 0.29 mm reported in the current study (see Table 3). With the Hippocrate system [140], an absolute positioning accuracy of 0.5 mm and a repeatability of 0.05 mm were obtained, which is also similar to our results (a teach/replay repeatability of 0.10 ± 0.22 mm was found with our system, see Table 5). It is to note, however, that a direct comparison with the Hippocrate scanner is difficult because no precise information was available in [140] on how these measures were obtained. Additionally, in this study, no quantitative evaluation of the 3D-reconstruction of an artery was performed. As a result, not much information supports Hippocrate performance in term of validation in a clinical

mimicking set up. Our 3D-reconstruction showed quantitatively in Table 6 that the robotic system can quantify stenoses with a good accuracy.

3.7.4 Advantages and limitations of our robotic system

3.7.4.1 Performance

In this study, the robot was used as a tracking device to provide positions of 2D-US images for 3D-reconstruction. According to Rousseau (2003), performance of the tracking device includes latency (or lag), update rate, interferences, precision of measures and optimum operating space. To identify how closely a robot follows a taught scan pattern determined by a clinician, it is first important to discuss latency and update rate. Latency is the delay required for the system to detect motion. Update rate refers to the number of positions reported by the system per second. Unfortunately, no measurements of these characteristics were performed or disclosed by the manufacturer of our robotic system. Nevertheless, we did not observe any limitations in scanning mimicking arteries and we can assume that latency and update rate frequencies are faster than the frame rate of US scanners (typically 30 Hz for most applications). Consequently, we do not anticipate any problems for lower limb vessel scanning by a clinician.

Interferences affecting the robot performance can occur when the operating environment is not respected (i.e., temperature, humidity and extreme electrical noise). Accordingly, the environment for the current study encompassed the manufacturer operative conditions required to preserve robust performances (i.e., room temperature and humidity, and normal electrical interferences encountered in industries or hospitals).

For robotic 3D-US imaging, precision of measures and resolution of US images should be comparable. At 10 MHz, US image resolution has approximately, at 3 cm depth, a resolution of 0.3-0.4 mm in axial, 1.0-2.0 mm in lateral and 3.0-4.0 mm in out of plane orientations [166]. In our study, the positioning accuracy of the robot ($\leq$ 0.75 mm) was similar to the combined axial and lateral resolutions of US imaging. However, since the sensing technology of the arm relies on the transformation of joint angles into the end-effector position, the robotic arm will maintain a reliable performance in complex

movements if the robot joints are operated within the safe boundary of their limits. It is to note that bending of the arm is very unlikely because our design is based on a robust industrial robot. However, excessive vibrations may limit the performance.

Other performance limitations include the use of the system under clinical conditions for scanning patients of different anatomy. Currently, our robotic system is limited to accommodate each scan of a patient's leg with a manual taught path made by a clinician. Henceforth, the robot replays this path over the leg and acquires at a constant step US image planes based on a pre-determined trajectory. Of course, movement of the patient's leg between the taught and replay modes would eventually need to be addressed. The patient leg may be either immobilized or an automatic tracking of the vessel and registration during replay may be required. However, these solutions are beyond the scope of the present article.

Finally, the robot performance was evaluated for position and inter-distance accuracies and for teach/replay repeatability at different locations within its operating workspace. A map zone that characterizes the robot performance limitations inside its workspace was achieved (see Figure 3.5 and Tables 3-5). It was found that the robot positioning accuracy limits varied between 0.46 mm and 0.72 mm, the inter-distance accuracy boundaries were between 0.26 mm and 0.63 mm, and the teach/replay repeatability was from 0.04 mm to 0.20 mm. Thus, a clinician can generally expect these performances when operating inside the robot workspace during the scanning of a patient.

3.7.4.2 Design

In this study, we identified the limits of accuracy from the base of the robotic arm that extends to SP for scanning lower limbs. The level of accuracy we can achieve with our robotic system is greatly influenced by the mechanical design specifications of the robotic arm. More specifically, the number of mechanical joints and link dimensions (i.e., member lengths of the robotic arm) are significant elements. Including SP in the evaluation certainly reduced the reported accuracy of our robotic system. It would be possible to improve accuracy with SP by adding mechanical joint limits to the robotic arm to restrain the workspace for optimal operation [119]. An alternate way to improve and preserve

performance would be to change the physical design of the robotic arm by computing a model of optimal link dimensions and joint orientations (i.e., kinematic parameters) with SP. The Jacobian, a matrix that depends on a kinematic model to relate joint velocities to the end-effector, would be a solution to provide a better positioning accuracy measured at the end-effector with SP [158].

Elastic joints are another source that can influence the level of accuracy achievable by a robot. Under this assumption, our robot has intrinsic compliant elements at the joints (e.g., six revolute joints, F/T sensor and cables) that have to be considered. Elasticity of mechanical transmission is often the cause of positional errors at the end-effector when a robot works in contact with the environment [167]. This is often due to static deformations caused under gravity in position tracking and interaction tasks. Given our robotic system was designed to interact with humans, and was in contact with a lower limb mimicking phantom for this study, this aspect is thought to be important to explain the reported positioning accuracies. Nonetheless, when the robot interacts with humans, these effects can be reduced to ensure a high performance with the design of a compliance control in the Cartesian space of the robotic system.

3.7.5 3D-reconstruction of a vascular phantom from a robot scan

3.7.5.1 Calibration with a cross-wire and 3D-US reconstruction

The calibration matrix obtained with the cross-wire showed a precision suitable for a preliminary 3D-reconstruction. However, the calibration precision affected the geometry of the reconstructed vessel in the longitudinal axis. This can be seen in Fig. 3.9, where the 3D reconstructed is slightly shifted in the x-y plane along its length (z axis). It is important to remember that the vascular phantom had a symmetric geometry along its length. For future work, we expect that it may be feasible to improve the calibration precision as the accuracy of the method relies on how well the intersecting point can be detected in the B-scan images and on how the cross-wire location can be precisely estimated in the robot referential. While the precision affected the 3D reconstructed central axis, it did not seem to influence severely the overall geometry. Thus, the stenosis severity could satisfactorily be evaluated from the 3D volume. Nevertheless, a better accuracy than 3.0 % (see Table 6)

may be expected and a z-phantom calibration device may be a solution for this problem [71].

3.7.5.2 Stenosis evaluation

Imaging lower limb stenoses is an important application for 3D-US. This non-invasive imaging technique may become an alternative to 3D reconstruction of arterial segments obtained with magnetic resonance imaging and computed tomography angiography. Carotid artery atherosclerotic plaque progression was evaluated in patients with a 3D-US linear step motor system [89]. Already, the vascular risk factors promoting plaque progression were monitored and analyzed with this system [90]. Another study validated the 3D-US Flock-of-Bird EM system to measure a phantom and blood conduit geometries [102]. Dimensions of uniform and stenotic 3D-reconstructed phantoms were measured. This system was able to detect diameter reductions up to 28 % corresponding to an area reduction of 48 %. More recently, a study with a similar EM system evaluated the error in stenosis quantification for the 3D-US reconstruction of carotid bifurcation phantoms and found errors of -1.2 % for detecting a 70 % stenosis [99]. We found similar results with errors of 3.0 % for detecting a 80% stenosis, and errors of -0.9 % for quantifying a 75 % stenosis (see Table 6).

3.8 Conclusion

The prototype medical robot proved to be a suitable tracking device that offers a constant performance and control to acquire 3D positions with a high precision, and good position and inter-distance accuracies. The computed positions in the robot referential of the acquired US images were satisfactory to quantify stenoses in a 3D reconstructed vessel phantom. Of course, further developments and validations of the robotic system are necessary to provide a platform that would meet clinical needs. Developments include a more robust 3D-US image calibration procedure to improve the accuracy of the 3D reconstruction from B-mode, color and power Doppler images. The integration of electrocardiogram data in the robot control system to gate the US image acquisition would also eliminate deformations of the reconstructed volume due to the pulsation of the vessel

wall. Acquisition of US images with controlled applied pressure may also be of interest to enable non-invasive elastographic measurements of pathological biological tissues [168] or to detect deep venous thrombosis with objective vessel compression measures [169].

Acknowledgments

This work was supported in part by the Canadian Institutes of Health Research (CIHR) under grant MOP #53244. Drs Soulez and Cloutier are, respectively, recipient of a Clinical Research Scholarship Award and of a National Scientist Award of the Fonds de la Recherche en Santé du Québec. Ms Janvier is recipient of Studentship Awards of the Fonds de la Recherche sur la Nature et les Technologies du Québec and of the Quebec Black Medical Association, whereas the salary of Ms Roy Cardinal is partially supported through a Studentship Award of the Natural Sciences and Engineering Research Council of Canada. The authors are grateful to Dr Louise Allard for manuscript revisions, and to Mr Benoit Godbout of the University of Montreal Hospital and Dr Daniel Leotta of the University of Washington for helpful discussions.

Chapter 4

Validation of 3D reconstructions of a mimicked femoral artery with an ultrasound imaging robotic system

Divide each difficulty into as many parts as is feasible and necessary to resolve it.

Rene Descartes

4.1 Forward

This chapter presents the paper published in the journal *Medical Physics* by the authors Marie-Ange Janvier, Gilles Soulez, Louise Allard and Guy Cloutier[29].

This paper describes the methods developed to characterize the calibration transform that relates the US image plane of the robotic system. A Z-phantom calibration procedure was employed and different clinical image acquisition settings were investigated. The accuracy of the calibration transform was evaluated with a vascular phantom, where a lower limb mimicking artery was reconstructed in 3D.

4.2 Abstract

Purpose: The degree of stenosis is the most important criterion to assess peripheral arterial disease manifested by atherosclerosis mainly in lower limb arteries. Ultrasound (US) imaging offers low-cost, safe, and convenient options to evaluate this disease, but most US freehand approaches cannot optimally locate stenoses and map lower limb arterial

geometries. A 3D-US imaging robotic system that can control and standardize image acquisition by scanning typically-encountered diseased arterial lower limb segments is presented and validated with phantoms.

Methods: A Z-phantom calibration procedure was used to characterize spatial transformation of the US probe image plane for different clinical image acquisition settings. Moreover, the accuracy of the calibration transform to reconstruct a lower limb mimicking vessel geometry was evaluated with a vascular phantom.

Results: A 3D calibration precision of 0.47 ± 0.27 mm was achieved. Reconstruction errors were less than 1.74 ± 0.08 mm in all 3D vessel representations, and the cross-sectional areas of each image section were close to those of gold standard phantom measures. The best reconstruction accuracy (smallest error) was 0.40 ± 0.03 mm.

Conclusion: Altogether, these results demonstrate the potential of the robotic scanner to adequately represent lower limb vessels for the clinical evaluation of stenoses.

4.3 Introduction

Atherosclerosis is the principal cause of peripheral arterial disease that leads to the progressive narrowing of lower limb arteries [7, 45, 46]. The 3D location of lesions and the degree of stenosis are the most common criteria for assessing the severity of PAD. Moreover, a map of the entire lower limb vessel is required to prepare an appropriate intervention (e.g., the diameter and length of an angioplasty balloon and stent) [170, 171]. In fact, most medical centers perform digital subtraction angiography, computed tomography angiography or magnetic resonance angiography for the complete representation of lower limb arteries [26, 38]. Although these technologies yield good to excellent image resolution and even some 3D rendering, they are either too costly, invasive or ionizing.

---

[29] The co-authors Gilles Soulez and Guy Cloutier are the supervisors of the thesis. The co-author Louise Allard helped in organizing and editing the manuscript.

Different ultrasound (US) imaging techniques, namely pulsed-wave Doppler, color Doppler flow imaging, power Doppler angiography and B-mode imaging, are currently able to detect arterial lesions in lower limbs safely, non-invasively and at low-cost [51, 151, 152, 172]. However, it is not easy, with these modalities, to visualize the entire lower limb vascular tree with accuracy within an acceptable time frame. Moreover, the evaluation of atherosclerotic disease with conventional 2D B-mode US is highly operator-dependent [32].

3D-US imaging can precisely define the degree of stenosis and map its location along the lower limb vascular tree. Already, many 3D-US systems have been successfully developed and validated in various clinical applications, notably, obstetrics, cardiology, and vascular imaging, to increase diagnostic confidence [68]. Most of them rely on a freehand US probe-tracking method that produces uneven geometric sampling, adding uncertainty to the reconstruction. Moreover, popular freehand tracking devices (optic and electromagnetic) have operating restrictions: scanning of small distances, the necessity of a constant line of sight, and avoiding metallic interference [71, 85, 106, 155, 173].

Robotic systems represent a promising alternative for lower limb stenosis quantification and location [119] because they can simultaneously control and standardize 3D-US acquisition without the limitations of 3D freehand devices. Some medical 3D-US prototype robots have been developed but are exclusively deployed in research [123, 140, 174, 175] because they focus mainly on architectural control and safety designs so that their potential clinical performance has not been evaluated. We proposed a medical robot [148] for 3D-US scanning of lower limb vessels. The principal features of this system are its teaching mode that enables the learning of “freehand” scanning accommodated to patients’ legs, and its replay mode that reproduces the manually-taught path. Clinicians would acquire with this system 2D cross-sectional US images at a controlled speed with x, y and z registration of coordinates and constant contact pressure for 3D reconstruction. Based on our previous report with this system [148], a high positioning accuracy of the robot end-effector and repeatability were achieved. In the context of the current study, these first-step results were required to assure robustness of this technology to track the US probe position into the robot 3D referential.

A major challenge in either freehand or robotic 3D-US is the precise localization of

the image into the referential positioning system (i.e., calibration transform for rotation, translation and scaling) [71, 176]. This information is particularly important as errors in image transform propagate through subsequent stages of 3D reconstruction in image analysis and scaling [177]. These errors thus have a major impact on the quality of the reconstructed geometry that enables precise 3D visualization, planning, and accurate image-guided interventions. 3D-US calibration techniques usually require imaging a phantom of known geometry and physical properties with key features that are easily identifiable. The simplest and most common phantom is the point-target (i.e., crossed wires or spherical ball) except that calibration is very tedious, time-consuming, and susceptible to image artifacts produced by the US beam [160, 161, 178]. A calibration wall phantom allows the fastest registration of US images [78, 176, 179] but for calibration to be valid, it needs to be scanned at a proper range with a specific protocol. Moreover, reverberations of the US beam by the wall can also affect calibration quality. The Z-phantom is the most efficient method for fast and precise calibration from a single B-scan [178-181]. In comparison to other calibration methods, it provides the best performance in terms of 3D point reconstruction accuracy [178]. To the best of our knowledge, no 3D-US studies have validated the effect of calibration transforms on 3D reconstructed vascular models. The objectives of this study were to adapt a Z calibration procedure for the 3D-US imaging robot and to evaluate its performance in terms of precision and reconstruction accuracy on a 3D vascular geometry with double stenoses.

4.4 Materials and methods

4.4.1 Prototype medical robotic 3D-US imaging system

The robotic system illustrated in Fig. 4.1 includes a computer workstation, the robotic arm (F3 articulated robot, CRS Robotics Corporation, Burlington, Ontario, Canada) and an US echograph. This 3D acquisition scanner, described in detail elsewhere [148], can capture US images at uniform spacing during probe displacement. In the current study, a Vivid-5 echograph system (General Electric, Milwaukee, WI, USA) equipped with a FPA 10-MHz linear array probe was employed. US images were digitized in 480 x 640 pixel format.

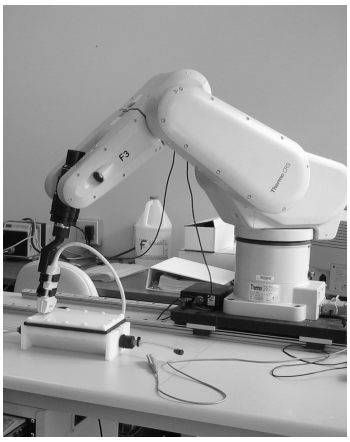

Figure 4.1: Overview of the prototype medical robotic 3D-US imaging system [148]. The robotic arm is moved by a user interface software on the workstation. 2D-US images are tagged with US probe positions acquired from the robotic arm. In this example, a vascular phantom is scanned.

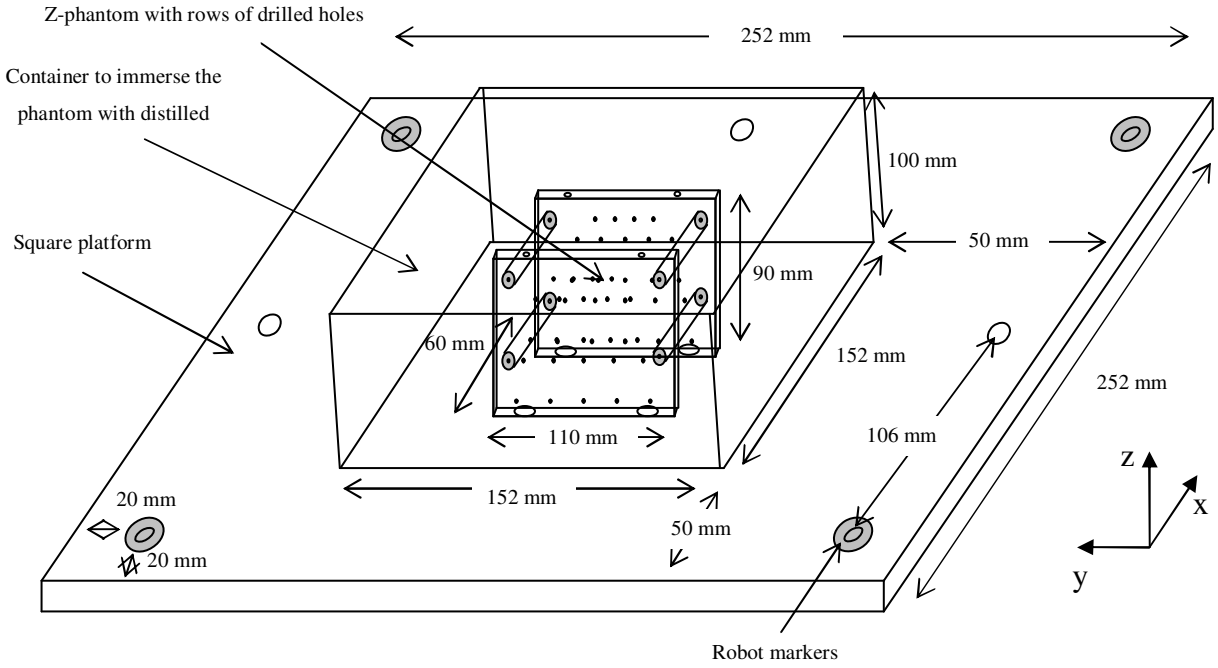

Figure 4.2: A complete view of the calibration phantom. It consists of a square platform, a container and a Z-phantom.

4.4.2 Calibration procedure

4.4.2.1 Calibration phantom, experimental set-up, data acquisition and processing

A precise calibration procedure based on a Z-phantom was developed for the 3D-US robotic system (i.e., to identify features that best relate the US image plane location to the phantom space within the robot referential). The design (Fig. 4.2) consists of a base platform, a container, and the Z-phantom.

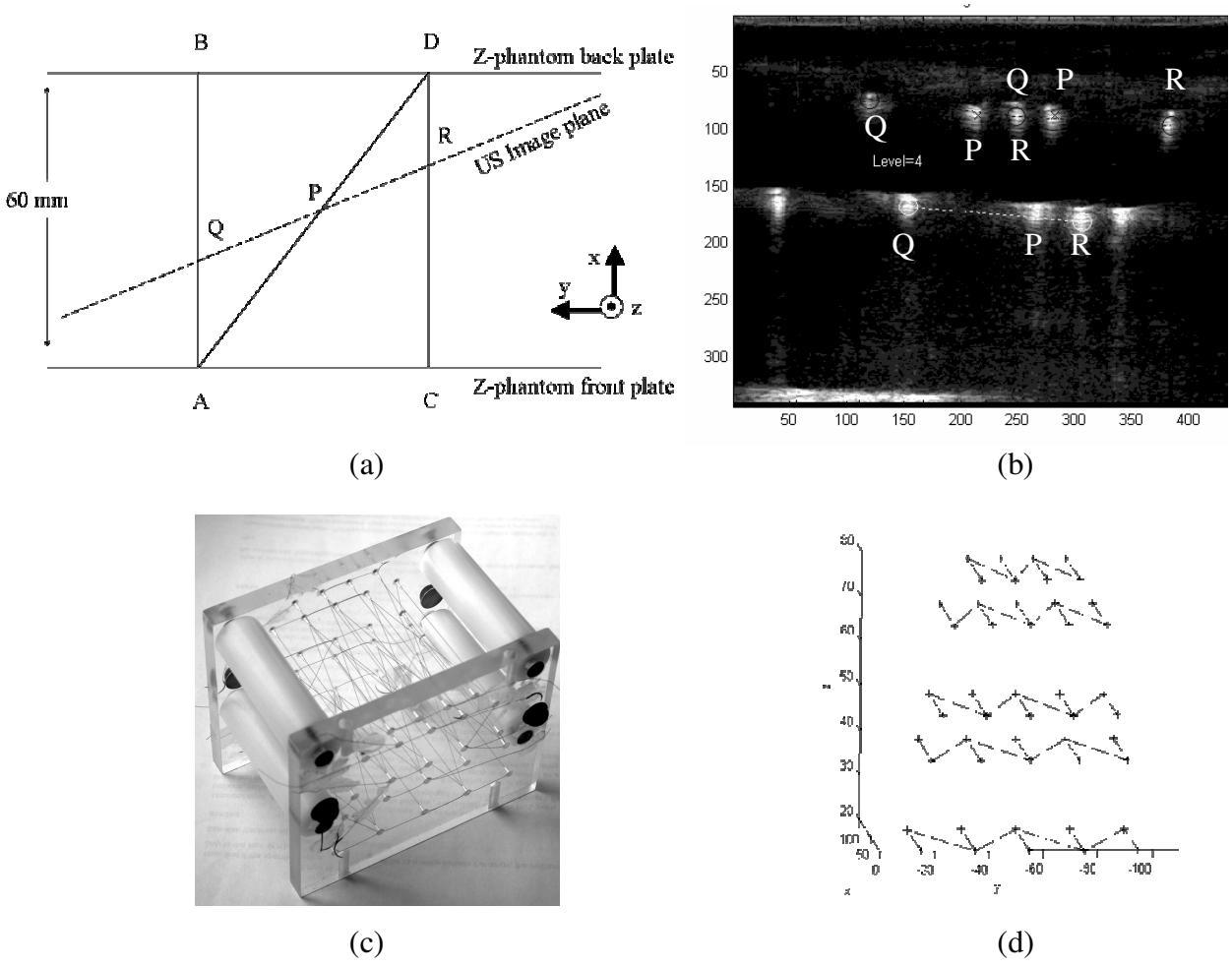

Figure 4.3: (a) Top view of the Z-phantom that illustrates a single Z-fiducial (i.e., segment wires $\overline{BA}$, $\overline{AD}$ and $\overline{DC}$). An US plane (i.e. dashed line) intersects these wires in collinear points *Q*, *P*, and *R*. (b) Example of an US image that contains multiple points of Z-fiducials in its field of view. (c) Side view of the complete Z-phantom is shown with (d), a grid of the entire 19 Z-fiducials constructed.

The square platform incorporates 4 holes to fix the phantom to a table in the robot workspace. This platform also contains 4 hemispherical steel holes, each 8.38 mm in

diameter and 4.19 mm in depth, which serve as markers to localize the phantom in the robot referential. The Z-phantom, inspired by previous works [178-181], was immersed in distilled water at room temperature within the container. It consists of 2 parallel Plexiglas plates (110 mm wide × 90 mm high × 9.53 mm thick) positioned 60 mm apart and maintained by 4 spacers made of high density polyethylene. Each plate encloses 24 drilled holes of 0.46 mm diameter aligned in 5 different rows with 10-20 mm gaps. A surgical blue monofilament polypropylene suture wire of 0.07-0.099 mm diameter (8726 Prolene 6-0, Ethicon Inc., Piscataway, NJ, USA) was interwoven through the holes to construct 19 Z-shaped patterns (i.e., Z-fiducials), as depicted in Fig. 4.3.

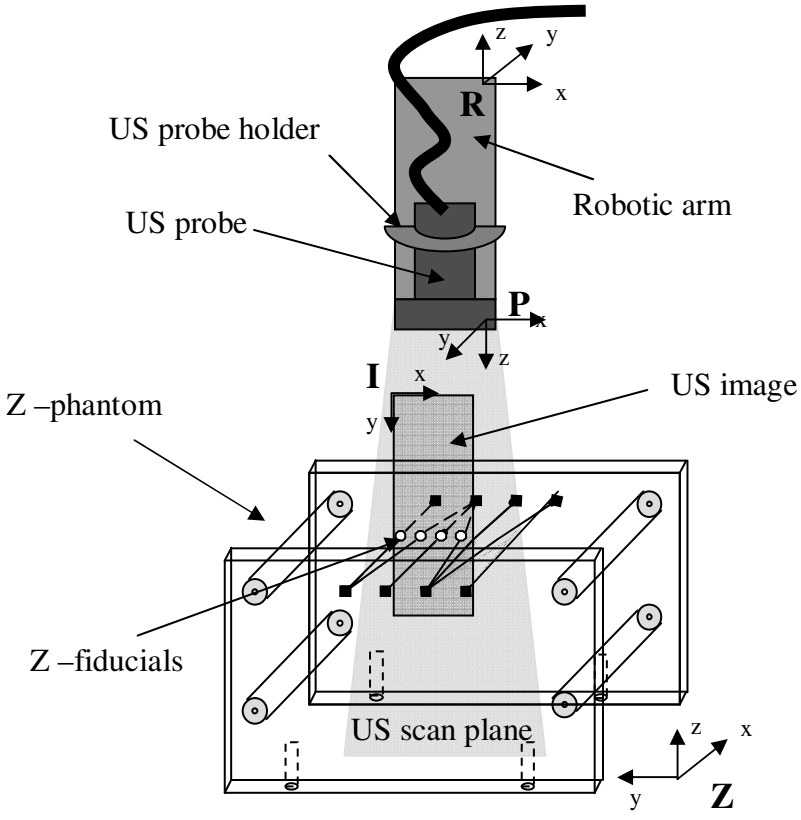

Figure 4.4: The coordinate system involved in the calibration method: Z-phantom *Z*, US image *I*, US probe *P* and robot *R*. The calibration transform was determined from a series of coordinate frame transformations that relate *Z* features to *I* and *R*.

The US probe was fixed with a holder to the robotic arm. The probe was held perpendicular over the Z-phantom to facilitate the US scan plane intersection with Z-fiducials (Fig. 4.4), and to minimize the blurry effect that the finite thickness of the US

beam has on images. Then, transducer motions were taught to the robotic arm to locate the Z-fiducial markers while acquiring US images.

Because peripheral arteries in lower limbs have a 3- to 8-cm depth range [182], operator-dependent adjustments of US image settings are required for a given scan. Consequently, such settings were evaluated because of the impact on calibration transforms [71, 183]. The US image acquisition parameters included 4 depths (5, 6, 7 and 8 cm) at no zooming, with a fixed focus depth of 4-5 cm, and 3 focus beam depths (2-4 cm, 4-5 cm and 5-7 cm) at a fixed 7-cm depth with no zooming. The focus beam depth provides the best lateral resolution of the US transducer to distinguish small adjacent structures perpendicular to the beam's major axis. At the 7-cm depth, with the best focus beam depth that had previously been found, 3 amplifications (i.e. zooms), corresponding to window sizes of 2, 3 and 4 cm, were also used. The zoom setting of the US scanner allows the display of only a selected region of interest remote from the transducer, where a smaller window size represents a higher magnified ROI. For each setting, 10 US scans were acquired, and, for each scan, 10 frames were selected to compute 10 calibration transforms. The ROI was cropped, and visible *Z*-fiducials identified and segmented manually.

4.4.2.2 Calibration equations

Different coordinate systems are involved in the calibration procedure and each one is related to the others by Eq. (11) (Fig. 4.4). Every transformation matrix T contains 3 rotations (α, β, γ) and 3 translations (x, y, z). The standard notation throughout this manuscript is ${}^{A}T_{B}$, where the coordinate system B is defined into the referential A.

$$\begin{pmatrix} x_k \\ y_k \\ z_k \\ 1 \end{pmatrix} = {}^{Z}T_{R} \cdot {}^{R}T_{P} \cdot {}^{P}T_{I} \cdot \begin{pmatrix} s_x \cdot u_k \\ s_y \cdot v_k \\ 0 \\ 1 \end{pmatrix} \qquad (11),$$

In the above equation, ${}^{Z}T_{R}$ is the unknown transformation of robot referential R into the Z-phantom, ${}^{R}T_{P}$ represents the known transformation of US probe P into robot referential R for an acquired image, and ${}^{P}T_{I}$ is the unknown calibration transformation of image I in US probe P. For each image, k, u_k and v_k are column and row indices with respect to the B-

scan origin; s_x and s_y are scaling parameters in mm/pixel, estimated from B-scan depth and zoom settings. Thus, a point in the k_{th} US image is localized in the Z-phantom referential with x_k, y_k and z_k.

4.4.2.2a Identification of Z-fiducials

US images depicted multiple dots that could be used to identify Z-fiducials (see Fig. 4.3). Each feature point in an US image *I* were identified in the *Z* referential by trigonometry, an approach similar to that in [178]. In particular, when the US image plane intersects the Z-shape phantom wires, it forms multiple collinear points similar to $\overline{QPR}$ (see Fig. 4.3) in the US image. Usually, these crossings are unknown in the *Z* referential. However, while not visible in the US image, the *A*, *B*, *C*, *D* location points are known in the *Z* referential due to the manufacture of Z-fiducials (Fig. 4.3). Thus, with similar triangles Δ, it was possible to calculate the location of the homologous point *P* that expresses the location of image plane *I* in the *Z*-phantom. The following equations are derived from the similar Δ*APQ* and Δ*DPR* that define point *P*.

$$x_P = x_A + h \cdot (x_D - x_A) \qquad (12)$$

$$y_P = y_A + h \cdot (y_D - y_A) \qquad (13)$$

$$z_P = z_A + h \cdot (z_D - z_A) \qquad (14),$$

where *h* is the ratio of distance $\overline{AP}$ to distance $\overline{AD}$ that is equivalent to the ratio of distance $\overline{QP}$ to distance $\overline{QR}$. By identifying the location of point *P* inside the US image plane *I* (Fig. 4.3), this corresponds to the detection of the same feature location point in the *Z*-phantom referential (i.e., x_k, y_k and z_k in Eq. (11)). In practice, several Z-fiducials were localized within a given US image plane to determine the relative position and orientation of the scan.

4.4.2.2b Localization of the Z-phantom

A calibration procedure with a spherical pointer that fits tightly into the robot markers of Fig. 4.2 was first used to localize the Z-phantom in the robot referential *R*. A

complete description of the method appears in [148]. For each robot marker, 10 independent sets of points corresponding to different articulations of the robotic arm were taught, then replayed and recorded by the robotic system. An iterative closest point (ICP) algorithm with Delaunay tessellation was employed to fit the measured robot points to the real Z-phantom robot marker point coordinates (MatLab open source code ICP, version 1.4, by Per Bergström, March 7, 2007). Thus, rigid body transformation ${}^{z}T_{R}$ between the Z-phantom model and the robot marker points could be determined with this method.

4.4.2.2c Calibration algorithm

A calibration algorithm served to determine the calibration transform that defines the spatial relationship between US image *I* and US probe *P*. Eq. (11) presents an over-determined system of non-linear homogeneous equations where most of the Z-phantom parameters can be estimated. The remaining unknown parameters, i.e., the calibration transform of image *I* into US probe *P* (${}^{P}T_{I}$), were computed by the Levenberg-Marquardt iterative algorithm, with a detailed description provided in [71, 78].

4.4.2.3 Calibration performance evaluation with the Z-phantom

The precision of the calibration procedure was evaluated by measuring variations in the *x*-*y* position of the US image plane due to spatial calibration errors [177]. It is not a measure of accuracy of the calibration parameters but of their repeatability. Ten different US images of the Z-phantom were assessed: 6 fiducial markers in each image were identified and reconstructed into the phantom referential with the calibration transform of Eq. (11). The precision of calibration C_{rms} was computed by:

$$C_{rms} = \frac{1}{\sqrt{MN}} \sum_{i=0}^{M} \sum_{j=0}^{N} \sqrt{(x-\bar{x})^2_{i,j} + (y-\bar{y})^2_{i,j}} \qquad (15),$$

where $(x-\bar{x})_{i,j}$ is the variation from the mean location $\bar{x}$ for fiducial positions *i* in the *x* direction for image *j* (see Fig. 3.4 for the identification of the image coordinate system I(*x*,*y*)). This definition applies as well to direction *y*. For every US image setting (i.e., depth, focus beam depth and zooming), 10 calibrations (i.e., 10 measures of C_{rms}) were performed

to obtain the mean precision that was calculated with $M = 6$ fiducial markers and $N = 10$ US images. The total sample size thus corresponded to the identification of 600 points on the Z-phantom. Note that this is the same equation as Eq. (8) in [148] but with a different notation.

4.4.3 3D reconstruction performance evaluation on a lower limb-mimicking artery

4.4.3.1 Vascular phantom geometry and experimental set-up

A phantom, mimicking a lower limb femoral artery, was fabricated to evaluate the 3D reconstruction performance of the robotic scanner. It contained 2 axisymmetrical stenoses of 80.0% *(S1)* and 75.0% *(S2)* in area reductions with a 'disease-free' diameter of 7.87 ± 0.11 mm (i.e., gold standard dimension). The vessel central axis was positioned at 3.4 cm from the top of the phantom. The entire fabrication process, characteristics and geometric accuracy of the vessel lumen embedded in this phantom are available in [163]. The mathematical model describing the vessel lumen geometry can be found in [186]. This geometry served as the gold standard reference for all subsequent measures that follows.

The vascular phantom was fixed tightly into the robot workplace and scanned along its length. A quasi-parallel plane US scan path was taught and replayed by the robot, and B-mode images were acquired at the same settings as those used for precision assessment with the Z-phantom (i.e., 4 depths, 3 focus beam depths and 3 zooms). For each US image setting, 10 scans were captured to reconstruct 10 vessels in 3D.

4.4.3.2 3D-US reconstruction process

At first, the vessel lumen of every US scan was segmented with a fast-marching method based on gray level statistics and gradients adapted from [41]. Each pixel of the segmented lumen contour was then mapped into the robot referential with the best calibration transform computed and the corresponding probe positions. The transformed lumen contours were re-sampled on a 300 x 20 rectangular grid and interpolated to provide

a 3D surface rendering of the reconstructed vessel. After that, the reconstructed polygon models were transformed to generate contours normal to the vessel center axis, as in [184].

4.4.3.3 3D reconstruction performance evaluation

The accuracy of 3D reconstructions was assessed by determining lumen surface map and vessel area errors from cross-sectional planes along the 3D-reconstructed vessel. Reconstructed and gold standard model-matching were performed by finding the center of gravity of both 3D vessel lumens, and by computing the appropriate transformation matrix (translation and rotation) that minimized the difference between both referential systems. Lumen surface map error was evaluated by measuring the absolute distance between the reconstructed geometry and that of the gold standard vessel, as expressed by:

$$E_{i,j,k} = abs\big(M(i,j,k) - S(i,j,k)\big) \qquad (16).$$

where M is the surface map of the reconstructed vessel, S the surface map of the gold standard vessel, $1 \leq i \leq X$ for X the number of grid points along the x axis depicted in Fig. 4.5, $1 \leq j \leq Y$ for Y the number of grid points along the y axis, and $1 \leq k \leq Z$ for Z the number of grid points along the z axis.

For each reconstruction, the error in area was also evaluated with a polygon-specific function of Matlab, *Polyarea,* which computes the average number of pixels inside a closed contour. Thus, for each US image setting where 10 reconstructions were performed, these measures (surface map and area errors) were tabulated independently into 1 mean (sample sizes = $X \times Y \times Z$ for the surface map accuracy and X for the area accuracy, where X also corresponds to the number of cross sections).

4.4.4 Statistical analysis

Analysis of variance with multiple pair-wise comparisons by the Bonferroni method was performed on the calibration and 3D-reconstruction results to evaluate differences among US imaging settings. All statistical analyses were done with the SPSS statistical software (version 13.0, SPSS Inc., Chicago, IL, USA).

4.5 Results

4.5.1 Calibration performance evaluation with the Z-phantom

Table 7 presents calibration precisions C_{rms} achieved with the robotic scanner. At 4 different image depth settings (i.e., from 5 to 8 cm), fixed focus depth of 4-5 cm, and no zooming, precision improved as the US image depth was increased (C_{rms} varied from 1.19 to 0.58 mm); 5 and 6 cm had significantly lower precision than other depths ($p < 0.001$). At the fixed image depth of 7 cm and no zooming, C_{rms} varied from 0.67 to 0.78 mm as a function of focus beam depth, 5-7 cm being the poorest ($p < 0.001$), and 4-5 cm, the best ($p < 0.05$). Note that a smaller sample size served to determine calibration performance at the 2-4 cm focus beam depth because not enough Z-fiducials were visible to localize the US plane on some scans. At the same 7-cm fixed depth and the best focus beam depth of 4-5 cm, optimum mean precision was achieved at maximum zooming (2:7) ($p < 0.001$) and degraded with less magnification (precision varied between 0.47 and 1.10 mm).

Table 7: Calibration precision

US image parameters	Settings	C_{rms} (mm)	Sample size (N)
Image depth at fixed 4-5 cm focus beam depth and no zoom	5 cm	$1.19 \pm 0.91^{\delta}$	600
	6 cm	$0.93 \pm 0.47^{\delta}$	600
	7 cm	0.60 ± 0.38	600
	8 cm	0.58 ± 0.36	600
Focus beam depth at fixed 7-cm image depth and no zoom	2-4 cm	0.72 ± 0.41	540
	4-5 cm	$0.67 \pm 0.32^{£}$	600
	5-7 cm	$0.78 \pm 0.37^{\delta}$	600
Zoom at fixed 7-cm image depth and 4-5 cm focus beam depth	2:7	$0.47 \pm 0.27^{\delta}$	600
	3:7	0.75 ± 0.41	600
	4:7	1.10 ± 0.60	600

C_{rms} is the reconstruction precision of the medical robotic system evaluated with Eq. 5 for different US image settings. N is the total number of sample points used. $^{\delta}$ indicates a statistically significant difference on pair-wise comparisons between settings on a US image parameter with $p < 0.001$ and $^{£}$ signifies $p < 0.05$.

Table 8: Reconstruction accuracy

US image parameters	Settings	Reconstruction error (mm)	Sample size (N)
Image depth at fixed 4-5 cm focus beam depth and no zoom	5 cm	0.87 ± 0.08	7
	6 cm	1.20 ± 0.02	10
	7 cm	1.74 ± 0.08	10
	8 cm	1.45 ± 0.12	10
Focus beam depth at fixed 7-cm image depth and no zoom	2-4 cm	1.71 ± 0.03	10
	4-5 cm	1.11 ± 0.003	10
Zoom at fixed 7 cm image depth and 4-5 cm focus beam depth	2:7	0.93 ± 0.04	9
	3:7	0.40 ± 0.03	10
	4:7	0.46 ± 0.03	10

Reconstruction accuracy of the medical robotic system evaluated in terms of distance errors for different US image parameters. Each value represents the mean ± standard deviation computed over 1 reconstruction from *N* total number of models used. Each pair of multiple comparisons between settings of US image parameters was significantly different ($p < 0.05$).

4.5.2 3D reconstruction performance evaluated on a lower limb-mimicking artery

Fig. 4.5 presents examples of the worst (Panel a) and best (Panel b) 3D reconstructions at different views with labeled stenoses. In Fig. 4.5a, vessel shape showed large distortions, whereas in Fig. 4.5b, overall geometry appeared to be acceptable. Corresponding lumen surface map errors are reported in Fig. 4.6. Note that similar distance errors were found for the 9 other reconstructed lower limb-mimicking vessels at the specified US image settings. Table 8 summarizes the accuracy of all 3D reconstructions. The best reconstructions were obtained at the 3:7 zoom setting, for an image depth of 7 cm and a focus beam depth of 4-5 cm (0.40 ± 0.03 mm, Fig. 4.6b) ($p < 0.05$). No vessel reconstructions were computed at the 5-7 cm focus beam depth because we assumed that worse results would be obtained (because the focal depth was the farthest with respect to the vessel central axis depth of 3.4 cm).

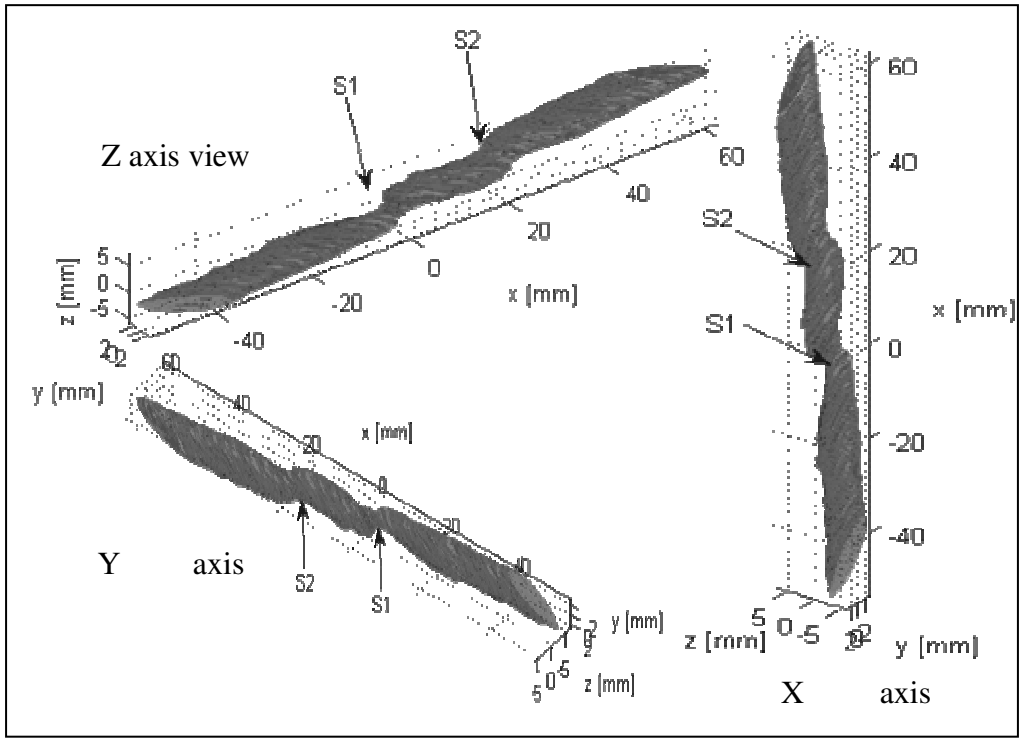

(a)

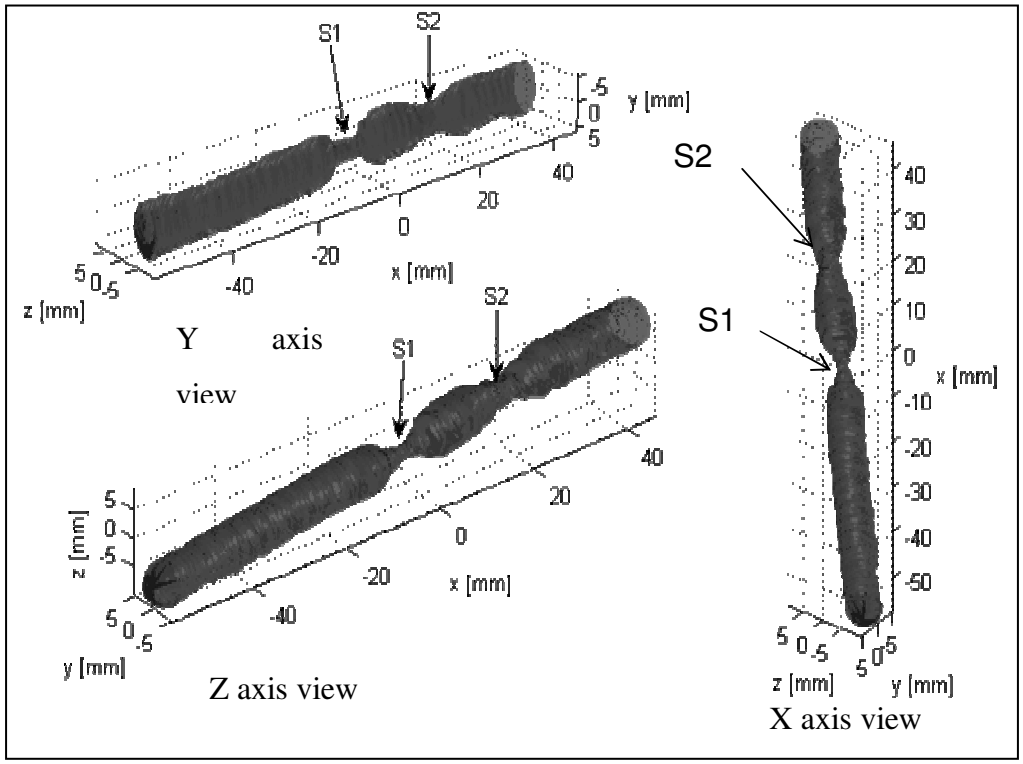

(b)

Figure 4.5: Examples of 3D-reconstructed vascular geometries with axisymmetric double stenoses (S1 and S2). (a) The worst 3D vessel reconstruction is displayed at 7-cm image depth and 4-5-cm focus beam depth with no zooming. (b) The best 3D reconstruction is obtained at 7-cm image depth, 4-5 cm focus beam depth and 3:7 zoom setting.

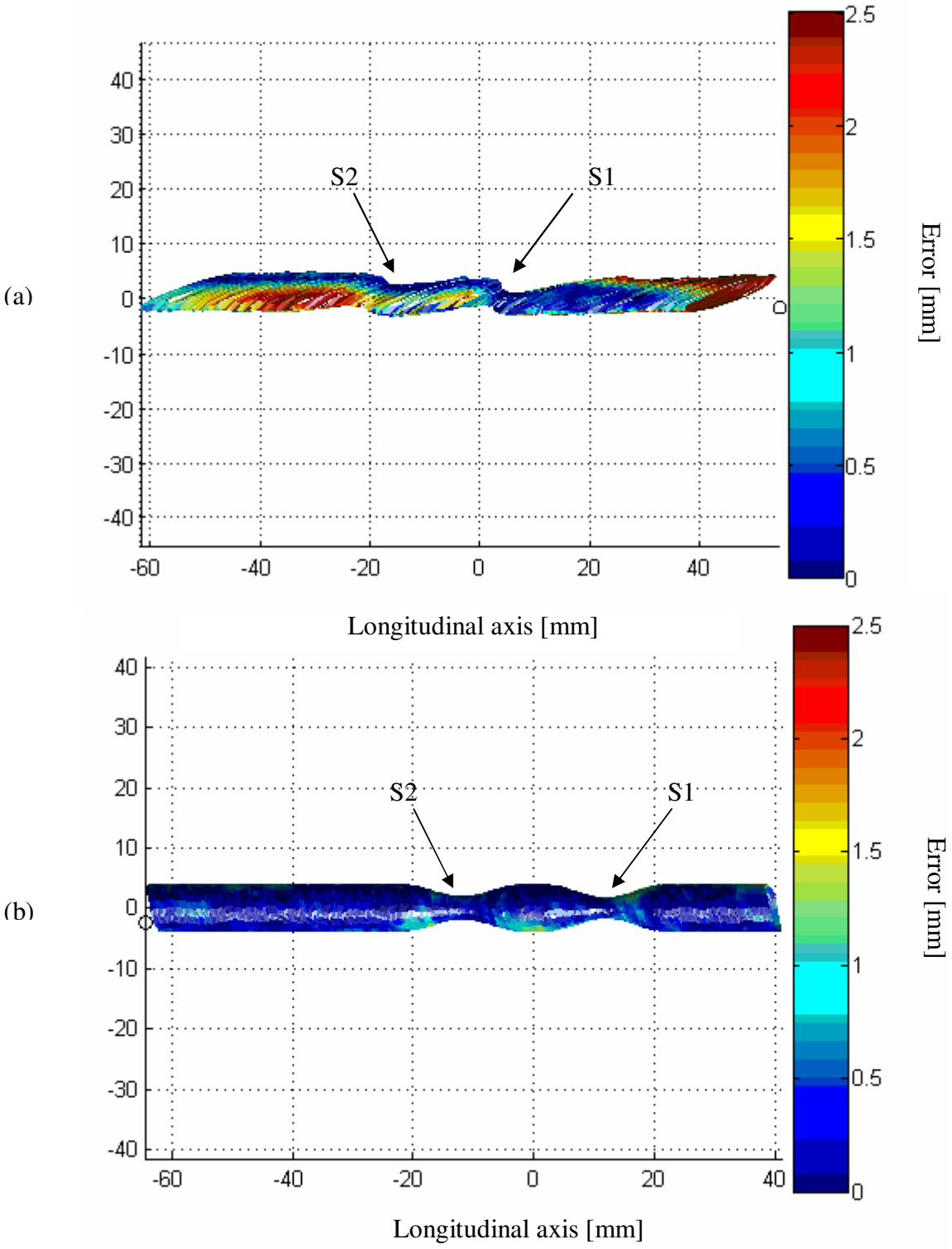

Figure 4.6: Reconstruction errors with respect to the axisymmetric cylindrical gold standard model. (a) Error map of the worst reconstruction corresponding to Panel a of Figure 4.5. (b) Error map of the best reconstruction corresponding to Panel b of Figure 4.5. Note that the same projected view is used on both Panels, differences are associated with reconstruction errors.

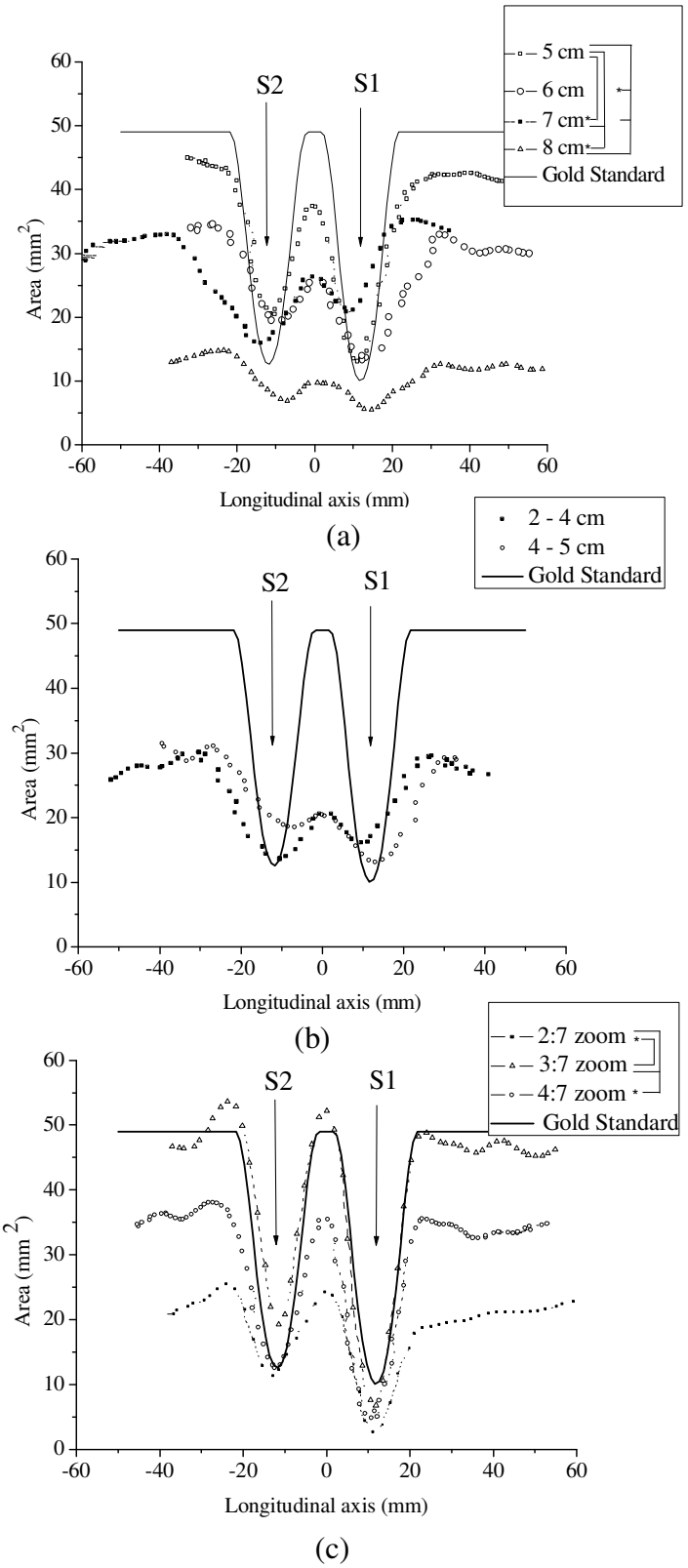

Figure 4.7: Mean areas of 3D-reconstructed vascular geometries with respect to gold standard dimension at different US image settings (for each curve, standard deviations between reconstructions are not displayed to facilitate reading): (a) at 4 image depths, 4-5 cm fixed focus beam depth and no zooming, (b) at a fixed image depth of 7 cm, no zooming and 2 focus beam depths, and (c) at 7-cm fixed image depth, 4-5 cm fixed focus beam depth and 3 zoom settings. For each panel, * indicates a statistically significant difference between US settings on pair-wise comparisons with $p < 0.05$.

Fig. 4.7 shows the reconstructed vessel areas at all tested US image parameters (legends indicate comparisons with significant differences, * $p < 0.05$). In general, an underestimation of cross-sectional areas was noted, except for the best setting in Panel c (3:7 zoom) where the vessel geometry was adequately reconstructed. In 6-, 7- and 8-cm image depth settings, at a fixed focus beam depth and no zooming, significantly underestimated areas were found ($p < 0.05$) (Fig. 4.7a), whereas in focus beam depth settings at a fixed image depth and no zooming, the areas revealed no statistical difference ($p = 0.11$) (Fig. 4.7b). In zoom settings, at fixed depth and focus beam depth, differences were generally in the most underestimated areas: 2:7 and 4:7 ($p < 0.05$).

4.6 Discussion

4.6.1 Calibration performance evaluation

In this study, for all image settings, the mean C_{rms} calibration precision ranged from 0.47 to 1.2 mm (Table 7). This indicates that the calibration transform is variable from one US image setting to another and that parameters can be adjusted on US scanning equipment to improve C_{rms}. However, some scanner parameters that may affect C_{rms} could not be improved or modified, such as the axial, lateral and elevational resolutions that respectively depend on the wavelength propagating in the medium (US frequency), on beam focusing and transducer lenses shape. Such parameters were not specifically considered in our study but their impact on C_{rms} can be approximated, according to a study realized using a similar scanner with a linear array probe of 10 MHz [166]. In that study, reported US image resolution was 0.3-0.4 mm in axial, 1.0-2.0 mm in lateral and 3.0-4.0 mm in elevational at a 3.0 cm depth. It is clear that the use of an US scanner with better resolutions would have positively impact our results, especially lateral and elevational resolutions. Nevertheless, these are typical parameters of modern US scanners.

As also noted, each adjusted parameter (image depth, focus beam depth and zooming) individually impacted the precision of the 3D robotic US scanning system. For the image depth setting with no zooming at a fixed 4-5 cm focus beam depth, C_{rms} was

minimum at either 7 or 8 cm with a mean value close to 0.60 mm (no statistical differences were noted between both measures). This result was not anticipated since C_{rms} performance was expected to become poorer as US image depth increased [160, 185, 186] because pixel density (i.e., axial and lateral) decreased.

In addition to the US scanner parameter selection, variations in the calibration transform were found dependent on points chosen in the B-scan. A greater number of points from the Z-phantom provided a more defined plane that could result in better calibration precision. Thus, at the smallest depth settings, lower precisions can be attributed to the limited field of view of the Z-phantom in US images, giving less Z-fiducials available for establishing the calibration transform of Eq. (11). Other studies with Z-phantoms have also found improved calibration precision at deeper US image settings for the same reason [178-181]. In the case of the focus beam depth and referring to Figs 4.2 and 4.3, the best C_{rms} performance was achieved at the 4-5 cm setting (0.67 ± 0.32 mm), which corresponds to the mid depth of the Z-phantom with a dimension of 9 cm. Accordingly at this setting, more Z-fiducials with optimum resolution could be imaged, thus improving the calibration transform. As also seen in Table 7, the zoom amplification ratio of 2:7 provided the best precision, with C_{rms} = 0.47 ± 0.27 mm. Image quality and definition were maximized with zooming and enhanced the calibration precision. However, for the calibration transform to be estimated adequately with zooming, care had to be taken to note the (x, y) position of the zoomed ROI within the whole US scan plane.

We also noted in this study that it was difficult to align the scan plane with the Z-fiducials because the finite US beam thickness (elevational resolution) caused point targets to appear in the B-scan even if they were not exactly in the mid position of this scan dimension [179]. Thus, dots that resulted from the intersection of Z-fiducials with the scanning beam appeared as smeared ellipses. This US beam offset could render the segmentation of Z-fiducials challenging in B-scans, and affect C_{rms}. In summary, the most repeatable calibration transform should be identified before scanning a vessel, and this requires testing different US image settings. Nevertheless, the results do not guarantee

accurate reconstruction of a lower limb artery because this measure only represents the consistency of the calibration parameters and not their accuracy.

4.6.1.1 Comparison with the literature

Calibration precision provides a measure that allows a fair evaluation of 3D-US system advantages and limitations. Previous Z-phantom studies with 3D-US freehand systems have reported similar findings as our 0.60-mm RMS (Root Mean Square) (600 measures) calibration precision at 7 cm US image depth, no zooming, with a 10-MHz linear array [178-181]. Precisions of 1.0-4.5 mm and 1.0-2.0 mm RMS (20 image samples each) have been obtained for the electromagnetic sensor system at respectively 9 and 16 cm US image depths with a 3.5-MHz sector-phased array [179]. For the optical tracking system, precisions of 0.7 mm and 1.2 mm (10 image samples each) have been presented for US image depths of 8 and 15 cm, respectively, using a 3.75-MHz curvilinear probe [180]. Still, other similar studies with a 7.5-MHz curvilinear probe have found this measure to deteriorate to 1.6-2.7 mm (36 measures) between 6-12 cm US image depths [187], or, alternatively, to improve to 1.04 ± 0.84 mm (1,830 measures) with a 10-MHz linear probe array [178]. While our results seem to perform better than these previous studies (especially when zooming is considered), comparison between other reports should be undertaken with caution because differences do exist in the US echograph, probe frequency, image settings, 3D tracking device, and performance evaluation method utilized. In comparing precision for different 3D-US calibration methods [71], smaller values were obtained when it was computed as the residue of the non-linear minimization problem of Eq. (11) [78, 183], or, alternatively, when it was assessed as an average measure [177, 178, 180, 187] rather than a RMS. It is noteworthy that most recent studies in 3D-US calibration present calibration precision as an average metric; our results would definitely be artificially improved if they were computed this way.

Calibration precision also depends on probe motions. It has been shown that acquisitions by linear translation of the probe give significantly better precision than acquisition by titling [178] which is a difficult task to achieve in freehand tracking. In addition, the reproducibility of calibration is limited in freehand. To ensure reproducible

3D-US freehand results, a pivoting cradle for mechanical sweeping was even incorporated into the probe calibration procedure in [181]. The robotic scanner has the advantage of being repeatable in scanning paths for US image acquisitions . This key feature is what permitted the in-depth analysis of US image parameters to characterize calibration performance.

Another benefit in this study is our adaptation of the Z-phantom with micrometer size non-water absorbable material wire (i.e., polypropylene). Previous studies showed drawbacks in identifying Z-fiducials in US images [179, 180]. Smaller wires (i.e., 0.2-mm diameter), higher frequency probes (i.e. 10 MHz) [178], or mounting a thin rubber membrane on top of the Z-phantom were thought to improve this task [180]. Better calibration precision was achieved in our study compared to prior works.

In the literature on robotics, calibration precision can be compared with a limited number of studies. Using the same 3D-US robotic system and a 10-MHz US linear probe at a 6 cm US image depth, an improvement in precision to 0.93 mm RMS (600 observations) has been obtained with the Z-phantom compared to the X-wire calibration method that allowed us to obtain a 3.5 mm RMS precision (76 observations) [148]. Moreover, our system showed a better precision at 0.58 ± 0.36 mm RMS (600 observations) for a 8 cm US image depth compared to another robotic system evaluation with a plane wire calibration method that achieved 1.23 ± 0.65 mm (780 observations) [176] mean precision with a 14-MHz linear array probe at the same image depth of 8 cm.

Some disadvantages exist with the Z-phantom calibration procedure. Our method was tedious because segmentation of wires was manual and images contained speckle noise. Automatic segmentation methods of Z-fiducial collinear points in predefined search regions have already been developed, but these approaches are known to have larger variations than a manual operator [178, 180]. These promising algorithms could enhance the efficiency of Z-phantoms if segmentation becomes more robust. Also, errors are introduced into the calibration performance when the medium (polypropylene wires immersed in water) has a different speed of sound than human tissues (1540 m/s) assumed by the US scanner [71, 180]. The speed of sound impact on calibration has not been explored in this study because we judged it to be minimal.

Finally, in this work, we have demonstrated that satisfactory results could be achieved with a Z-phantom to calibrate a 3D-US imaging robot. Precisions favorably comparable to other studies have been obtained for different US image settings. In clinical practice, the calibration procedure needs to be fast and repeatable. To improve efficiency, this calibration procedure should be performed only once to characterize US image settings that match the target clinical application. A special adapter that ensures repetitive and precise attachment between the robot handle and the US probe should be conceptualized for this purpose. Also, a robust automatic segmentation algorithm should be used with typically gel-based agar incorporated into the Z-phantom to reduce US image artifacts due to possible reverberation. Another alternative would be to use raw digital radiofrequency signals [188, 189] instead of B-mode images to improve segmentation. However, this would require further hardware and software developments into the 3D-US robotic system and post processing of RF signals.

4.6.2 3D reconstruction performance evaluation on a lower limb-mimicking artery

In this study, reconstruction accuracy to represent a 3D vessel geometry was evaluated between 0.40 and 1.74 mm (Table 8) with significant differences observed for all US image settings investigated. Vessels reconstructed were more accurate at smaller depths (0.87 ± 0.08 mm) even if the calibration transform used provided less precision under these conditions (Table 7). This can be attributed to the higher pixel density around the vessel at smaller depths; the “disease-free” vessel lumen covered a range from 3 to 3.8 cm within the phantom. According to Table 8, the optimum reconstruction was obtained by placing the focus beam depth slightly below the vessel, at 4-5 cm. Reconstruction accuracy was the best when the depth setting of 7 cm was zoomed at 3:7 (0.40 ± 0.03 mm). This result was not anticipated, as the highest magnification 2:7 zoom was expected to provide the best reconstruction accuracy because the optimum precision of 0.47 mm was obtained for these settings. Poorer accuracy can be produced by US image artifacts becoming larger with zooming.

Area is another measure that we used to express the accuracy of the 3D vessel geometry. Most area profiles showed underestimations with 2 axisymmetric stenoses spaced apart at approximately the same distance for different US image settings (Fig. 4.7). This information reveals distortions in vessel shape where an oval and near elliptical geometry could be reconstructed. At 7-cm depth, 4-5 cm focus beam depth and 3:7 zoom setting, reconstructed vessels showed the best fidelity to the circular gold standard geometry. These observations reflect reconstructed accuracies of Table 8.

Overall, errors in vessel representations are attributed to the phantom fabrication process, segmentation of US images, robot intrinsic performance, and to the reconstruction procedure. Firstly, the fabrication process of the vascular phantom has -1.4% error in diameter [163]. This small contribution may nevertheless be important because the gold standard geometry was based on this model. Secondly, the segmentation algorithm used to detect the vessel lumen was adapted from a method implemented for IVUS images [41]. The segmentation accuracy in our images remains unknown and not comparable to IVUS reports. A slight error of a few pixels in segmentation can translate into errors of some mm in 3D vessel representation. Thirdly, another contributor to the vessel reconstruction quality is the robot performance in localizing an object in space. As reported earlier [148], our robot has a positioning accuracy of 0.46-0.75 mm that is repeatable at 0.20 mm, and an inter-distance accuracy of 0.26-0.61 mm. Among these performance measures, only the x, y, z inter-distance accuracy can be compared with reconstruction errors reported in Table 8 (0.40-1.74 mm). As expected, reconstruction errors were slightly larger than the robot inter-distance accuracy because the former measure includes all together the abovementioned contributing uncertainties (i.e., phantom, segmentation and reconstruction performances). Because 3D vessel reconstructions were co-registered with the gold standard vascular phantom geometry before assessing errors of Table 8, the robot positioning accuracy and repeatability are less relevant in this discussion. Lastly and to conclude this section, we support the hypothesis that the reconstruction procedure was the main source of error of Table 8 because it derives directly from the accuracy of the calibration transform (Eq. (11)).

4.6.2.1 Comparison with the literature

The 3D lower limb-mimicking artery was evaluated for different calibration transforms. Performance was assessed in terms of distance (reconstruction) accuracy and areas. Other similar calibration studies but with different calibration methods (i.e., X-wire, wall, three-wires, Cambridge phantom, etc…) also examined performance of 3D-US systems in distance accuracy but only on 1-D or 2-D reconstructed feature-based target points from the calibration phantom itself or from a simple independent geometric object (e.g. balloon or pin heads). We summarize their results relative to our 0.87-1.74 mm 3D vessel reconstruction accuracy obtained for the 5 to 8 cm US image depths, fixed 4-5 cm focus beam depth and no zooming (Table 8). Recall that our findings were obtained with a 10-MHz linear array probe for 10 vessel reconstructions (approximately 6,000 points per reconstruction).

Z-phantom studies with an electromagnetic freehand tracking and a 3.5-MHz phased array have reported 0.23 ± 2.89 mm distance accuracy for 960 inter-steel bead measurements at 9 cm US image depth [179], whereas inter-Z-fiducial analyses using optical freehand tracking devices with a 10-MHz linear array probe had 1.15 ± 0.43 mm distance accuracy for 810 measurements at 8 cm US image depth [178]. Other Z-phantom studies report results for inter-targets and feature length measurement accuracy between 0.2 and 1.2 mm with optical systems and probes ranging from 3.5 to 7.5 MHz at 6-12 cm US image depths with less than 30 samples [181, 183, 187].

Moreover, alternative phantom calibration methods (i.e., X-wire, wall, three-wires, Cambridge phantom, etc…) with electromagnetic and optic freehand tracking devices in the literature have inter-target distance accuracies that range from -0.19 µm to 3.0 mm [71, 78, 161, 177, 180, 185]. Of course, it is not possible to directly compare the accuracy of all these studies to our results because many differences exist in calibration phantoms, US probe frequencies, US image settings and distance accuracy metrics.

Generally, performances of our calibrations for accurate vessel reconstructions are of similar magnitude as the inter-target distance accuracy reports of 3D-US optical systems (best positional accuracy [71]). Electromagnetic systems seem to show significantly better

results in inter-target distance accuracy than other systems. However, most of these reported measures in the literature are misleading because unsigned values are computed into their average, thus improving their overall accuracy. Also note that valid clinical 3D-US system accuracy cannot be extrapolated from these inter-target measures because they have no relation to the clinical context aimed.

Studies performed in clinic with 3D-US freehand systems have preferred to directly show the clinical potential of their technologies for monitoring human vessel pathologies over time [100, 190-192]. Because most studies have not validated their 3D reconstruction with a gold standard, the validity of their 3D systems to accurately represent a 3D geometry is unknown, and if they did [99], no information is available to assess the calibration method used and its performance. Consequently, diseased vessels can be misdiagnosed when unidentified systematic errors intermingle with the pathology in their 3D representations.

Also, our study has the advantage of being comparable to 2 others that employed a similar vascular phantom and the same US scanning equipment and probe. In the first investigation, the accuracy to reconstruct vascular phantom diameters varied between -0.37 and -0.90 mm at 6 cm US image depth with a previous X-wire calibration method and the same 3D-US robotic imaging system [148]. In our experiment, reconstruction accuracy was 1.20 mm at this particular depth. The results varied between studies because of the way measurements were assessed. In , the diameter at specific cross-sections of the 3D representation was taken into account and evaluated on gold standard geometry with micro-caliper measures (unsigned errors). In the current paper, entire points of surface reconstruction were assessed on gold standard geometry, and 10 reconstructed samples were computed for the mean measure. Evidently, the present report is more rigorous than our previous work in [148] to validate the 3D-US imaging robotic system. The second study, with similar vascular phantoms, evaluated in-stent restenoses *in vitro* with an electromagnetic system and a linear step motor for 3D reconstructions [193]. A value of 1.0 ± 0.1 mm RMS calibration accuracy was achieved with the STRADWIN software at 4.5 cm US image depth with no available information on zooming and focus beam depth. Our system showed better results with 0.87 ± 0.08 mm reconstruction accuracy at 5 cm US

image depth. However, the *in vitro* in-stent restenoses study provided no information relative to precision analysis of calibration parameters. Thus, their suggestive results remain inconclusive and not equivalent.

The goal of calibration is to find the correct (or optimum) transform that allows 3D geometry to be reconstructed accurately. Our study attained this objective by evaluating the performance of different US image settings that affect calibration transformation accuracy to reconstruct a 3D lower limb-mimicking artery. Our validation was the first of its kind for lower limb 3D-US vessel reconstruction. In this work, reconstruction errors and cross-sectional areas completely allowed the quantification and identification of distortions obtained with the robotic scanner on our 3D vessel representations. Future analyses will include the reconstruction of complex lower limb arterial geometries, multimode imaging comparisons, stenosis quantification, and a possible clinical study to demonstrate the benefits of this robotic scanning system.

4.7 Conclusion

The 3D-US robotic scanner was validated to adequately reconstruct a 3D lower limb-mimicking artery. A Z-phantom calibration procedure was completed with this robotic system and, as a result, calibration transforms were characterized with US image settings according to precision and 3D reconstruction accuracy. Calibration precision was found to perform best at deeper US image settings with focus beam depths corresponding to target Z-fiducials located on the US scan and at the highest zoom. Reconstruction accuracy was evaluated in terms of distance accuracy with respect to a gold standard geometry of a vascular phantom. The cross-sectional area was also analyzed along the length of the reconstructed vessels. Optimum US settings to accurately reconstruct the vessel were at lower US image depths, a focus beam depth slightly below the vessel, and a mid-sized window zoom to reduce artifacts. These results are likely suitable for the clinical evaluation of stenoses. Further developments and validations of the robotic system are nevertheless necessary to provide a platform that would meet clinical needs.

Acknowledgments

This work was supported in part by the Canadian Institutes of Health Research (CIHR) under Grant MOP #53244. Dr Soulez is recipient of a Clinical Research Scholarship Award of the Fonds de la recherche en santé du Québec (FRSQ). Ms. Janvier is the recipient of studentship awards from Fonds de la recherche sur la nature et les technologies du Québec, TD Canada Trust, the Institute of Biomedical Engineering at Université de Montréal, the Quebec Black Medical Association and the End of Study Grant from the Faculty of Graduate and Postgraduate Studies at Université de Montréal. The authors are grateful to Ms. Zhao Qin, Mr. Boris Chayer, Ms. Marianne Fenech and Ms. Marie-Hélène Roy-Cardinal for technical support. The authors are grateful to Mr. Ovid M. Da Silva for manuscript editing.

Chapter 5

A 3D ultrasound imaging robotic system to detect and quantify lower limb arterial stenoses: *in vivo* feasibility

A painter told me that nobody could draw a tree without in some sort becoming a tree; or draw a child by studying the outlines of its form merely . . . but by watching for a time his motions and plays, the painter enters into his nature and can then draw him at every attitude . . .

Ralph Waldo Emerson

5.1 Forward

This chapter presents the submitted paper in the journal *IEEE Transactions on Biomedical Engineering* by the authors Marie-Ange Janvier, Louise Allard, Gilles Soulez and Guy Cloutier[30].

This paper describes the methods developed to evaluate the robotic system's ability to localize and quantify arterial stenoses. An *in vitro* study is first performed on a lower limb mimicking vascular phantom with a realistic geometry. Then, the feasibility *in vivo* is executed on a lower limb artery. The CTA is employed to analyse the geometry and to localize stenoses.

[30] The co-authors Gilles Soulez and Guy Cloutier are the supervisors of the thesis. The co-author Louise Allard helped in structuring the experimental design, organizing and editing the manuscript.

5.2 Abstract

The degree of stenosis is the most common criterion used to assess the severity of lower limb peripheral arterial disease. 2D-ultrasound (US) imaging is the first-line diagnostic method for investigating lesions, but it cannot render a 3D map of the entire lower limb vascular tree required for therapy planning. We propose a prototype 3D-US imaging robotic system that can potentially reconstruct arteries from the iliac in the lower abdomen down to the popliteal behind the knee. A short, realistic, multimodal vascular phantom was first conceptualized to evaluate the system's performance *in vitro*. Geometric accuracies were assessed in surface reconstruction and cross-sectional area in comparison to computed tomography angiography (CTA). Mean surface map error of 0.55 mm was recorded for 3D-US vessel representations, and cross-sectional lumen areas were congruent to the CTA geometry. *In vitro*, stenotic lesions were properly localized and severe stenoses up to 98.3% were evaluated with –3.6 to 11.8% errors. The system's feasibility in detecting *in vivo* stenoses on a femoral artery segment was also investigated clinically and compared to CTA. Altogether, these results encourage future developments to increase the robot's potential for adequately representing lower limb vessels and clinically evaluating stenotic lesions for therapy planning and recurrent non-invasive and non-ionizing follow-ups.

5.3 Introduction

Atherosclerosis is the principal cause of peripheral arterial disease (PAD) that forms diffuse lesions in lower limb vessels [7]. An arterial diameter reduced by more than 50% represents a significant stenosis where invasive therapy (i.e., endovascular or surgical revascularization) could be judged necessary [194]. Usually, these procedures require planning with precise information on stenosis severity, location, length and non-diseased vessel diameter. It is common to follow the patency of endovascular or surgical therapies to detect restenosis or progression of atheroslerosis [195]. Indeed, the rate of restenosis after 1 year following balloon dilatation and stenting of the femoro-popliteal artery is around 40 to 60 % [52]. The patency of vein graft bypass also requires long-term surveillance because of the occurrence of stenoses due to myointimal hyperplasia [196].

Ultrasound (US) is the first-line imaging method employed clinically to investigate lower limb arterial lesions. Diagnosis relies on pulsed-wave Doppler and color Doppler flow assessment, and B-mode imaging to define atherosclerotic plaque morphology [26]. Because most US-based evaluation methods are limited to 2D image plane views, they do not provide sufficient information to guide interventional therapies. Following screening by US, symptomatic peripheral arterial disease requiring invasive therapy are planned with computed tomography angiography (CTA), magnetic resonance angiography (MRA) scan or invasively with digital subtraction angiography (DSA) [26, 194]. While these latter imaging techniques can map the entire lower limb vascular tree in 3D rendering, CT imaging is ionizing and requires injection of allergenic iodine contrast agent, whereas MRA is costly. The gadolinium-based contrast can induce nephrogenic systemic fibrosis in patient with renal failure and its accessibility is limited by several contra-indications related to high magnetic field. Given the importance of quantifying stenoses and mapping their localization for therapy planning and patient follow-up, the development of a precise non-invasive US-based 3D mapping technique is of clinical importance for lower limb vascular evaluation.

3D-US imaging is an economical and safe technology mainly used in research for anatomical or volumic representation. Since it can provide the physician with a complete mapping of lower limb vessel, it has the potential to increase diagnosis confidence and provide accurate stenosis localization and quantification. Already, *in vivo* feasibility in imaging carotid arteries, lower limb venous bypass and the brachial plexus (i.e., nerve fibers running from the spine that runs to the neck, armpit and the arm) have been demonstrated using 3D-US systems based on linear step motors, electromagnetic and optical freehand tracking techniques [91, 99, 111, 197, 198]. These devices are ideal to localize lesions on short segments, but the restricted range of probe motion detection, signal interference or tracking visibility limits their utility in long and tortuous lower limb arteries [106, 155, 173].

Robotic systems represent a novel alternative for lower limb stenosis location and quantification because they can simultaneously control and standardize the 3D-US image

acquisition process with high precision and flexibility. While most 3D-US prototype robots attempt to increase the capability of clinicians in prostate brachytherapy and tele-echography of the abdomen [175, 199, 200], only two designs exist for vascular examination. Hippocrate is the first feedback medical robot designed with safety strategies to scan short vessel segments, such as the carotid artery, and to perform tonometry measurements synchronized with the heart rate [140]. To the best of our knowledge, no other follow-up study has been conducted with this robot besides a non-invasive investigation of endothelial function [141]. In fact, the robot's mechanical architecture was later adapted to a new design for reconstructive skin surgery [201]. The University of British Columbia's medical US image-guided robot is designed for performing tele-examination scanning of the carotid artery [146]. Shared control between operators, the robot controller and US image processor make the real-time visual servoing of US probe movements possible. Nevertheless, this robot's architectural design has constrained movements in its workspace and a limited 3 degrees of freedom controller because it is specialized for short, close to rectilinear paths such as the carotid artery.

To provide accurate 3D-US scanning of lower limb vessels, a 3D-US imaging robotic system was developed by our group [148]. The system can scan short and long segments of leg arteries in "freehand", using a 'teach' mode, and reproduce the manually-taught path in 'replay' mode. When scanning along a path with this robot, clinicians can expect to acquire 2D axial US images with their corresponding x, y and z positions at a constant speed and contact pressure to correctly represent vessels in 3D. The robust positioning accuracy and repeatability achieved previously over the robot's entire workspace disclosed the broad operational range of our system for tracking lower limb vessels [148]. Also, we recently showed, with a Z-fiducial calibration procedure, that we could adequately register 2D-US images into our robot referential to reproduce a mimicked axisymmetric vessel artery with fidelity [202]. The present study aims to demonstrate the performance efficacy of this robotic system under conditions closer to the clinical context. Two objectives were targeted: (1) to assess the accuracy of the robotic imaging system *in vitro* in locating and quantifying lower limb vessel stenoses with a phantom mimicking a realistic geometry; and (2) to evaluate the ability of this robotic imaging system for 3D mapping of a diseased femoral artery *in vivo*. For both objectives, 3D US reconstructions were compared with the

CTA as a gold standard examination.

5.4 Materials and methods

5.4.1 3D-US imaging robotic system

As illustrated in Fig. 5.1, the 3D-US imaging robotic system contains a robotic arm (F3 Articulated Robot, CRS Robotics Corporation, Burlington, Ontario, Canada), an US echograph and a personal computer with the US robotic scanner software (Integral Technologies Inc., Laval, Quebec, Canada). A Vivid-5 scanner (General Electric, Chicago, IL, USA) equipped with a FLA-10 (10 MHz) linear array probe was used for *in vitro* experiments, whereas a HDI-5000 (Philips Healthcare, Andover, MA, USA) with a L12-5 (12 MHz) linear array probe allowed scanning the patient with lower limb arterial disease. Digitized 480 x 640 pixel format B-mode and color Doppler flow images were acquired with corresponding robotic arm positions stored for future 3D reconstructions. This robotic system has previously been described in details [148].

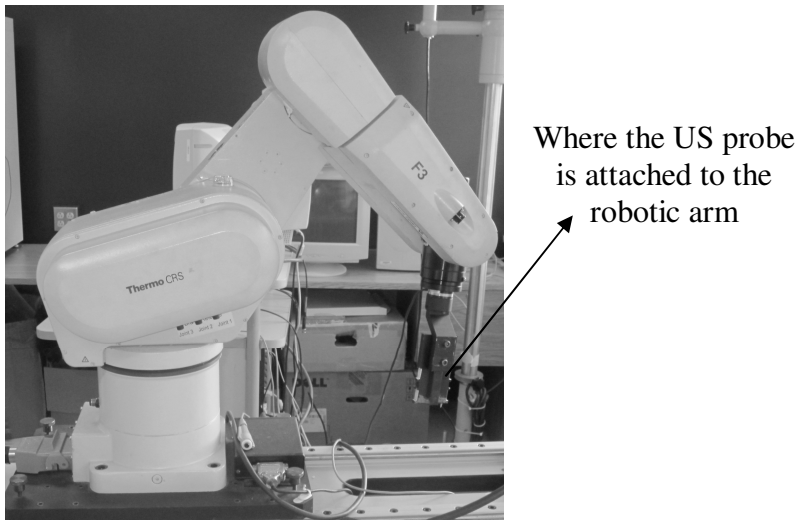

Figure 5.1: F3 CRS robotic arm used in the 3D-ultrasound (US) imaging robotic system.

5.4.2 In vitro analysis of a realistic vessel segment

5.4.2.1 Vascular phantom and experimental set-up:

The geometric accuracy of the robotic system in reconstructing 3D vessels was evaluated with a phantom replicating a human iliac artery with multiple stenoses. This model was created from a 3D reformation of a multi-detector computed tomography (CT) scan acquisition in a patient with a peripheral arterial disease of the iliac artery. The phantom was prepared according to a manufacturing process described previously [203]. Fig 5.2 shows a 3D vessel representation obtained from the CAD (computer-aided design) file employed to prepare the moulding prototype. This segment presents two severe stenoses identified as *S1* and *S2* with 97.3% and 98.3% area reductions, respectively. The vessel's central axis at both ends was positioned at 3.4 cm from the top cover of the phantom box; it was 4.0 cm at the location identified on the figure (Fig. 5.2b), and the length *L* of the scanned iliac segment was 98.7 mm from the aortic bifurcation.

Dimensions of CAD 3D representation of the vessel were measured on cross-sectional planes. The maximal diameter of the non-diseased vessel segment was D = 6.5 mm and the minimum diameters at stenoses were $S1$ = 1.4 mm and $S2$ = 1.2 mm (Fig. 5.2a). Lengths of stenoses were measured as the distance between pre-stenotic and post-stenotic maximum vessel diameters ($L1$ = 14.0 mm and $L2$ = 28.1 mm). The distance between maximum diameter reductions at both stenoses *S1* and *S2* was LS = 20.0 mm.

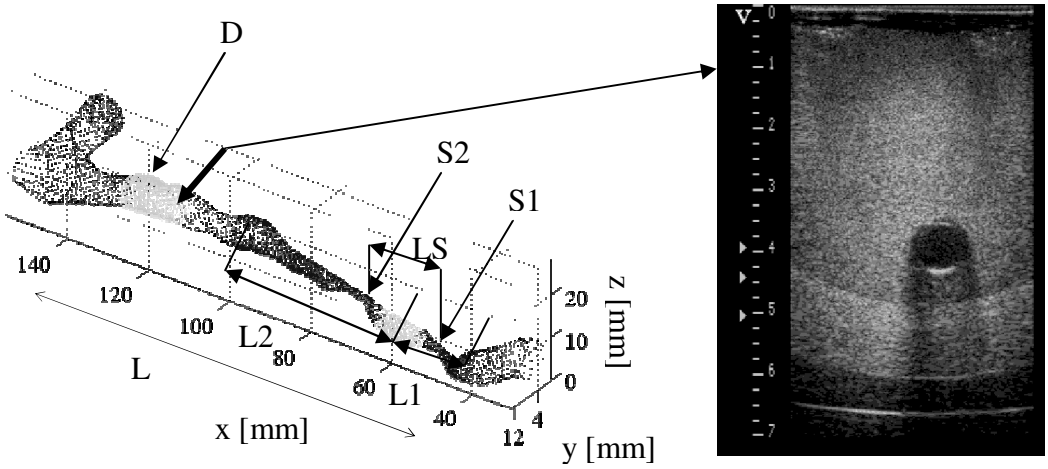

Figure 5.2: (a) CAD representation of a realistic vascular phantom embodying an iliac artery with 2 severe stenoses (*S1* and *S2*). *L1* and *L2* represent their respective lengths, and *LS*, the shortest distance between maximal points of the stenoses. *L* is the total length of the vessel and *D* is the non-diseased vessel diameter. (b) B-mode cross-sectional image of the vascular phantom where its location is indicated by an arrow in (a). The shadowing on the B-mode image is attributed to the presence of a polyurethane membrane mimicking the vessel wall and used to avoid the diffusion of CTA contrast outside the vessel lumen.

5.4.2.2 3D-US vessel representation

As in [202], a Z-phantom calibration procedure of the 3D-US imaging robotic system was first required to assure correct vessel representation. This procedure estimates the calibration transform that registers the US image plane into the robot referential. Then, the vascular phantom filled with degassed water was set firmly into the robot's workspace. US gel (Parker Laboratories, Fairfield, NJ, USA) was applied on the phantom's top cover, and US images were acquired at a 7-cm image depth, a 4-5-cm single focus beam depth and a 3-cm window size zooming (3:7 setting on the Vivid-5 scanner) to match scanning conditions producing the best accuracy for 3D vessel representation [202]. Then, a quasi-parallel plane US scan path was taught to the robot by a technician and automatically replayed 8 times. During the robot 'replay' mode, cross-sectional US images of the mimicked diseased artery were captured to reconstruct 8 3D representations of the vessel with surface rendering. For 3D reconstruction, the vessel lumen of each US image was segmented with a fast-marching method based on gray level statistics and gradients adapted from [41]. Then, each pixel of the segmented lumen contour was mapped into the robot referential using the calibration transform and corresponding x, y, z probe positions [202]. To provide a 3D surface rendering of the reconstructed vessel, the transformed lumen

contours were re-sampled on a 300×20 rectangular grid, interpolated and realigned normal to the vessel center axis, as in [184].

5.4.2.3 CTA representation of the vessel

Because CTA imaging has the best accuracy for PAD evaluation [26], a Somatom Sensation 64-slice scanner (Siemens, Erlangen, Germany) was utilized to acquire images of the vascular phantom according to a standard clinical protocol. The imaging settings were: 217-mA current density, 120-kV peak voltage, 1.0-mm slice thickness, 0.6-mm reconstruction interval, and 38.0-cm field of view for a 512×512 matrix size. The phantom lumen was filled with a 2.8% v/v (volume concentration) solution of 430 mg/ml iothalamate meglumine (Conray 43, Mallinckrodt Medical, Pointe-Claire, Quebec, Canada) diluted in 0.9% NaCl solution. 3D-CTA image representation was achieved with a maximum intensity projection (MIP), a volume rendering reformation and 2.0-mm axial reformations, with the Visual software (version 1.4, Object Research System (ORS), Montreal, Quebec, Canada). This representation was later transformed into a 3D binary file that was converted into 3D contour points with MatLab (version 6.5, The MathWorks Inc., Natick, MA, USA).

5.4.2.4 Geometric evaluation of 3D vessel representations

The reconstructed lumen surface, vessel cross-sectional areas, localization and quantification of stenoses imaged with the 3D-US robotic system were compared to the CTA gold standard method. Given that each imaging approach presents its own sources of errors, accuracy in 3D vessel representation was also determined with the CAD file used to produce the vascular phantom.

5.4.2.4a Comparative analyses of the reconstructed surfaces

Before comparing vessel geometries, a rigid registration was performed by using an iterative closest point algorithm to align the two 3D vessel models [204]. This method, applied on free-form curves, surfaces and 3D-shapes, efficiently matches 2 ranges of data points without requiring pre-processing or feature extraction. The algorithm uses a closest point estimation method and an iterative absolute orientation algorithm [205]. The result is

an optimal transformation matrix (translation and rotation) that minimizes the mean square distance between the two 3D models.

Surface reconstruction errors were evaluated by measuring the absolute distance between points on the 3D evaluated geometry and on the gold standard vessel representation, as expressed by:

$$E_{i,j,k} = S_{tested}(i,j,k) - S_{ref}(i,j,k) \qquad (17)$$

where S_{tested} is the surface points of the 3D reconstructed vessel evaluated, S_{ref} is the surface points of the reference method, $1 \le i \le X$ where X is the number of grid points along the x axis, $1 \le j \le Y$ where Y is the number of points along the y axis, and $1 \le k \le Z$ where Z is the number of points along the z axis. If the number of cross-sections differs between US, CTA and CAD 3D models, Eq.(17) uses for reference the representation with the minimum longitudinal distance X. For all comparisons of 3D reconstructions between US (B-mode, color flow), CTA and CAD files, the absolute value of this measure was tabulated into one mean (sample size = $X \times Y \times Z$ where chosen dimensions were those of the reference model).

5.4.2.4b Lumen cross-sectional areas

Cross-sectional areas were measured along the x-axis of each 3D-reconstructed vessel on US (B-mode and color flow) and CTA, and on the CAD file. The area was evaluated with *Polyarea,* a polygon-specific function of Matlab, which computes the average number of pixels inside a clockwise closed contour. For all 8 US reconstructions, the mean ± standard deviation of cross-sectional areas were assessed over the vessel length (sample size = X, which is the number of cross sections).

5.4.2.4c Localization and quantification of stenoses

Stenoses were localized at perceived stenotic sites. Quantification of stenoses was described as the percentage of lumen reduction compared to a reference vessel in surface. This measure, S_{area}, was expressed by Eq. (18) and was evaluated with respect to the known degree of vessel narrowing, as determined by the CAD file of the 3D vessel representation (see *S* labels in Fig. 5.2).

$$S_{area} = 100 \times \left(\frac{A_D - A_i}{A_D} \right) \qquad (18)$$

where A_i defines the area of a cross-sectional vessel lumen, A_D expresses the reference measure where the maximal value is identified in the non-diseased vessel segment (see label *D* in Fig. 5.2). The degree of stenosis was the maximal quantified value at the stenotic site. Dimensions of stenoses were measured in terms of length using the CAD file 3D representation of the vessel for reference (see Section 5.4.2.1 and labels *L1, L2 and LS* in Fig. 5.2).

5.4.3 In vivo feasibility study

5.4.3.1 3D-US imaging robotic system: experimental set-up, data acquisition and processing

To evaluate the feasibility of the robotic system, a pilot study was conducted on 1 patient, an 82-year-old man with evidence of occlusive PAD, as shown by a previous CTA exam. The study received approval from our institutional review board, and informed consent was obtained from the patient.

The volunteer lay supine with the target limb rose at the height of a supportive pillow. The radiologist first manipulated the US probe attached to the robotic arm in "teach mode" (i.e., a mode enabling the learning of a "freehand" scan with minimum torque applied on robot articulations) to inspect the femoral artery, starting from the femoral bifurcation down to the distal femoral artery. Both B-mode and color Doppler flow exams were performed in teach mode to store the femoral artery's path. These taught trajectories were then replayed by the robot at a constant speed with *x*, *y*, *z* coordinate registration for each acquired cross-sectional image.

US image settings in both B- and color flow modes were an image depth of 6 cm, a 2-4 cm focus beam depth and no zooming. In B-mode, the scan path was close to perpendicular with respect to the vessel longitudinal axis. In color flow mode, optimal angles allowing Doppler shift to fill the vessel lumen, according to the perception of the clinician, were chosen along the scan path (the mean angle was determined in post-processing from the *x*, *y*, *z* coordinates of each acquired image and it was 54.4^{o}). The wall

filter was set to 87 Hz. The patient's leg remained seemingly immobile throughout the entire examination but movements were not monitored. Collected images were then analyzed and processed for 3D vessel reconstructions according to the same methods described for the *in vitro* study in Section 5.4.2.2.

5.4.3.2 CTA: Experimental set-up, data acquisition and processing

The lower limb CTA exam was performed with the same scanner and afore-mentioned parameter settings as in the *in vitro* study (see Section 5.4.2.3). The patient was placed in a supine position, feet-first in the scanner with legs at the isocenter and a sweep was executed from the abdominal aorta to the patient's foot with a 40.0-cm field of view. A 120 cc bolus of a non-ionic contrast agent Omnipaque 370 (iohexol 370 mg iodine/ml, GE Healthcare, Buckinghamshire, UK) was injected at a rate of 4 cc/s with an intravenous superficial brachial catheter. Collected data were processed to reconstruct in 3D the right femoral artery with the method outlined in Section 5.4.2.3. Calcifications in CT scans were excluded from the vessel lumen based on threshold methods.

5.4.3.3 Geometric evaluation of 3D vessel representations

Geometric analyses of the lower limb femoral artery reconstructed from US and CTA images were conducted by aligning the corresponding segment from the femoral bifurcation. The reconstructed surface and lumen cross-sectional areas were then compared; quantification of stenoses was also performed. All methods for 3D rigid registration and performance assessment metrics were described earlier in the *in vitro* study of Section 5.4.2.4.

5.4.3 Statistical analysis

Pairwise analysis of variance tests (ANOVA) were performed with the Bonferroni method for geometric analyses of *in vitro* 3D vessel comparisons between the 3D-US imaging robotic system, the CTA scanner and the CAD file. These comparisons were also assessed *in vivo* between B-mode and color Doppler flow geometries. All statistical analyses were completed with OriginLab (version 7.5, OriginPro, Northampton, MA, USA). Results are mean ± one standard deviation.

5.5 Results

5.5.1 In vitro analysis of a short, realistic vessel segment

5.5.1.1 Comparative analyses of 3D vessel representations

Figure 5.3 gives examples of the vascular phantom lumen imaged with the 3D-US system in B-mode and CTA scanner, and the corresponding gold standard CAD file. Table I tabulates the total artery length and surface area of these three vessel maps. 3D-US provided the shortest vessel representation and the smallest surface, whereas CTA had the largest surface area when compared with the CAD file. Figure 5.4 presents comparative surface error maps for CTA and 3D B-mode US comparisons, CAD versus 3D-US and CAD versus CTA. For 3D B-mode US assessment, 8 reconstructions were used for comparisons and results were tabulated into one mean to display a surface error map. Significant differences based on one-way ANOVA were found among all mean surface error maps ($p < 0.05$).

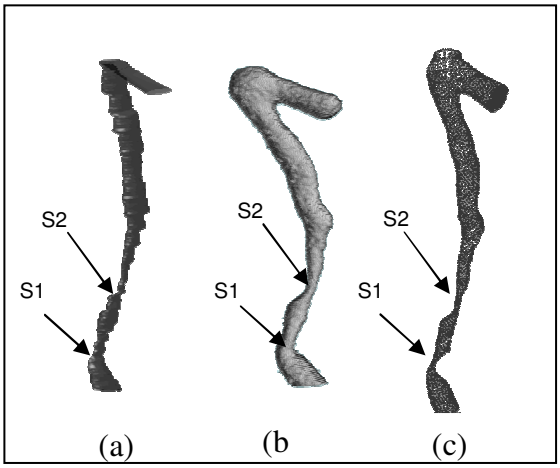

Figure 5.3: 3D vessel representations of the short, realistic vascular phantom with 2 severe stenoses (*S1* and *S2*) illustrated by (a) 3D-US, (b) CTA, and (c) the CAD file.

In the displays of Fig. 5.4, surface contour points were compared with the closest surface contour points of the reference model. Since the number of cross-sections differs between US, CTA and CAD 3D maps, in Eq. (17) the representation with the minimum longitudinal distance X was used for reference. Thus overestimations with respect to the reference 3D maps (B-mode in Fig. 5.4a and CAD in Fig. 5.4b and c) are shown in green-

yellow to red; whereas underestimations are displayed in navy-blue to dark blue. Therefore, in the evaluation performed between each representation, missing lengths (i.e., missing cross-sections) at the extremity resulted in large errors because closest reference surface points used in Eq. (17) were enlarged; we kept this information but it should not be viewed as an image distortion.

Table 9: Comparative analysis of 3D-reconstructed surfaces of the short, realistic vascular phantom

3D vessel representations	Total length *L* (mm)	Total surface (mm^2)	Sample size (*N*)
3D-US (B-mode)	89.4 ± 0.7	1884.5 ± 7.1	8
CTA	95.9	2073.2	1
CAD	98.7	2015.9	1

As shown in Fig. 5.4a, CTA (tested geometry) provided an overestimated vessel representation of the reconstructed surface compared to 3D-US (which is the gold standard reference here). The absolute mean error of 8 vessel samples was 0.55 ± 0.04 mm with a range of 0.03 - 3.6 mm (these statistics exclude artifacts at the extremity). For each error map where the CAD file was the gold standard reference (Fig. 5.4 b-c), the surface reconstruction error of the tested geometry generally indicates an overestimation of the vessel size, except for B-mode US around the *S2* stenotic site and the non-diseased area for the CTA where an underestimation is noted. 3D-US (B-mode) had an absolute mean surface error of 0.96 ± 0.54 mm (Fig. 5.4b, range of 0.06 to 3.6 mm,). CTA disclosed the smallest errors of 0.60 ± 0.39 mm (Fig. 5.4c, with a range going from 0.05 to 2.2 mm).

Figure 5.5a shows an example, from one B-mode US reconstruction, of the cross-sectional lumen *x*, *y*, *z* orientation along the vessel axis, whereas Fig. 5.5b compares quantitatively areas obtained in B-mode US ($n = 8$), CTA and CAD. There was a significant statistical difference ($p < 0.05$) based on one-way ANOVA between each mean cross-sectional area along *X* compared to the CAD file as well as for the 3D-US and the CTA comparison. CTA gave the largest representation of the vessel lumen compared to the CAD file, with a mean cross-sectional area error of 10.7 ± 11.3 mm^2 along *X*, whereas 3D

B-mode US resulted in a smaller mean cross-sectional area error of 4.3 ± 12.6 mm^2. The 3D-US vessel cross-sectional areas compared to CTA had a mean error of -6.4 ± 9.8 mm^2.

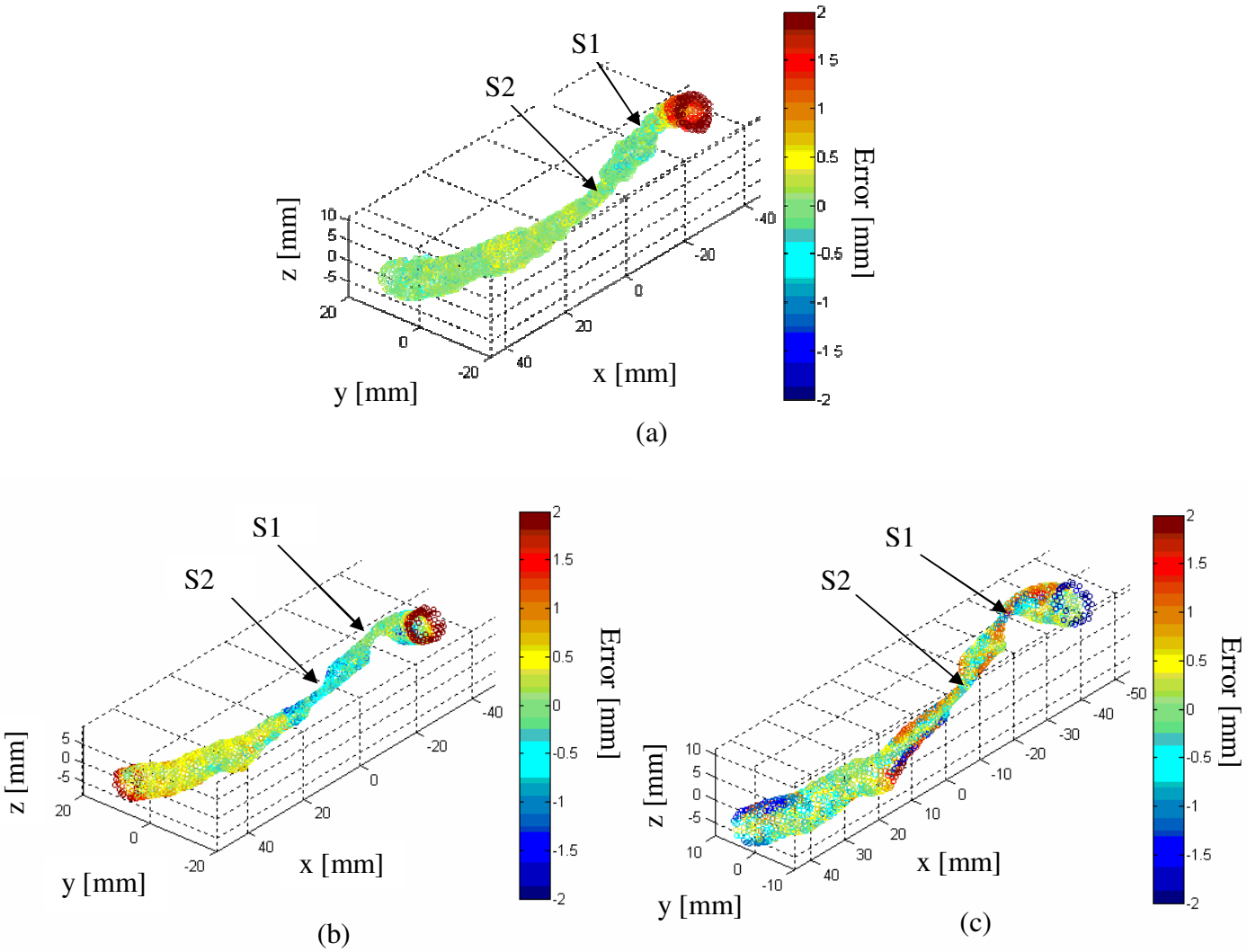

Figure 5.4: Comparative analysis between 3D vessel representations of the realistic vascular phantom with 2 severe stenoses (*S1* and *S2*). (a) On the B-mode 3D-US vessel representation, mean surface reconstruction comparison between CTA and 3D-US is displayed. On the CAD file, the respective surface reconstruction errors are shown with the (b) 3D-US (B-mode) and the (c) CTA.

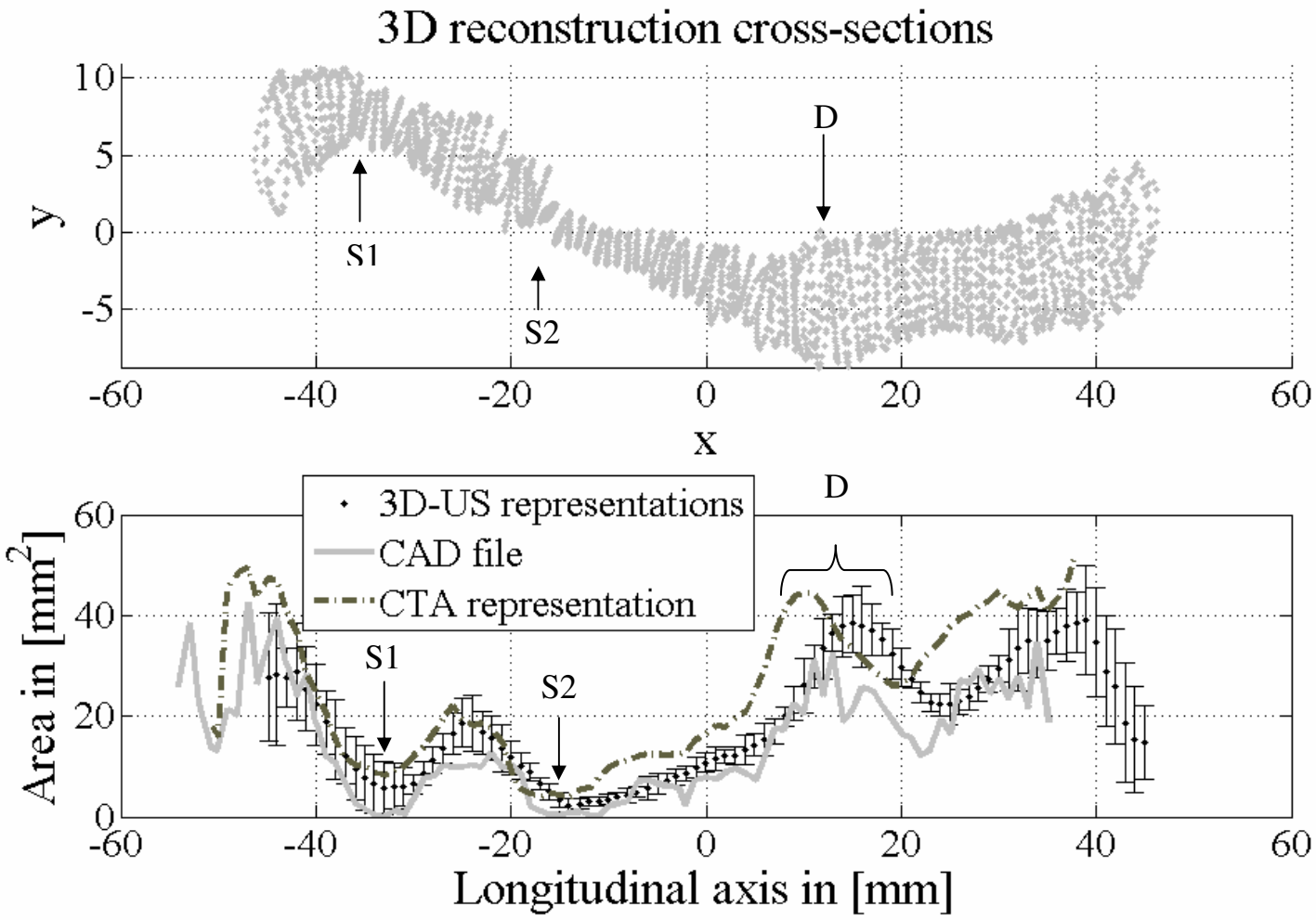

Figure 5.5: The cross-sectional lumen areas of the 3D-US, CTA and CAD file representations are shown for the realistic vascular phantom. S1 and S2 represent severe stenoses and D is the non-diseased vessel diameter.

5.5.1.2 Localization and quantification of stenoses

Stenoses *S1* and *S2* were localized in each 3D vessel representation (Fig. 5.5). They were then quantified according in (2) and summarized in Table 10. Both stenoses, in area reduction, were better assessed in 3D B-mode US compared to CTA. Table 11 summarizes lengths of stenoses; errors were either larger, equivalent or smaller with 3D-US than CTA, when compared to the CAD file.

Table 10: Quantification of stenoses of the realistic vascular phantom

Stenoses (%)	B-mode US (*N*=8 samples)		CTA (*N*=1 sample)	
	Measurement	Error	Measurement	Error
CAD *S1* (97.3)	85.6 ± 6.1	-11.8 ± 6.1	81.5	-15.8
CAD *S2* (98.3)	94.8 ± 1.9	-3.6 ± 1.9	91.5	-6.9

Table 11: Lengths of stenoses of the realistic vascular phantom

Length (mm)	B-mode US (*N*=8 samples)		CTA (*N*=1 sample)	
	Measurement	Error	Measurement	Error
CAD *L1* (14.0)	14.4 ± 2.5	0.4 ± 2.5	12.0	-1.96
CAD *L2* (28.1)	31.6 ± 2.0	3.5 ± 2.0	29.1	1.0
CAD *LS* (20.0)	19.0 ± 2.6	-1.1 ± 2.5	28.1	-1.1

5.5.2 In vivo feasibility study

Figure 5.6 shows a curved 3D-CTA MPR of the patient's right femoral artery displaying calcification and multiple stenoses. Figure 5.7a provides the CTA vessel representation with zooming of the middle segment in panels b & d to show comparisons of surface maps with 3D B-mode US and 3D color Doppler US. Corresponding error maps are presented in panels c & e, and quantitative assessments of the middle segment total length and surface area in each mode are summarized in Table 12. The B-mode 3D vessel representation provided a larger surface and length, and Doppler, shorter ones. As reported in Fig. 5.7c and 5.7e, both 3D-US vessel representations overestimated the CTA middle segment reconstructed surface points ($p < 0.05$ for both CTA-B-mode and CTA-Doppler comparisons). The absolute mean surface reconstruction error using Eq.(17) of the B-mode 3D vessel representation compared to CTA was 1.82 ± 1.31 mm with a range of 0.02 to 6.1 mm (Fig. 5.6c). It was doubled for color Doppler, indeed the absolute mean error was 2.99 ± 2.10 mm and the range was from 0.03 to 9.31 mm (Fig. 5.7e). It is to note that both

statistics exclude artefacts at the extremity. Similar conclusions can be made regarding the cross-sectional lumen areas evaluated in the middle vessel section in Fig. 5.8. In comparison to the CTA, significant differences ($p < 0.05$, one-way ANOVA) were found between the mean cross-sectional lumen area errors in B-mode (13.4 ± 11.1 mm^2) and color Doppler (25.2 ± 15.4 mm^2). Two moderate stenoses of 49.9 % and 56.3 % were quantified in the CTA longitudinal segment of [-60, -40] and [-20, 20] mm (see Fig. 5.8). In Doppler, the corresponding stenoses were localized at [-40, -20] and [0, 20] mm and quantified to 71.3 % and 78.6 % respectively. In B-mode, stenoses were localized at [-40, 0] and [0, 20] mm with a quantification of 88.9% and 89.8 %.

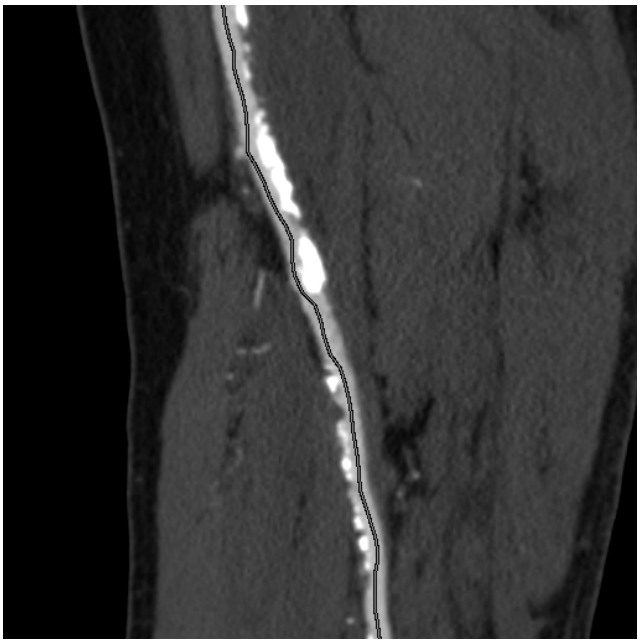

Figure 5.6: A volume rendering 3D reformation of the CTA on patient's right femoral artery.

Table 12: Comparative analysis of 3D-reconstructed surfaces of the Middle segment of the patient's right femoral artery

3D vessel representations	Total length L (mm)	Total surface (mm^2)	Sample size (N)
B-mode	136.6	2868.6	1
Doppler	115.8	2431.8	1
CTA	128.7	2702.7	1

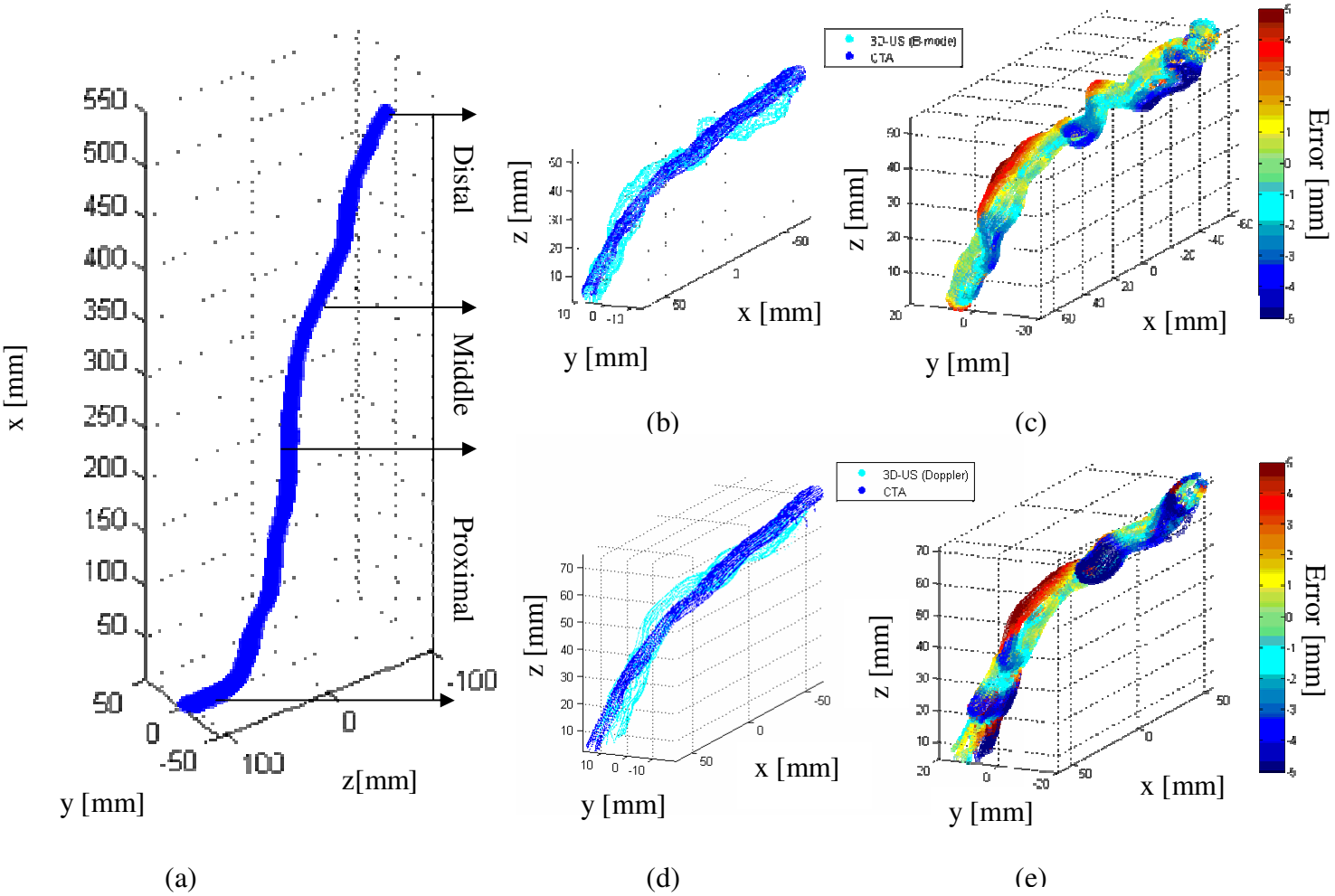

Figure 5.7: Entire CTA vessel representation of the patient's right femoral artery divided in 3 segments: proximal, middle and distal (a). The middle segment (from 220-370 mm) is presented in B-mode (b) and surface map errors on the 3D-US vessel representation (c). The same middle vessel segment in color Doppler flow is shown (d) and the surface map errors of the CTA representation (e) are displayed.

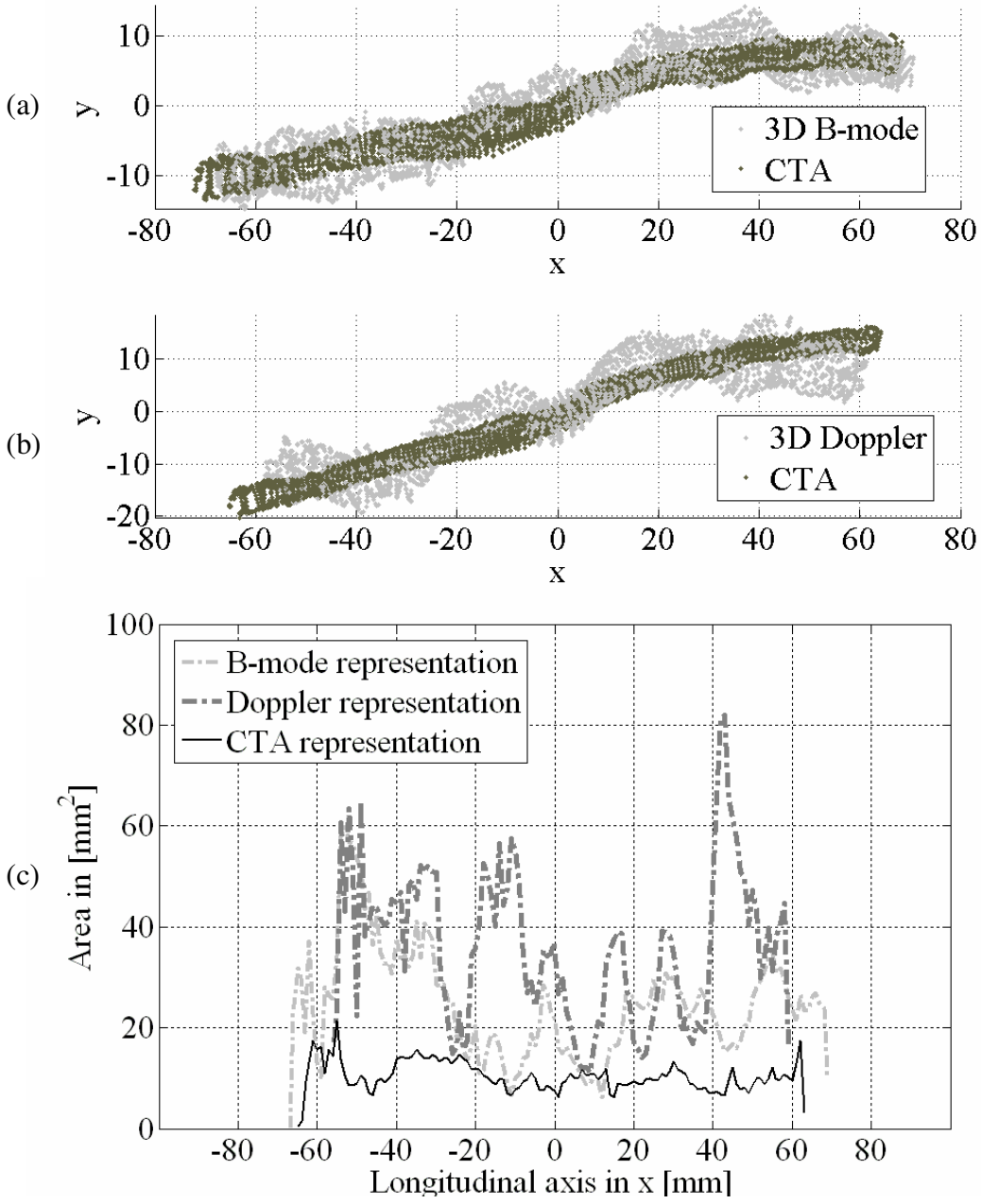

Figure 5.8: CTA 3D vessel representation of the middle segment of the patient's right femoral artery in B-mode (a) and color Doppler flow (b). The corresponding cross-sectional lumen areas are also presented.

.

5.6 Discussion

5.6.1 Analyses of 3D vessel representations

In this study, *in vitro* and *in vivo* 3D-US vessel representations showed geometries similar to those obtained with the clinical CTA gold standard. The *in vitro* investigation revealed that 3D-US reconstructed surfaces had a mean difference from CTA of less than a mm (0.55 mm); *in vivo* a larger mean difference of 1.82 mm was noted. Larger errors noted at the extremities exist because of differences in length between 3D representations. Although comparable B-mode (or color Doppler) versus CTA results were obtained, the reliability of computed tomography can be discussed since the true gold standard CAD file was available *in vitro*. CTA overestimated the true vessel size (surface area of 2073 versus 2016 mm^2 for CAD, Table 9; also see Fig. 5.5b). This can be explained by the MIP and VR algorithms used for outlining the lumen boundary of CTA images and by the smooth filtering applied along the longitudinal axis. With these algorithms, significant loss of details in CTA scans can occur because they use only one gray threshold to identify the lumen vessel. Consequently, the CTA post-processing techniques are user-dependent [206]. In addition, the resolution of CTA limits delineating arteries that are less than 1.2 mm [207]. Because the *in vitro* phantom had stenoses with diameters within this range (1.2-1.4 mm), even with contrast agent, a loss of details and an overestimation of the lumen surface were expected. Regarding 3D-US assessment versus CAD, our findings demonstrated an error of 1.13 ± 0.56 mm (Fig. 5.4b, range of 0.06 to 7.1 mm). Reported errors are explained by the surface reconstruction procedure of the robotic system explained further in [202].

Some factors can be identified regarding the performance of the 3D-US imaging robotic system when comparisons are made either with 3D CTA or CAD mappings. Already, there are considerable differences observed between B-mode representations and CTA *in vitro* (Fig. 5.4 and 5.5) and *in vivo* (Fig. 5.7 and 5.8): the B-mode representation was closer to CTA *in vitro* than *in vivo*. While different segmentation method was used for both CTA scans, it is important to note that the most significant challenge faced with *in vivo* images was to identify the vessel lumen from surrounding tissue and exclude vascular calcifications. Thus, errors in segmentation could have been introduced into the *in vivo*

CTA representation. Regarding 3D-US, discrepancies with CTA could results from image resolution, number of image samples along the *x*-axis (longitudinal axis), segmentation of the vessel lumen, and 3D calibration precision of the robotic system. Also, contrary to CTA representations that were smoothed along the longitudinal axis, our 3D-US mappings were presented by juxtaposing raw *x*, *y*, *z* segmentation points of each cross-sectional image (e.g., see Fig. 5.5a and Fig. 5.8a and b). Altogether, these errors were found, in a previous study, to contribute to up to 0.40 mm in surface points reconstruction and are thoroughly discussed in [202]. Other sources of errors could reside in the fabrication process of the vascular phantom with reported errors up to 5.7% in diameter compared to the CAD file [203]. However, all above mentioned sources of errors do not explain entirely 3D mapping discrepancies with CTA or CAD reconstructions, especially *in vivo* (Fig. 5.8).

An additional challenge *in vivo* was the presence of calcium within the artery wall producing severe acoustic shadowing and preventing the vessel lumen from being adequately visualized along its length, thus resulting in unusable data for the 3D-US reconstruction. Because color Doppler uses blood flow velocity signals, it could map the arterial lumen better than in B-mode. However, it tended to map the vessel lumen outside its true boundary because of the sensitivity of this method to the gain setting [30]. Thus, in this mode, the segmentation of the vessel lumen was larger, as observed in Fig. 5.8c.

Note that *in vivo*, the same calibration transform sources of errors (i.e., Z-phantom calibration, section 5.4.2.2) were faced as *in vitro*, except that the location of the calibration phantom into the robot workspace was found to have an effect on the 3D vessel dimensions and geometry. The Z-phantom calibration was configured to reconstruct accurately a small scanning distance of 90 mm into the robot space. *In vitro*, the position of the Z-phantom and that of the scanned vascular phantom coincided, as in [202], whereas *in vivo* the Z-phantom was approximately located within the robot workspace. Indeed, the patient's leg was first scanned, markers were indicated on the scanning bed and then the Z-phantom was positioned approximately at the location of the middle segment of the femoral artery, depicted in Fig. 5.6a. That explains why only the middle segment of the femoral artery was reconstructed and compared to CTA. For future works, two solutions are envisaged: either

designing a longer Z-phantom matching the length of a typical human leg (with markers on the scanning bed to properly position the leg), or repeating calibrations by moving the current Z-phantom at different locations on the scanning bed. In addition, because patient motion was not monitored in this study, changes in the leg position during acquisition might also have contributed to geometric distortions. The robot tags positions in US images and assumes the vessel to be static between the freehand teach and automated scanning modes. In addition, with movement during scanning, *x*, *y*, *z* image positions might be relayed with delay thus incorrectly registering the actual location of the US image in the robot referential. Of course, this preliminary *in vivo* result is not enough to characterize the 3D-US imaging robotic system, but holds great promise for future clinical perspectives.

5.6.2 Analyses of localization and quantification of stenoses

Severe *in vitro* stenoses were detected, localized and quantified (see Fig. 5.5 and Table 10). Compared to CTA, the lumen areas of *S1* and *S2* were underestimated by less than 4.1%. The difference was much larger with CAD file representations (see Table 10), where stenoses were generally undervalued by up to 11.8%. The difference in stenosis quantification was mostly due to the poor assessment of the non-diseased vessel segment, where dimensions (in area) were larger with CTA compared to the CAD file and 3D-US representations (Table 9 & Fig. 5.5). Also, *S2* was more accurately quantified than *S1* probably because in the fabrication of the vascular phantom this segment was more congruent to the CAD file (Fig. 5.5). In Table 12, lengths of stenoses in 3D-US and CTA representations had errors of similar magnitude with the CAD file (<3.5 mm). *In vivo*, detection and quantification of stenoses on 3D-US vessel representations (both B-mode and Doppler) were more difficult because vessel axes did not perfectly overlap with CTA (Fig. 5.7). It is to note severe stenoses were not easily identifiable as well on the CTA representation. Moderate in vivo stenoses were quantified on 3D-US vessel representations up to 89.8% in B-mode and up to 78.6 % in Doppler (see Fig. 5.8 zones [-40, 0] and [0,20]mm) (the CTA was quantified up to 39.0 % in Fig. 5.8 zones [-60,-40] and [-20,20]mm). This was mostly attributed to differences in the non-diseased geometry segment of 3D-US vessel representations. Because the true vessel area is unknown *in vivo*

and because only 1 subject was used, it is premature to conclude on the capability of the robotic scanning system to quantify stenoses in patients.

5.6.3 Comparison to the literature

5.6.3.1 Analyses of 3D vessel representations

Reconstruction of an *in vitro,* realistic vessel segment (89.4 mm length) was achieved reliably with the 3D-US robotic imaging system compared to CTA. A mean surface-reconstructed error of 0.55 mm, which translates across its length as 0.65% variability (% of surface-reconstructed error/length) was reported, and a mean lumen cross-sectional error of -6.4 ± 9.8 mm^2 with respect to CTA was found. *In vivo*, the middle segment of a lower limb artery imaged in CTA was reconstructed with US (136.6 mm length). This portion was biased with a mean point surface error of 1.82 mm in B-mode that translates across its length into 1.34% variability (% of surface-reconstructed error/length), and a mean lumen cross-sectional area error of 13.4 ± 11.1 mm^2. The same analyses were doubled in value for the color Doppler representation. In the literature, it is difficult to compare our results to other 3D-US studies using electromagnetic freehand tracking because they have not evaluated the accuracy of their system and focused mainly on demonstrating their technology's potential to monitor pathological changes in reconstructed vessels during a fixed period. For example, in a carotid study, 4 asymptomatic subjects with almost non-existent atherosclerosis plaque were used to evaluate the reproducibility of a freehand system to assess the vessel lumen volume [100]. The carotid artery lumen volume had 5% (cm^3) reproducibility but only a 1-cm segment of its bifurcation was analyzed. In a vein graft investigation, the cross-sectional lumen area was monitored at affected sites (e.g., valves and diffused intimal hyperplasia) [196] where in 10 patients, the reproducibility was 6.9% (2.5 mm^2) for lengths ranging from 16 to 75 mm. Other studies examining the carotid artery evaluated the reproducibility to 1.4% rms precision *in vitro* with phantoms that consisted of water-filled balloons, and showed the reconstruction of 2 *in vivo* pathological geometries without performing any analyses [192]. Another study validated their reproducibility with anthropomorphic pulsatile phantoms of the carotid bifurcation of approximately 40 mm in length [99]. Errors in cross-sectional areas were up to -6.5%

(-1.5 mm^2) and their lumen volume up to -5.5% (-89.9 mm^3). The applicability of this system was tested *in vivo* on 4 pathological patients with no image reference for analyses.

All these methods seem promising to reproduce results with high fidelity in vessel segments. Our data have also shown comparable reproducibility for vessel reconstruction *in vitro* and *in vivo* across its length. However, we have also demonstrated the accuracy of vessel representations *in vitro* and compared our *in vivo* results to a reference model produced by another clinical imaging modality. As we have reported, solely assessing reproducibility does not verify accuracy in reconstructing the entire vessel geometry. This measure just demonstrates stability of the system in reproducing the same 3D representation. This sort of assessment is usually biased because the environment is controlled and does not represent the clinical context. In our study, we have shown the potential to accurately represent lower limb arteries *in vitro* with a realistic vessel geometry by surface-reconstruction analyses and cross-sectional area measurements. We have investigated these geometries with CTA, a clinical diagnosis tool with the highest standard of accuracy, and assessed errors with the CAD file representing the geometry of the lumen. The feasibility of producing a 3D vessel representation of a lower limb superficial femoral artery with stenoses *in vivo* was also tested by emulating, at best, the clinical context. The 3D-US imaging robotic system to detect, localize and quantify lower limb arterial stenoses was presented in full scope in a manner that identifies clinical benefits and pitfalls, and further developments required to enhance the clinical application.

5.6.3.2 Analyses of localization and quantification of stenoses

Stenoses in this study were detected and quantified in terms of area reduction and in lengths. *In vitro,* stenoses up to 98.3% (corresponding approximately to 82% in diameter) were detected with errors <4.1% with respect to CTA (<11.8% error compared to the CAD file). In the literature, only a few *in vitro* studies performed with an electromagnetic tracking device had similar objectives. In a saphenous vein bypass graft study, stenoses up to 58.0% in diameter reduction were detected with <-1.4 mm accuracy [102]. Using a similar tracking device, another study assessed *in vitro* stenoses up to 70.0% in diameter reduction at the bifurcation site of the carotid artery with <3.0% error; *in vivo* stenoses up to 74.0% in diameter reduction were also detected with no gold standard reference [99].

This method quite accurate *in vitro* was restricted to this small arterial segment, however since no other clinical imaging modality was used to verify the *in vivo* results, only the potential of the technology can be claimed.

Because there is no true reference standard for vessels *in vivo*, clinical investigations are often conducted in multimodal comparison. In our work, we evaluated *in vitro* and *in vivo* data with CTA. This clinical diagnosis tool is known to accurately detect the presence of stenoses in more than 90% of small and moderate-sized arteries, but sometimes overestimates the degree of stenosis in heavily-calcified arteries [26]. Our 3D-US system had difficulty detecting and localizing severe stenoses in the middle segment of the patient`s femoral artery because the geometry was distorted and data was missing. The calcified artery was the cause of this problem because strong shadow was observed on US images and the lumen was often unidentifiable. It is important to remember for this same segment, severe stenoses could not be identified on the CTA vessel representation for the same reason. Still, comparison of our study with others is not appropriate, especially when stenosis grading is highly dependent on the examination method and post-processing technique [194]. Improvements in stenosis quantification may be achieved *in vivo* by using image compounding because acquiring different US views may improve the signal to noise ratio of images.

Limitations of the robotic arm also include its inflexibility to cover certain areas of the patient's lower limb for the acquisition of cross-sectional US images. It would currently not be possible with 1 full scan to cover the entire vascular tree from the iliac to the tibial vessels without constraints from the robot's safety controls and architecture [148]. To improve the patient's lower limb workspace and to comply with safety issues, it would be necessary to improve the robot's kinematics design. A new medical robot architecture, specially designed for this application with strong compliance to safety concerns is currently in development by our group [208]. Moreover, to enable detection of stenoses at the same location compared to CTA, an improvement of the procedure should be incorporated to keep the limb static, with the design of a holder that could monitor changes in position with embedded sensors to correct for movements.

5.7 Conclusion

The 3D-US imaging robotic system was validated *in vitro* with a short, realistic vascular phantom. The 3D-US reconstructions obtained were analyzed for geometry and quantification of stenoses. Their standards were compared to CTA and their errors compared to the CAD file of the phantom lumen geometry. We also verified the feasibility of this system *in vivo* and compared the 3D reconstruction with CTA imaging. The results showed promise in detecting stenoses on a portion of a long vessel (i.e., femoral artery) of a pathological patient. Of course, further developments are necessary to ensure the complete representation of lower limb vessels. The use of a new robot architecture that incorporates safety guidelines and arm lengths with kinematics design to cover the whole leg surface is in process [208]. The design of a new Z-phantom calibration device may also be necessary to scan long vessels accurately. In the future, comparative analyses could adopt multiple imaging modalities, including duplex US (i.e., anatomy and blood flow), to situate the accuracy level of our 3D-US robotic imaging system for quantifying stenoses with spatially-registered Doppler spectral waveforms [104]. In addition, a clinical study with more patients could validate application in the medical context by following lower limb vessel pathology over a fixed period of time, evaluating their therapy and monitoring plaque progression [196].

Acknowledgments

This work was supported in part by the Canadian Institutes of Health Research (CIHR) under grant MOP #53244. Dr. Soulez is the recipient of a National Scientist award of the Fonds de la Recherche en Santé du Québec. Ms. Janvier was the recipient of studentship awards from the Fonds de la Recherche sur la Nature et les Technologies du Québec, TD Canada Trust, the Institute of Biomedical Engineering at the Université de Montréal, the Quebec Black Medical Association and the End of Study Grant from the Faculty of Graduate and Postgraduate Studies at the Université de Montréal. The authors are grateful to Dr. Claude Kauffmann, Ms. Zhao Qin, Mr. Boris Chayer, Dr. Marianne Fenech, Dr. Marie-Hélène Roy Cardinal and Dr François Destrempes for discussion and technical supports. The authors are also grateful to Mr. Ovid M. Da Silva for manuscript editing.

Chapter 6

Discussion

Making your mark on the world is hard. If it were easy, everybody would do it. But it's not. It takes patience, it takes commitment, and it comes with plenty of failure along the way. The real test is not whether you avoid this failure, because you won't. It's whether you let it harden or shame you into inaction, or whether you learn from it; whether you choose to persevere.

Barack Obama

6.1 Summary and original contributions

The goal of this thesis was to validate and optimize a prototype medical 3D-US imaging robotic system to localize and quantify arterial stenoses in lower limbs. Three research objectives were targeted by this project and their achievement contributed to a combination of publications. The first paper presented the performance of our medical robotic 3D-US imaging system, the second paper demonstrated validity and accuracy of 3D reconstructions *in vitro* on a mimicked femoral artery and the last paper showed its feasibility to localize and quantify lower limb arterial stenoses *in vitro* and *in vivo*. The conclusions drawn from this research project provide a clear analysis on the performance and limitation of our system for an eventual clinical application. The calibration and geometric evaluations of 3D vessel representations were the general theme discussed in this project.

6.1.1 Calibration

The cornerstone of any 3D-US imaging system is its performance in navigation, compatibility and performance in a clinical environment [71]. Considering the technical specifications of our medical robot, there is a real potential to generate accurate 3D reformations (i.e., reconstructions) with high repeatability, positioning accuracy, precision and improved clinical decision. However, the efficiency of the robot relies on the accuracy of the 3D data. A calibration method was required to integrate kinematic links and US images into the robot's frame of reference, and also to compare CAD and CTA models to the corresponding 3D vessel representations.

6.1.1.1 Robot kinematic calibration

Robot kinematics are determined by the length of the links and the angulation of each joint of the robotic arm to perform accurately in its workspace. Normally, the end-effector, the last component of the robotic arm, is tracked and kinematic parameters are identified by measuring several robot's joint configurations [209]. The robotic literature, the sources of end-effector positioning errors are largely due to geometric and elastic structural deformations that occur in the robotic arm [167, 210-212]. The precision of 3D navigation systems can change during the course of experimentation if there is any variation in the direction of the target of interest [71, 112]. To overcome this limitation, validation techniques are usually performed repeatedly with a stylus to assess precision and positioning accuracy for the clinical application under investigation [112, 160, 162, 185, 213].

In chapter 3, we evaluated the performance of our medical robotic imaging system by combining calibration kinematic principles in comparison with standard 3D-US freehand tracking validation techniques. A rigid pointer was incorporated into the robotic arm to extend the robotic point targets into a lower limb mimicking phantom. Point target precision was ≤ 0.57 mm, the positioning accuracy was ≤ 0.75 mm and the inter-target accuracy was ≤ 0.48 mm in the 5 designated zones of the robot workspace for both 'teach' and 'replay' modes. These results were comparable to the literature where point-target precision varies between 0.61 mm and 1.7 mm and inter-target accuracies vary between

0.05 mm and 1.7 mm for EM devices [85, 160, 161, 185]. In lower limb arterial vessel segments, differences as low as ≤ 0.20 mm were found in zones close or remote to the robotics' arm base. Hence, the robotic arm is appropriate for our clinical application. The creation of a map of optimum zones in the robot workspace was helpful to characterize and improve the system's performance. In robotics, this contribution is paramount to optimize robot limb lengths, improve accuracy and predict its performance for investigating lower limb vessels. Also, to our knowledge, this characterizing process provided for the first time a rigorous method of evaluating a 3D-US medical robot with competitive performance to other common 3D-US freehand tracking systems used for similar clinical applications. Nevertheless, it is important to note that the performance of the robot could be improved in the order of microns using sophisticated metrology equipment such as laser tracker (volumetric accuracy of 20 microns), a linear interferometer system (accuracy of 1 micron), a measurement arm (volumetric accuracy of 18 microns) and a telescopic ballbar.

6.1.1.2 US image calibration

Appropriate location of US images in the robot coordinate system is another form of calibration necessary to allow every 2D-US image to be registered correctly according to their position and orientation with respect to the patient anatomy [71]. This additional calibration step is mandatory in 3D-US freehand tracking systems to compute the transformation (rotation, translation and scaling) between the tracking sensor mounted on the probe and the image plane itself. This registration should provide a spatial relationship between the native 2D frames to reconstruct accurately a 3D geometry. However, the calibration problem is still challenging because much variability is introduced from noise in the 3D position localizers and the limits imposed from US image resolution. These issues have been addressed extensively in the literature mostly with 3D-US freehand systems as summarized in [71]. Solutions to minimize variability focused mainly in the conception of calibration phantoms and identification of features on the US images that can also be located in the tracking coordinate system. While the concept of calibration itself is relevant for robotic systems, much of the techniques used the freehand approach. In the freehand method, human operators are not capable of executing exact trajectories with high precision and good reproducibility [214]. Most approaches in the literature have neglected the impact

of the probe movements on the calibration transform. It is well known that tracking accuracy directly determines the accuracy and precision of 3D geometry and the visual perception of the model. All tracking devices used in freehand systems record the position and orientation (pose) of the sensor on the probe, not the US image plane itself [71].

A similar challenge was faced with our robotic system with the US probe now attached to a handle of the end-effector. In chapter 3, we first used a classical cross-wire phantom [160] to determine the calibration transform. We achieved a precision of 2.5 mm to locate the point target repeatability. While the accuracy of the calibration transform could not be measured directly, we evaluated its apparent performance visually on 3D reconstruction of the vascular phantom. We observed a shift along the reconstructed vessel longitudinal axis. In chapter 4, we improved our method by using a more robust calibration technique with a Z-phantom conceptualized for our robotic system. We evaluated the effect of US imaging parameter settings on the performance of a 3D reconstruction of a vessel. This was possible because the robot could repeatedly execute the same trajectory for all specified settings with high precision and accuracy. For different US image parameter settings (i.e., 4 image depths, 3 focus image depths and 3 image zooming), we found a precision between 0.47 mm and 1.2 mm and an accuracy between 0.40 mm to 1.74 mm. The characterization of the system provided an optimum setting to represent accurately a lower limb mimicking artery and this quantification could be used to either compensate or to predict the calibration performance in other US image settings. Other studies using different 3D-US freehand systems (i.e., optics and electromagnetics) evaluated design efficiency, performance of distinct US probes or alternate calibration methods with a calibration with the Z-phantom [179-181, 215]. In the 3D-US calibration literature, it is well known that a rigorous protocol is necessary to acquire calibration data. Ideally, the acquisition protocol should be organized into predefined settings in translation, rotation and relative position between the tracking system, phantom and probe in order to select a calibration transform for each US image data set [178]. In addition, the correctness of the probe calibration should be verified immediately with 2D and 3D quality measurements [187]. In that matter, precision was found more sensitive to calibration errors than accuracy because it only processes the variations caused by spatial calibration parameters as opposed

to combining other sources of errors [177]. For all the reasons listed above we decided to use a Z-phantom to calibrate our robot and evaluate our 3D vessel representation.

6.1.1.3 Image registration

Image registration was a necessary step required to validate the accuracy and precision of our reconstructed 3D vessels. This form of calibration method aligns the position and orientation of two different 3D representations enabling an objective comparison of these reformations. This technique is very common in augmented reality, where virtual objects and users need to merge into the same environment. In that matter, the scope of challenges is broader because of the lack of accurate wide-area sensors to track in real-time objects' locations and orientations [114, 115]. In medical robotics, the potential to augment clinician's ability to perform image guided therapy with an improved precision and accuracy with CT, US or fluoroscopic images have been explored [157, 216-218]. In this case, pre-operative and per-operative patient imaging or localization are performed followed by a process of image registration that establishes the spatial relationship between images of the patient's and the actual patient.

A major issue in medical robotics and 3D-US freehand systems is to ensure that the robot positioning is accurate because this will impact precision of the guidance and eventually the outcome of the intervention [157, 160, 162, 213]. Generally, this measure is difficult to assess in clinical setting due to the lack of fixed and well-defined landmarks inside the patient [108]. Normally, precisely built phantoms are used to assess the overall system's accuracy. In our study, we used a vascular phantom to validate our 3D-US reconstructed vessel geometry. In chapter 4, the reference standard *in vitro* came from a mathematical model in [219] and, in chapter 5, from a realistic model of stenosed vessel embedded in a phantom [203] and in vivo 3D vessel representations from clinical CTA images. Registration techniques discussed in chapters 4 and 5 were used to match our 3D-US vessel reconstruction to these reference models. In chapter 4, this form of validation allowed to detect and quantify distortions in vessel shape. In case of poor 3D reconstructions, an elliptical geometry was identified whereas the best robotic reconstructions were very close to the reference model. The differences in the 3D

representations could easily be linked with the accuracy of the calibration transform because the method of 3D reconstruction was the same for all acquired data. In chapter 5, multi-mode image comparisons of vessel representations were made available *in vitro* with our 3D-US system, the CTA and the CAD mould because of an image registration algorithm which allows features to be matched directly. Moreover, a feasibility evaluation *in vivo* was realized with our 3D-US system and the CTA vessel representation could be used as reference. Thus, from these evaluations a strong validation of our 3D-US system was obtained for the localization, detection and quantification of stenoses in lower limb vessels.

6.1.2 Geometric evaluations of 3D vessel representations

3D-US systems are developed to perform volumic acquisitions that could be used in a clinical setting instead of more expensive or invasive imaging modalities such as MRA and CTA. They are usually evaluated on the quality of 3D representations they produced [192]. Repetitive volumic evaluation of an object with a balloon shape embedded in a phantom is often used to evaluate the accuracy of length and different 1D, 2D and 3D measurements taken from 3D US acquisitions [187, 192]. Accurate volume estimation required the use of small inter-slice distances, however, distances less than the elevation resolution do not result in increased accuracy [77]. In a clinical setting, benefits of 3D volume measurements were reported to quantify prostatic lesions and carotid atherosclerosis plaque volumes [77, 91, 220]. A good reproducibility of the volume quantification is required to be clinically useful. Errors of volume measurement can result from compensatory random errors in locating the points defining the volume [160]. Cross-sectional area measurements are also used in clinic to analyse the progression of stenotic lesions in a vessel. The reproducibility of cross-sectional area measurements can improve the confidence in the 3D representation method especially in case of vessel sinuosity where 2D measurement can be erroneous [103, 190].

In chapters 4 and 5, we evaluated the adequacy of our 3D vessel representation not only in repeatability but also in accuracy. Matching our 3D representations to a reference standard allowed us to evaluate the reconstruction accuracy in distance and the cross-

sectional area errors. Iterative measurements allowed us to establish the repeatability of our system.

In chapter 4, the accuracy of our 3D-US reconstruction in distance ranged between 0.40 – 1.74 mm and the comparison of cross-sectional areas at optimum setting had a good fidelity in representing the shape of the vascular phantom.

In chapter 5, mean length estimation of 3D-US reconstruction and cross-sectional area analyses *in vitro* were found to be underestimated with respect to the CTA (0.03 – 3.6 mm) and overestimated compared with the CAD file (0.06 – 3.6 mm). *In vivo*, mean length estimation of 3D-US reconstruction and cross-sectional areas were overestimated compared to the CTA in B-mode and in Doppler. The differences of the results obtained *in vitro* and *in vivo* can be explained principally by some factors such as the calibration parameters for a long length vessel, the calcification in arteries, and the movement of the patient leg. These factors are not controlled *in vivo*.

Stenoses evaluated from these geometries were quantified *in vitro* in chapter 3, on a vascular phantom with double stenoses of 75.0 % and 80.0 % area reductions. Stenosis quantification errors from 3D-US reconstruction were estimated at -0.9 % and 3.0 %, respectively.

In chapter 5, severe stenoses up to 97.3 % (area reduction) *in vitro* were quantified with ≤ -11.8 % error (4.1% error when compared to the CTA). Stenoses *in vivo* were not easily identifiable in B-mode, color doppler and the CTA because of calcified arteries. This resulted in distortions overall the 3D vessel representations. Also, in US reformations not all the sections of the lower limb vessel were reconstructed. Other groups that have used similar methods to evaluate the accuracy of their 3D reconstructed geometry in vascular application have not characterized the performance of the system both *in-vivo* and *in-vitro* with error estimation of the length and shape of the reformation and its impact on stenosis quantification. Either they used phantoms or balloons [71, 192, 221, 222], animals [223] and cadaver organs [222]. Even if they have performed *in vitro* and *in vivo* 3D-US reconstruction of arteries [99, 102], their analyses were not in depth to identify the advantages and limitations of their system for the clinical application.

6.2 Future research

6.2.1 New robotic design

To counter the current limitations of our present 3D-US robotic imaging system, a new prototype parallel robot has been specifically designed to enable 3D US scanning of lower limb vessels [208]. This new robot architecture offers a larger workspace to cover the patient's leg anatomy. Moreover, the safety of the system is improved because it is made with parallel arms which a tool holder is attached to carry the US probe (see Fig. 6.1). Also, real-time visual servoing and force control are planned to be incorporated with this robot, where the clinician could place manually the starting position for scanning on the artery with the desired applied force, and the robot could track the center of the vessel accordingly. This system shared control approach has already been proposed by the research group at the University of British Columbia [146], except that the system is tele-operated by the operator with a mouse or joystick for this last prototype. While this scanning method is restricted to straight lines, it could be improved to handle more complex shaped objects in its control features such as in [224].

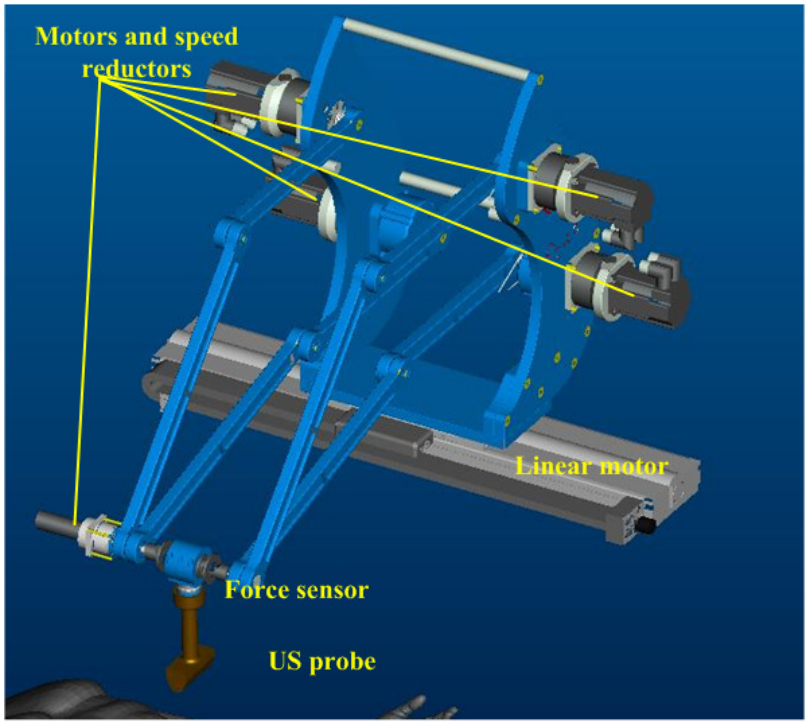

Figure 6.1: New parallel robot architecture for 3D-US medical imaging.

Adaptive visual servoing is also a method that could be used to control the US probe for an optimum procedure to determine the best spatial calibration parameters [225]. This technique could be adapted with our Z-phantom method and the new robot design to provide an automatic calibration [225]. Robust segmentation methods such as the fast marching algorithm [41] could also be incorporated to provide in real-time the lumen boundary, where the center of gravity of the vessel could be more adequately determined. Subsequently, multiple artery tracking could be integrated for a more complete representation of the lower limb arterial vascular tree. Of course, a force feedback control loop similar to [140] need to be implemented in order to apply appropriate forces on the US probe.

Since we are using a teaching approach, our present 3D-US robotic system also repeats the force exerted by the operator. However, it will not change the Cartesian position to adjust the force error. This function will be added to our new design. In addition, since the scan is a high interactive process, the force control feedback should be controlled by the clinician or operator to enable correction if necessary.

While the new robot architecture was designed mechanically for safety, all phases of the robot must be tested before clinical implementation. Software and electrical safety are important aspect to consider in the operation of the device. Verification and validation of this safe medical robot with innovative software is going to be crucial in order to integrate the operation of this new technology for the clinical application [226]. Basic principles include: redundancy in safety controls s, speed and power controls in actuators; rigorous design analysis, documentation, and testing protocols; multiple emergency stop and checkpoint/restart facilities; etc [218]. After considering all safety issues, another validation will be required to characterize the precision and accuracy of this new robot architecture, as done in this thesis.

To solve the leg motion problem many strategies may be proposed for the new robot architecture because simply tying the leg will not prevent all motion artefacts. Furthermore, a method to track displacement of the leg is needed. An external tracking device that monitors the leg motion is the first approach suggested. Using a magneto-optic hybrid tracker, a technology very common in augmented reality visualization, the leg movements can be monitored and the robot's path can be adjusted to this reference for navigation [113, 115-117, 227]. Of course this procedure would require an additional calibration step of the two systems for registration. Another alternative is to use camera sensors [228, 229], shape tape (i.e., a motion capture sensor) [179], or even a combination of accelerometers and gyroscopes [230] to construct a virtual representation of the lower limb to track its movement in real-time. These are all well known orthopaedic devices that are used to capture human motion for monitoring the physical activity of lower limbs and evaluating their performance. Perhaps combining human locomotion principles to our new robotic design could be applied to correct leg motion.

6.2.2 3D Image processing

Many sources of errors and artefacts encountered in our study were a result of the image processing algorithms applied to our data [70, 75]. Improvements in the 3D-US reconstruction techniques can be provided to include a voxel-based (volume) reconstruction with our feature-based (surface contour) method. This preservation of original data (2D

image planes) extended into a 3D grid volume could allow new information surrounding the anatomy of the vessel to be explored. Thus, a variety of rendering techniques could be applied to the image volume for repetitive review. Moreover, a class of options in segmentation and rendering algorithms for volume or surface operations could be made available for the same 3D volume data [70, 75]. These methods could be facilitated through computer aided software where a user interface is developed to allow clinicians to control the viewing of the 3D reconstructed image. This interaction should preferably be in real-time for a visual effective management of the lower limb vessel examination. Stradx (University of Cambridge, Cambridge, UK), a real-time acquisition and visualization software, has been developed for freehand 3D-US devices [66, 95]. This software does not construct a voxel array but exploits arbitrary slices directly from the raw B-scans for viewing. Perhaps, an integration of this software to our new robot architecture could be performed for a real-time 3D viewing of lower limb vessels.

For the robot design reported in this thesis, centering the vessel manually (teach mode) presented a challenge *in vivo*. Much artefacts were observed in the vessel reformations. In the robotic literature, a number of motion tracking algorithms have been implemented to evaluate the feasibility of US image servoing in centering the vessel. These approaches discussed in [146] are feature-based algorithms such as the star and discrete snakes where the vessel boundary is sought on US images. The extracted information is then used to control motion of the robotic arm. The feasibility is determined by the US image Jacobian which relates differential changes in image features to differential changes in the end effector location. Thus, controling the motion of the US transducer to the center of the vessel is possible with this option and could be added in our new design. To improve these algorithms and control of the robotic arm as well as optimum settings of the US image, image servoing with RF images could also be used.

Nevertheless, other sources of errors and artefacts may still occur in 3D-US imaging regardless of the image processing techniques applied [231]. 3D spatial compounding of US scans is an approach that could be used to improve the quality of US images. This method constructs an improved image from the combination of several different angles from the same cross-sectional plane. The acoustic shadows caused by calcified arteries and

speckle noise therefore could be reduced in the US images. This procedure has already shown potential with an articulated scan arm and a freehand system [165, 232]. Thus, our new robot architecture could incorporate this process by having multiple scans of the artery of interest viewed at different angles. Another strategy would be to use RF data with hardware and software developments in our new robot design that support this mode. This would allow direct processing of the US images from its raw data and extract precise information without image artifacts.

6.2.3 Clinical benefits

Many clinical benefits could be gained from a 3D-US robotic imaging system to detect stenoses located in lower limb vessel arteries and to provide the clinician with an arterial or venous mapping without ionizing radiation or the use of expensive technologies such as MRI. After this technology has been completely validated and optimized, it can also qualify for image-guided therapy applications such as vessel puncture, guidance of angioplasty or stenting procedure [233]. After peripheral revascularization or bypass surgery, repetitive imaging follow-up is necessary to evaluate the remodeling of vein grafts and the effectiveness of balloon angioplasty and stents on patients over several years [52, 103, 190, 195]. For these situations mentioned, 2D US imaging is cumbersome and too operator dependent, thus a 3D US B-mode and Doppler mapping can be a good alternative for these patients. Other benefits of this technology could be to quantify plaque and stenosis in lower limb vessel arteries in order to monitor the disease progression in patients under medical treatment [89, 90, 92, 220]. Computational flow models could also be achieved in lower limb vessels to assess the wall shear stress and localize the development of atherosclerotic plaques [98, 198]. Another approach with the new robotic system could be to study elastrography of the arteries by applying compressions to vessel and measure their rigidity. This method of analysis has already proven great potential for the carotid artery and the deep venous thrombosis detection [168, 169]. Evaluating stenosis in Doppler mode with spatially-registered spectral waveform in 3D is also another possibility with our system. Sample volumes of Doppler waveform registered in 3D space with a surface reconstruction of the lumen vessel in color Doppler are possible [101, 104]. Finally, with all the benefits available with the system, the best option would be to perform a clinical

study with a large patient data base to locate and quantify arterial stenoses in lower limb vessels and compare them to CTA or MRA for evaluating the impact of this approach on patient management.

6.3 Conclusion

This study confirmed that our new prototype medical 3D-US imaging robotic system technology is able to locate and quantify lower limb arterial stenoses for diagnosis, therapy planning and monitoring. Principally, this new technology can provide an accurate 3D model of a lower limb artery, with a potential for accurate mapping and quantification of arterial stenoses *in vitro* but a need for improvement *in vivo*. Its evaluation with CTA has shown that this approach is feasible and has a potential to give high diagnostic accuracy in a clinical setting if several improvements are made on robotic interface and image processing. In regards to the clinical application, 3D reformation of the vessel where stenoses can be located and quantified accurately in any projection was generated at low-cost and non-invasively. Finally, this study has provided the proof of concept that 3D-US imaging robotic system can manage optimally lower limb stenoses.

Bibliography

[1] "Causes of Death," in *Canada Health*, 2004 (report).

[2] "Economic Burden of Illness in Canada," in *P. H. A. O. Canada*, 1998 (report).

[3] P. Poredos, and B. Jug, "The prevalence of peripheral arterial disease in high risk subjects and coronary or cerebrovascular patients," *Angiology,* vol. 58, no. 3, pp. 309-315, Jun-Jul 2007.

[4] J. A. Berliner, M. Navab, A. M. Fogelman, J. S. Frank, L. L. Demer, P. A. Edwards, A. D. Watson, and A. J. Lusis, "Atherosclerosis: basic mechanisms. Oxidation, inflammation, and genetics," *Circulation,* vol. 91, no. 9, pp. 2488-2496, May 1995.

[5] L. M. Khachigian, *High-risk Atherosclerotic Plaques*, New York: CRC Press, 2005.

[6] J. R. Bartholomew, and J. W. Olin, "Pathophysiology of peripheral arterial disease and risk factors for its development," *Cleve Clin J Med,* vol. 73, pp. S8-14, Oct 2006.

[7] K. Watson, B. D. Watson, and K. S. Pater, "Peripheral arterial disease: a review of disease awareness and management," *Am J Geriatr Pharmacother,* vol. 4, pp. 365-379, Dec 2006.

[8] A. V. Meru, S. Mittra, B. Thyagarajan, and A. Chugh, "Intermittent claudication: an overview," *Atherosclerosis,* vol. 187, pp. 221-237, Aug 2006.

[9] H. C. Stary, *Atlas of Atheroclerosis Progression and Regression*, 2nd ed. London: Richmond House, 2004.

[10] E. S. Bartlett, T. D. Walters, S. P. Symons, and A. J. Fox, "Carotid stenosis index revisited with direct CT angiography measurement of carotid arteries to quantify carotid stenosis," *Stroke,* vol. 38, pp. 286-291, Feb 2007.

[11] I. N. Staikov, M. Arnold, H. P. Mattle, L. Remonda, M. Sturzenegger, R. W. Baumgartner, and G. Schroth, "Comparison of the ECST, CC, and NASCET grading methods and ultrasound for assessing carotid stenosis. European Carotid Surgery Trial. North American Symptomatic Carotid Endarterectomy Trial," *J Neurol,* vol. 247, pp. 681-686, Sep 2000.

[12] M. H. Heijenbrok-Kal, M. C. Kock, and M. G. Hunink, "Lower extremity arterial disease: multidetector CT angiography meta-analysis," *Radiology,* vol. 245, pp. 433-439, Nov 2007.

[13] N. A. Khan, S. A. Rahim, S. S. Anand, D. L. Simel, and A. Panju, "Does the clinical examination predict lower extremity peripheral arterial disease?," *JAMA,* vol. 295, pp. 536-546, Feb 2006.

[14] T. R. Harrison, and D. L. Kasper, *Harrison, principes de médecine interne,* Paris, 2006.

[15] I. D. Moussa, M. R. Jaff, R. Mehran, W. Gray, G. Dangas, Z. Lazic, and J. W. Moses, "Prevalence and prediction of previously unrecognized peripheral arterial disease in patients with coronary artery disease: the Peripheral Arterial Disease in Interventional Patients Study," *Catheter Cardiovasc Interv,* vol. 73, pp. 719-724, May 2009.

[16] R. S. Dieter, J. Tomasson, T. Gudjonsson, R. L. Brown, M. Vitcenda, J. Einerson, and P. E. McBride, "Lower extremity peripheral arterial disease in hospitalized patients with coronary artery disease," *Vasc Med,* vol. 8, pp. 233-236, Nov 2003.

[17] P. L. Antignani, "Treatment of chronic peripheral arterial disease," *Curr Vasc Pharmacol,* vol. 1, pp. 205-216, Jun 2003.

[18] L. A. Garcia, "Epidemiology and pathophysiology of lower extremity peripheral arterial disease," *J Endovasc Ther,* vol. 13, pp. II3-9, Feb 2006.

[19] "Diagnosis and management of peripheral arterial disease :A national clinical guideline," in *S.I.G., Network*, 2006 (report).

[20] R. B. Rutherford, J. D. Baker, C. Ernst, K. W. Johnston, J. M. Porter, S. Ahn, and D. N. Jones, "Recommended standards for reports dealing with lower extremity ischemia: revised version," *J Vasc Surg,* vol. 26, pp. 517-538, Sep 1997.

[21] F. A. Schmieder, and A. J. Comerota, "Intermittent claudication: magnitude of the problem, patient evaluation, and therapeutic strategies," *Am J Cardiol,* vol. 87, pp. 3-13, 2001.

[22] S. P. Marso, and W. R. Hiatt, "Peripheral arterial disease in patients with diabetes," *J Am Coll Cardiol,* vol. 47, no. 5, pp. 921-929, Mar 2006.

[23] A. T. Hirsch, M. H. Criqui, D. Treat-Jacobson, J. G. Regensteiner, M. A. Creager, J. W. Olin, S. H. Krook, D. B. Hunninghake, A. J. Comerota, M. E. Walsh, M. M. McDermott, and W. R. Hiatt, "Peripheral arterial disease detection, awareness, and treatment in primary care," *JAMA,* vol. 286, no. 11, pp. 1317-1324, Sep 2001.

[24] H. M. Ismail, K. Jackson, and D. Smith, "Diagnosis and treatment of peripheral arterial disease compared with other atherosclerotic vascular diseases in a university primary care clinic," *J Investig Med,* vol. 54, no. 5, pp. 255-261, Jul 2006.

[25] C. A. Doubeni, R. A. Yood, S. Emani, and J. H. Gurwitz, "Identifying unrecognized peripheral arterial disease among asymptomatic patients in the primary care setting," *Angiology,* vol. 57, pp. 171-180, Mar-Apr 2006.

[26] D. Chan, M. E. Anderson, and B. L. Dolmatch, "Imaging evaluation of lower extremity infrainguinal disease: role of the noninvasive vascular laboratory, computed tomography angiography, and magnetic resonance angiography," *Tech Vasc Interv Radiol,* vol. 13, pp. 11-22, Mar 2010.

[27] J. Golledge, "Lowere-limb arterial disease," *The Lancet,* vol. 350, pp. 1459-1465, Nov 1997.

[28] C. M. Kramer, "Peripheral arterial disease assessment: wall, perfusion, and spectroscopy," *Top Magn Reson Imaging,* vol. 18, pp. 357-369, Oct 2007.

[29] M. Cournot, H. Boccalon, J. P. Cambou, J. Guilloux, D. Taraszkiewicz, H. Hanaire-Broutin, B. Chamontin, M. Galinier, and J. Ferrieres, "Accuracy of the screening physical examination to identify subclinical atherosclerosis and peripheral arterial disease in asymptomatic subjects," *J Vasc Surg,* vol. 46, no. 6, pp. 1215-1221, Dec 2007.

[30] J. T. Bushberg, Seibert, J. A., Leidholt, E. M., Boone, J. M., *The essential Physics of medical imaging*, Philadelphia: Lippincott Wiliams & Wilkins, 2002.

[31] J. P. Lekakis, C. Papamichael, T. G. Papaioannou, K. S. Stamatelopoulos, A. Cimponeriu, A. D. Protogerou, J. Kanakakis, and S. F. Stamatelopoulos, "Intima-media thickness score from carotid and femoral arteries predicts the extent of coronary artery disease: intima-media thickness and CAD," *Int J Cardiovasc Imaging,* vol. 21, pp. 495-501, Oct 2005.

[32] L. E. Chambless, M. M. Zhong, D. Arnett, A. R. Folsom, W. A. Riley, and G. Heiss, "Variability in B-mode ultrasound measurements in the atherosclerosis risk in communities (aric) study," *Ultrasound Med Biol,* vol. 22, pp. 545-554, Jan 1996.

[33] E. S. Bartlett, T. D. Walters, S. P. Symons, and A. J. Fox, "Quantification of carotid stenosis on CT angiography," *AJNR Am J Neuroradiol,* vol. 27, pp. 13-19, Jan 2006.

[34] C. S. Eddleman, H. J. Jeong, M. C. Hurley, S. Zuehlsdorff, G. Dabus, C. G. Getch, H. H. Batjer, B. R. Bendok, and T. J. Carroll, "4D Radial Acquisition Contrast-Enhanced MR Angiography and Intracranial Arteriovenous Malformations. Quickly Approaching Digital Subtraction Angiography," *Stroke*, May 2009.

[35] B. L. Dolmatch, "Imaging peripheral arterial disease: a randomized controlled trial comparing contrast-enhanced MR angiography and multi-detector row CT angiography," *Perspect Vasc Surg Endovasc Ther,* vol. 18, pp. 191-193, Jun 2006.

[36] M. Al-Omran, T. F. Lindsay, J. Major, A. Jawas, L. A. Leiter, and S. Verma, "Perceptions of Canadian vascular surgeons toward pharmacological risk reduction in patients with peripheral arterial disease," *Ann Vasc Surg,* vol. 20, pp. 555-563, Sep 2006.

[37] S. Dellegrottaglie, J. Sanz, F. Macaluso, A. J. Einstein, S. Raman, O. P. Simonetti, and S. Rajagopalan, "Technology Insight: magnetic resonance angiography for the evaluation of patients with peripheral artery disease," *Nat Clin Pract Cardiovasc Med,* vol. 4, pp. 677-687, Dec 2007.

[38] F. U. Grijalba, and M. C. Esandi, "Comparison of gadofosveset-enhanced three-dimensional magnetic resonance angiography with digital subtraction angiography for lower-extremity peripheral arterial occlusive disease," *Acta Radiol,* vol. 51, pp. 284-289, Jan 2010.

[39] J. Mikita, "[Peripheral arterial disease]," *Orv Hetil,* vol. 147, pp. 723-730, Apr 2006.

[40] M. Nylaende, A. Kroese, E. Stranden, B. Morken, G. Sandbaek, A. K. Lindahl, H. Arnesen, and I. Seljeflot, "Markers of vascular inflammation are associated with the extent of atherosclerosis assessed as angiographic score and treadmill walking distances in patients with peripheral arterial occlusive disease," *Vasc Med,* vol. 11, pp. 21-28, Feb 2006.

[41] M. H. Roy-Cardinal, J. Meunier, G. Soulez, R. L. Maurice, E. Therasse, and G. Cloutier, "Intravascular ultrasound image segmentation: a three-dimensional fast-marching method based on gray level distributions," *IEEE Trans Med Imaging,* vol. 25, pp. 590-601, May 2006.

[42] T. W. Rice, and A. B. Lumsden, "Optimal medical management of peripheral arterial disease," *Vasc Endovascular Surg,* vol. 40, pp. 312-327, Aug-Sep 2006.

[43] P. P. Aung, H. G. Maxwell, R. G. Jepson, J. F. Price, and G. C. Leng, "Lipid-lowering for peripheral arterial disease of the lower limb," *Cochrane Database Syst Rev*, pp. CD000123, 2007.

[44] W. S. Aronow, "Peripheral arterial disease," *Geriatrics,* vol. 62, pp. 19-25, Jan 2007.

[45] G. J. Hankey, P. E. Norman, and J. W. Eikelboom, "Medical treatment of peripheral arterial disease," *JAMA,* vol. 295, pp. 547-53, Feb 2006.

[46] A. Stoyioglou, and M. R. Jaff, "Medical treatment of peripheral arterial disease: a comprehensive review," *J Vasc Interv Radiol,* vol. 15, pp. 1197-1207, Nov 2004.

[47] R. G. Crowther, W. L. Spinks, A. S. Leicht, F. Quigley, and J. Golledge, "Lower limb movement variability in patients with peripheral arterial disease," *Clin Biomech,* vol. 23, pp. 1080-1085, Oct 2008.

[48] W. S. Aronow, "Management of peripheral arterial disease of the lower extremities in elderly patients," *J Gerontol A Biol Sci Med Sci,* vol. 59, pp. 172-177, Feb 2004.

[49] F. Violi, and W. Hiatt, "A critical review of antiplatelet treatment in peripheral arterial disease," *Intern Emerg Med,* vol. 2, pp. 84-87, Jun 2007.

[50] C. Bianchi, V. Montalvo, H. W. Ou, V. Bishop, and A. M. Abou-Zamzam, Jr., "Pharmacologic risk factor treatment of peripheral arterial disease is lacking and requires vascular surgeon participation," *Ann Vasc Surg,* vol. 21, pp. 163-166, Mar 2007.

[51] J. I. Weitz, J. Byrne, G. P. Clagett, M. E. Farkouh, J. M. Porter, D. L. Sackett, D. E. Strandness, Jr., and L. M. Taylor, "Diagnosis and treatment of chronic arterial insufficiency of the lower extremities: a critical review," *Circulation,* vol. 94, pp. 3026-3049, 1996.

[52] M. Schillinger, S. Sabeti, C. Loewe, P. Dick, J. Amighi, W. Mlekusch, O. Schlager, M. Cejna, J. Lammer, and E. Minar, "Balloon angioplasty versus implantation of nitinol stents in the superficial femoral artery," *N Engl J Med,* vol. 354, pp. 1879-88, May 2006.

[53] N. Hudorovic, "Detecting the Ademkiewicz artery: is it really necessary in everyday practice?," *Eur J Cardiothorac Surg,* vol. 32, pp. 186-187; Jul 2007.

[54] M. Lecart, M. H. Cardinal, Z. Qin, G. Soulez, and G. Cloutier, "In vitro in-stent restenoses evaluated by 3D ultrasound," *Med Phys,* vol. 36, pp. 513-522, Feb 2009.

[55] E. Regar, P. W. Serruys, C. Bode, C. Holubarsch, J. L. Guermonprez, W. Wijns, A. Bartorelli, C. Constantini, M. Degertekin, K. Tanabe, C. Disco, E. Wuelfert, M. C. Morice, and R. S. Group, "Angiographic findings of the multicenter Randomized Study With the Sirolimus-Eluting Bx

Velocity Balloon-Expandable Stent (RAVEL): sirolimus-eluting stents inhibit restenosis irrespective of the vessel size," *Circulation,* vol. 106, pp. 1949-1956, Oct 2002.

[56] H. Kramer, S. Weckbach, G. van Kaick, M. F. Reiser, and S. O. Schoenberg, "[Screening in cardiovascular diseases.]," *Radiologe,* vol. 48, pp. 52-62, Jan 2008.

[57] A. T. Hirsch, T. P. Murphy, M. B. Lovell, G. Twillman, D. Treat-Jacobson, E. M. Harwood, E. R. Mohler, 3rd, M. A. Creager, R. W. Hobson, 2nd, R. M. Robertson, W. J. Howard, P. Schroeder, and M. H. Criqui, "Gaps in public knowledge of peripheral arterial disease: the first national PAD public awareness survey," *Circulation,* vol. 116, pp. 2086-2094, Oct 2007.

[58] B. H. Elsman, D. A. Legemate, F. W. van der Heyden, H. de Vos, W. P. Mali, and B. C. Eikelboom, "The use of color-coded duplex scanning in the selection of patients with lower extremity arterial disease for percutaneous transluminal angioplasty: a prospective study," *Cardiovasc Intervent Radiol,* vol. 19, pp. 313-316, Sep-Oct 1996.

[59] S. Lujan, E. Criado, E. Puras, and L. M. Izquierdo, "Duplex scanning or arteriography for preoperative planning of lower limb revascularisation," *Eur J Vasc Endovasc Surg,* vol. 24, pp. 31-36, Jul 2002.

[60] J. K. Avenarius, J. C. Breek, L. E. Lampmann, D. P. van Berge Henegouwen, and J. F. Hamming, "The additional value of angiography after colour-coded duplex on decision making in patients with critical limb ischaemia. A prospective study," *Eur J Vasc Endovasc Surg,* vol. 23, pp. 393-397, May 2002.

[61] A. N. Katsamouris, A. D. Giannoukas, D. Tsetis, T. Kostas, I. Petinarakis, and N. Gourtsoyiannis, "Can ultrasound replace arteriography in the management of chronic arterial occlusive disease of the lower limb?," *Eur J Vasc Endovasc Surg,* vol. 21, pp. 155-159, Feb 2001.

[62] T. Mandolfino, A. Canciglia, S. Lamberto, A. Carmignani, M. D'Alfonso, and A. Bottari, "[Comparison between magnetic resonance angiography and duplex ultrasound for preoperative planning of lower limb revascularisation]," *Chir Ital,* vol. 57, pp. 615-620, Sep-Oct 2005.

[63] A. Krnic, N. Vucic, and Z. Sucic, "Duplex scanning compared with intra-arterial angiography in diagnosing peripheral arterial disease: three analytical approaches," *Vasa,* vol. 35, pp. 86-91, May 2006.

[64] R. Kagawa, Y. Okada, T. Shima, M. Nishida, K. Yamane, and K. Moritake, "B-mode ultrasonographic investigations of morphological changes in endarterectomized carotid artery," *Surg Neurol,* vol. 55, pp. 50-56; Jan 2001.

[65] L. Allard, G. Cloutier, L. G. Durand, G. O. Roederer, and Y. E. Langlois, "Limitations of ultrasonic duplex scanning for diagnosing lower limb arterial stenoses in the presence of adjacent segment disease," *J Vasc Surg,* vol. 19, no. 4, pp. 650-657, Apr 1994.

[66] A. Gee, R. Prager, G. Treece, and L. Berman, "Engineering a freehand 3D ultrasound system," *Pattern Recognition Letters,* vol. 24, pp. 757-777, Feb 2003.

[67] O. V. Solberg, F. Lindseth, H. Torp, R. E. Blake, and T. A. Nagelhus Hernes, "Freehand 3D ultrasound reconstruction algorithms--a review," *Ultrasound Med Biol,* vol. 33, no. 7, pp. 991-1009, Jul 2007.

[68] T. R. Nelson, "Three-dimensional imaging," *Ultrasound Med Biol,* vol. 26, pp. 35-38, May 2000.

[69] "User manual", in *Sonix ultrasound system*, Burnaby, B.C., 2005 (report).

[70] A. Fenster, and D. B. Downey, "Three-dimensional ultrasound imaging," *Annu. Rev. Biomed. Eng.,* vol. 2, pp. 457-475, May 2000.

[71] L. Mercier, T. Lango, F. Lindseth, and D. L. Collins, "A review of calibration techniques for freehand 3-D ultrasound systems," *Ultrasound Med Biol,* vol. 31, pp. 449-471, Apr 2005.

[72] C. Laporte, and T. Arbel, "Combinatorial and probabilistic fusion of noisy correlation measurements for untracked freehand 3-D ultrasound," *IEEE Trans Med Imaging,* vol. 27, pp. 984-994, Jul 2008.

[73] A. H. Gee, R. J. Housden, P. Hassenpflug, G. M. Treece, and R. W. Prager, "Sensorless freehand 3D ultrasound in real tissue: Speckle decorrelation without fully developed speckle," *Med Imag Anal,* vol. 10, pp. 137-149, Sept 2006.

[74] R. J. Housden, A. H. Gee, G. M. Treece, and R. W. Prager, "Sensorless reconstruction of unconstrained freehand 3D ultrasound data," *Ultrasound Med Biol,* vol. 33, pp. 408-419, Mar 2007.

[75] T. R. Nelson, and D. H. Pretorius, "Three-dimensional ultrasound imaging," *Ultrasound Med Biol,* vol. 24, pp. 1243-1270, Dec 1998.

[76] R. N. Rankin, A. Fenster, D. B. Downey, P. L. Munk, M. F. Levin, and A. D. Vellet, "Three-dimensional sonographic reconstruction: techniques and diagnostic applications," *AJR Am J Roentgenol,* vol. 161, pp. 695-702, Oct 1993.

[77] A. Fenster, and D. B. Downey, "Three-dimensional ultrasound imaging and its use in quantifying organ and pathology volumes," *Anal Bioanal Chem,* vol. 377, pp. 982-989, Nov 2003.

[78] R. W. Prager, R. N. Rohling, A. H. Gee, and L. Berman, "Rapid calibration for 3-D freehand ultrasound," *Ultrasound Med Biol,* vol. 24, no. 6, pp. 855-869, Jul 1998.

[79] T. C. Poon, and R. N. Rohling, "Comparison of calibration methods for spatial tracking of a 3-D ultrasound probe," *Ultrasound Med Biol,* vol. 31, pp. 1095-1108, Aug 2005.

[80] J. A. Panza, "Real-time three-dimensional echocardiography: an overview," *Int J Cardiovasc Imaging* vol. 17, pp. 227-235, Jun 2001.

[81] R. M. Lang, V. Mor-Avi, L. Sugeng, P. S. Nieman, and D. J. Sahn, "Three-dimensional echocardiography: the benefits of the additional dimension," *J Am Coll Cardiol,* vol. 48, pp. 2053-2069, Nov 2006.

[82] N. C. Nanda, and A. P. Miller, "Real time three-dimensional echocardiography: specific indications and incremental value over traditional echocardiography," *J Cardiol,* vol. 48, pp. 291-303, Dec 2006.

[83] G. Valocik, O. Kamp, and C. A. Visser, "Three-dimensional echocardiography in mitral valve disease," *Eur J Echocardiogr,* vol. 6, pp. 443-454, Dec 2005.

[84] J. N. Welch, "Design, implementation, and analysis of a three-dimensional ultrasound system for image-guided surgery," Ph.D. Thesis, Stanford University, United States, California, 2003.

[85] F. Rousseau, "Méthodes d'analyse d'image et de calibration pour l'échographie 3D en mode main-libre," Ph.D. Thesis, Institut de Formation Supérieur en Informatique et Communication, VISTA, IRISA, RENNES, 2003.

[86] M. E. Legget, D. F. Leotta, E. L. Bolson, J. A. McDonald, R. W. Martin, L. Xiang-Ning, C. M. Otto, and F. H. Sheehan, "System for quantitative three-dimensional echocardiography of the left ventricle based on a magnetic-field position and orientation sensing system," *IEEE Trans Biomed Eng,* vol. 45, pp. 494-504, Apr 1998.

[87] D. L. King, D. L. King, Jr., and M. Y. Shao, "Evaluation of in vitro measurement accuracy of a three-dimensional ultrasound scanner," *J Ultrasound Med,* vol. 10, pp. 77-82, Feb 1991.

[88] D. L. King, Gopal, A. S., Shen, Z., Schnellbaecher, M. J., King Jr., D. L., Keller, A. M., Sapin, P. M., Schroder, K. M., Akinboboye, O.O., "Three-Dimensional Echocardiography: Optimizing the Amount of Data Acquired for Determination of Left Ventricular Ejection Fraction," *Computers in Cardiology*, pp. 205 - 208, Sep 1994.

[89] A. Delcker, and H.-C. Diener, "Quantification of atherosclerotic plaques in carotid arteries by three-dimensional ultrasound," *Br J Radio,* vol. 67, pp. 672-678, Sep 1994.

[90] A. Delcker, H.-C. Diener, and H. Wilhelm, "Influence of vascular risk factors for atherosclerotic carotid artery plaque progression," *Stroke: Am Heart Assoc,* vol. 26, pp. 2016-2022, Nov 1995.

[91] A. Landry, J. D. Spence, and A. Fenster, "Quantification of carotid plaque volume measurements using 3D ultrasound imaging," *Ultrasound Med Biol,* vol. 31, pp. 751-762, Jun 2005.

[92] M. Egger, J. D. Spence, A. Fenster, and G. Parraga, "Validation of 3D ultrasound vessel wall volume: an imaging phenotype of carotid atherosclerosis," *Ultrasound Med Biol,* vol. 33, pp. 905-914, Jun 2007.

[93] D. F. Leotta, P. R. Detmer, and R. W. Martin, "Performance of a miniature magnetic position sensor for three-dimensional ultrasound imaging," *Ultrasound Med Biol,* vol. 23, pp. 597-609, Dec 1997.

[94] P. R. Detmer, G. Bashein, T. Hodges, K. W. Beach, E. P. Filer, D. H. Burns, and D. E. Strandness, Jr., "3D Ultrasonic image feature localization based on magnetic scanhead tracking: in vitro calibration and validation," *Ultrasound Med Biol,* vol. 20, pp. 923-936, Apr 1994.

[95] R. W. Prager, A. Gee, and L. Berman, "Stradx: real-time acquisition and visualization of freehand three-dimensional ultrasound," *Med Image Anal,* vol. 3, pp. 129-40, Jun 1999.

[96] K. W. Lee, N. B. Wood, and X. Y. Xu, "Ultrasound image-based computer model of a common carotid artery with a plaque," *Med Eng Phys,* vol. 26, pp. 823-840, Dec 2004.

[97] K. Dionisio, V. R. Chan, L. W. Campbell, J. Connelly, W. C. Karl, and R. S. Lees, "Three-dimensional characterization of carotid plaque structure and deformation with noninvasive ultrasound imaging," in *IEEE Conference of Computers in Cardiology,* Chicago, IL, USA, 19-22 Sept 2004, pp. 237-240.

[98] F. P. Glor, B. Ariff, A. D. Hughes, P. R. Verdonck, S. A. Thom, D. C. Barratt, and X. Y. Xu, "Operator dependence of 3-D ultrasound-based computational fluid dynamics for the carotid bifurcation," *IEEE Trans Med Imaging,* vol. 24, pp. 451-456, Apr 2005.

[99] D. C. Barratt, B. B. Ariff, K. N. Humphries, S. A. Thom, and A. D. Hughes, "Reconstruction and quantification of the carotid artery birfucation from 3-D ultrasound images," *IEEE Trans Med Imaging,* vol. 23, pp. 567-583, May 2004.

[100] C. P. Allott, C. D. Barry, R. Pickford, and J. C. Waterton, "Volumetric assessment of carotid artery bifurcation using freehand-acquired, compound 3D ultrasound," *Br J Radiol,* vol. 72, pp. 289-292, Mar 1999.

[101] T. Wessels, J. U. Harrer, S. Stetter, M. Mull, and C. Klotzsch, "Three-dimensional assessment of extracranial Doppler sonography in carotid artery stenosis compared with digital subtraction angiography," *Stroke,* vol. 35, pp. 1847-1851, Aug 2004.

[102] T. C. Hodges, P. R. Detmer, D. H. Burns, K. W. Beach, and D. E. Strandness, Jr., "Ultrasonic three-dimensional reconstruction: in vitro and in vivo volume and area measurement," *Ultrasound Med Biol,* vol. 20, pp. 719-729, Apr 1994.

[103] D. F. Leotta, J. F. Primozich, K. W. Beach, R. O. Bergelin, R. E. Zierler, and D. E. Strandness, Jr., "Remodeling in peripheral vein graft revisions: serial study with three-dimensional ultrasound imaging," *Journal of Vascular Surgery,* vol. 37, no. 4, pp. 798-807, Apr, 2003.

[104] D. F. Leotta, J. F. Primozich, S. M. Henderson, L. N. Karr, R. O. Bergelin, K. W. Beach, and R. E. Zierler, "Display of spatially-registered Doppler spectral waveforms and three-dimensional vein graft geometry," *Ultrasound Med Biol,* vol. 31, no. 10, pp. 1317-26, Oct, 2005.

[105] J. U. Harrer, T. Wessels, S. Poerwowidjojo, W. Moller-Hartmann, and C. Klotzsch, "Three-dimensional color-coded duplex sonography for assessment of the vertebral artery origin and vertebral artery stenoses," *J Ultr Med,* vol. 23, pp. 1049-1056, Aug 2004.

[106] W. Birkfellner, F. Watzinger, and F. Wanschitz, "Systematic distortions in magnetic position digitizers," *Med Phys,* vol. 25, pp. 2242-2248, Nov 1998.

[107] F. Poulin, and L. P. Amiot, "Interference during the use of an electromagnetic tracking system under OR conditions," *J Biomech,* vol. 35, pp. 733-737, Jun 2002.

[108] F. Lindseth, T. Lango, J. Bang, and T. A. Nagelhus Hernes, "Accuracy evaluation of a 3D ultrasound-based neuronavigation system," *Comput Aided Surg,* vol. 7, pp. 197-222, Nov 2002.

[109] O. Chavanon, L. Carrat, C. Pasqualini, E. Dubois, D. Blin, and J. Troccaz, “Computer-guided pericardiocentesis: experimental results and clinical perspectives,” *Herz,* vol. 25, pp. 762-768, Dec 2000.

[110] J. W. Trobaugh, D. J. Trobaugh, and W. D. Richard, “Three-dimensional imaging with stereotactic ultrasonography,” *Comput Med Imaging Graph,* vol. 18, pp. 315-323, Sep-Oct 1994.

[111] C. J. Cash, A. M. Sardesai, L. H. Berman, M. J. Herrick, G. M. Treece, R. W. Prager, and A. H. Gee, “Spatial mapping of the brachial plexus using three-dimensional ultrasound,” *Br J Radiol,* vol. 78, pp. 1086-1094, Dec 2005.

[112] M. Cartellieri, J. Kremser, and F. Vorbeck, “Comparison of different 3D navigation systems by a clinical "user",” *Eur Arch Otorhinolaryngol,* vol. 258, pp. 38-41, Jan 2001.

[113] Y. Suya, U. Neumann, and R. Azuma, "Hybrid inertial and vision tracking for augmented reality registration," in *IEEE Comput. Soc. Tech. Committee on Visualization & Graphics*, Los Alamitos, CA, USA, 13-17 March 1999, pp. 260-267.

[114] T. Auer, S. Brantner, and A. Pinz, "The integration of optical and magnetic tracking for multi-user augmented reality," in *5th Eurographics Workshop on Virtual Environments*, Wien, Austria, 31 May-1 June 1999, pp. 43-52.

[115] T. Auer, and A. Pinz, "Building a hybrid tracking system: integration of optical and magnetic tracking," in *2nd International Workshop on Augmented Reality*, Los Alamitos, CA, USA, 20-21 Oct 1999, pp.13-22.

[116] M. Nakamoto, K. Nakada, Y. Sato, K. Konishi, M. Hashizume, and S. Tamura, “Intraoperative magnetic tracker calibration using a magneto-optic hybrid tracker for 3D ultrasound-based navigation in laparoscopic surgery,” *IEEE Trans Med Imaging,* vol. 27, pp. 255-270, Feb 2008.

[117] D. Zetu, P. Banerjee, and D. Thompson, “Extended-range hybrid tracker and applications to motion and camera tracking in manufacturing systems,” *IEEE Trans Rob Autom,* vol. 16, pp. 281-293, Jun 2000.

[118] A. State, M. A. Livingston, W. F. Garrett, G. Hirota, M. C. Whitton, E. D. Pisano, and H. Fuchs, "Technologies for augmented reality systems: realizing ultrasound-guided needle biopsies," in *Computer Graphics and Interactive Techniques,* New York, NY, USA, 4-9 Aug 1996, pp. 439-446.

[119] G. Duchemin, P. Poignet, E. Dombre, and F. Pierrot, “Medically safe and sound,” *IEEE Rob Autom,* vol. 11, pp. 46-55, Jun 2004.

[120] C. Delgorge, F. Courreges, L. A. Bassit, C. Novales, C. Rosenberger, N. Smith-Guerin, C. Bru, R. Gilabert, M. Vannoni, G. Poisson, and P. Vieyres, “A tele-operated mobile ultrasound scanner using a light-weight robot,” *IEEE Trans Inform Techn Biomed,* vol. 9, pp. 50-58, Mar 2005.

[121] F. Courreges, P. Vieyres, and R. S. H. Istepanian, "Advances in robotic tele-echography services - The OTELO system," in *IEEE Engineering in Medicine and Biology Society*, San Francisco, CA, United States, 1-5 Sept 2004, pp. 5371-5374.

[122] P. Vieyres, G. Poisson, F. Courreges, O. Merigeaux, and P. Arbeille, “The TERESA project: from space research to ground tele-echography,” *Industrial Robot,* vol. 30, pp. 77-82, Jun 2003.

[123] A. Vilchis, J. Troccaz, P. Cinquin, K. Masuda, and F. Pellissier, “A new robot architecture for tele-echography,” *IEEE Trans Rob Autom,* vol. 19, pp. 922-926, Oct 2003.

[124] A. Vilchis, K. Masuda, M. Althuser, J. Ayoubi, J. Bosson, J. Troccaz, and P. Cinquin, “Télé-Échographie Robotisée: des concepts à la validation clinique,” *Annals of Telecommunications,* vol. 58, pp. 687-697, 2003 (report).

[125] K. Masuda, E. Kimura, N. Tateishi, and K. Ishihara, "Construction of 3D movable echographic diagnosis robot and remote diagnosis via fast digital network," in *IEEE Engineering in Medicine and Biology Society,* Istanbul, Turkey, 25-28 Oct 2001, pp. 3634-3637.

[126] K. Masuda, E. Kimura, N. Tateishi, and K. Ishihara, "Three dimensional motion mechanism of ultrasound probe and its application for tele-echography system," in *IEEE/RSJ International Conference on Intelligent Robots and Systems,* Maui, HI, USA, Oct 29-Nov 3 2001, pp. 1112-16.

[127] J. Guiochet, B. Tondu, and C. Baron, "Safety analysis and integration for robotic systems-application to a medical robot for tele-echography," in *International Conference on Robotics and Applications,* Anaheim, CA, USA, 19-22 Nov 2001, pp. 158-162.

[128] K. Masuda, E. Kimura, N. Tateishi, Y. Suzuki, and K. Ishihara, "Robotic tele-diagnosis system of echography and wireless experiment for mobile telemedicine," in *IEEE Engineering in Medicine and Biology Biology 24th Annual Conference,* Houston, TX, United States, Oct 23-26 2002, pp. 1855-1856.

[129] N. Philip, and R. S. H. Istepanian, "Medical quality of service for wireless ultrasound streaming in robotic tele-ultrasonography system," in *IEEE/ACSInternational Conference on Computer Systems and Applicatins,* Amman, Jordan, 13-16 May 2007, pp. 245-250.

[130] C. Delgorge, C. Rosenberger, G. Poisson, and P. Vieyres, "Evaluation of the quality of ultrasound image compression for a robotic tele-echographic system," in *Computers in Cardiology,* Lyon, France, 25-28 Sept 2005, 4 pages.

[131] N. Hungr, J. Troccaz, N. Zemiti, and N. Tripodi, "Design of an ultrasound-guided robotic brachytherapy needle-insertion system," in *31st Annual International Conference of the IEEE Engineering in Medicine and Biology Society,* Minneapolis, MN, USA, 3-6 Sept 2009, pp. 250-253.

[132] V. V. Karnik, A. Fenster, J. Bax, D. W. Cool, L. Gardi, I. Gyacskov, C. Romagnoli, and A. D. Ward, "Assessment of image registration accuracy in three-dimensional transrectal ultrasound guided prostate biopsy," *Med Phys,* vol. 37, pp. 802-813.

[133] W. Zhouping, L. Gardi, D. B. Downey, and A. Fenster, "Oblique needle segmentation and tracking for 3D TRUS guided prostate brachytherapy," *Med Phys,* vol. 32, pp. 2928-2941, Sept 2005.

[134] H. S. S. Ho, P. Mohan, E. D. Lim, D. L. Li, J. S. P. Yuen, W. S. Ng, W. K. O. Lau, and C. W. S. Cheng, "Robotic ultrasound-guided prostate intervention device: system description and results from phantom studies," *Int J Med Rob Comp As Surg,* vol. 5, pp. 51-58, Mar 2009.

[135] J. Bax, L. Gardi, J. Montreuil, D. Smith, and A. Fenster, "A compact robotic apparatus and method for 3-D ultrasound guided prostate therapy," in *Medical Imaging: Visualization and Image-Guided Procedures*, San Diego, CA, USA, 18 Feb 2007, pp. 65092H (8 pages).

[136] M. Preeti, H. Henry, D. Li, L. E. Wyn, L. Weber, C. Chris, and S. Ng Wan, "Ultrasound guided transperineal robotic biopsy system for the prostate," *in the 6th IASTED International Conference on Biomedical Engineering,* Innsbruck, Austria, 13-15 Feb 2008, pp. 292-297.

[137] G. Fichtinger, J. P. Fiene, C. W. Kennedy, G. Kronreif, I. Iordachita, D. Y. Song, E. C. Burdette, and P. Kazanzides, "Robotic assistance for ultrasound-guided prostate brachytherapy," *Med Imag Anal,* vol. 12, pp. 535-545, 2008.

[138] P. Poignet, E. Dombre, O. Merigeaux, F. Pierrot, and G. Duchemin, "Design and control issues for intrinsically safe medical robots," *Industrial Robot,* vol. 30, pp. 83-88, Jun 2003.

[139] S. Boudet, J. Gariepy, and S. Mansour, "An integrated robotics and medical control device to quantify atheromatous plaques: experiments on the arteries of a patient," in *IEEE/RSJ International Conference on Intelligent Robot and Systems,* New York, NY, USA, 7-11 Sept 1997, pp. 1533-1538.

[140] F. Pierrot, E. Dombre, E. Dégoulange, L. Urbain, P. Caron, S. Boudet, J. Gariépy, and J.-L. Mégnien, "Hippocrate: a safe robot arm for medical applications with force feedback," *Medical Image Analysis,* vol. 3, no. 3, pp. 285-300, Sep 1999.

[141] J. Levenson, F. Pessana, J. Gariepy, R. Armentano, and A. Simon, "Gender differences in wall shear-mediated brachial artery vasoconstriction and vasodilation," *J Am Col Cardiol,* vol. 38, pp. 1668-1674, Nov 2001.

[142] G. Duchemin, P. Maillet, P. Poignet, E. Dombre, and F. Pierrot, “A hybrid position/force control approach for identification of deformation models of skin and underlying tissues,” *IEEE Trans Biomed Eng,* vol. 52, pp. 160-170, Feb 2005.

[143] P. Abolmaesumi, S. E. Salcudean, and W. H. Zhu, "Visual servoing for robot-assisted diagnostic ultrasound," in *IEEE Engineering in Medicine and Biology Society,* Chicago, IL, USA, 23-24 July 2000, pp. 2532-2535.

[144] P. Abolmaesumi, M. R. Sirouspour, S. E. Salcudean, and W. H. Zhu, "Adaptive image servo controller for robot-assisted diagnostic ultrasound," in *IEEE/ASME International Conference on Advanced Intelligent Mechatronics,* Como, Italy, 8-12 July 2001, pp. 1199-1204.

[145] W. H. Zhu, S. E. Salcudean, S. Bachmann, and P. Abolmaesumi, "Motion/force/image control of a diagnostic ultrasound robot," in *IEEE International Conference on Robotics and Automation,* San Francisco, CA, USA, Apr 2000, pp. 1580-1585.

[146] P. Abolmaesumi, S. E. Salcudean, Z. Wen-Hong, M. R. Sirouspour, and S. P. DiMaio, “Image-guided control of a robot for medical ultrasound,” *IEEE Transactions on Robotics and Automation,* vol. 18, pp. 11-23, Feb 2002.

[147] M. Blanchard, R. Geoffroy, G. Cloutier, J. De Guise, P. Bigras, and L. G. Durand, "3D Ultrasonic Robotic Scanner," in *Integral*, Montreal, 2002, pp. 1-20 (report).

[148] M. A. Janvier, L. G. Durand, M. H. Roy-Cardinal, I. Renaud, B. Chayer, P. Bigras, J. de Guise, G. Soulez, and G. Cloutier, “Performance evaluation of a medical robotic 3D-ultrasound imaging system,” *Med Image Anal,* vol. 12, pp. 275-290, Jun 2008.

[149] G. D. Giannoglou, Y. S. Chatzizisis, V. Koutkias, I. Kompatsiaris, M. Papadogiorgaki, V. Mezaris, E. Parissi, P. Diamantopoulos, M. G. Strintzis, N. Maglaveras, G. E. Parcharidis, and G. E. Louridas, “A novel active contour model for fully automated segmentation of intravascular ultrasound images: in vivo validation in human coronary arteries,” *Comp Biol Med,* vol. 37, pp. 1292-1302, Feb 2007.

[150] M. M. McDermott, P. Greenland, K. Liu, J. M. Guralnik, L. Celic, M. H. Criqui, C. Chan, G. J. Martin, J. Schneider, W. H. Pearce, L. M. Taylor, and E. Clark, “The ankle brachial index is associated with leg function and physical activity: the walking and leg circulation study,” *Ann Inter Med,* vol. 136, pp. 873-883, Aug 2002.

[151] B. H. Elsman, D. A. Legemate, H. J. de Vos, W. P. Mali, and B. C. Eikelboom, “Hyperaemic colour duplex scanning for the detection of aortoiliac stenoses. A comparative study with intra-arterial pressure measurement,” *Eur J Vasc Endovasc Surg,* vol. 14, pp. 462-467, Dec 1997.

[152] Y. Matignon, "Échographie-Doppler dans l'artériopathie oblitérante des membres inférieurs," in *Agence Nationale d'Accrédition et d'Évaluation en Santé*, 2004, pp. 1-144 (report).

[153] Sonix ultrasound system, ″User manual," *Ultrasonix Medical Corporation*, Burnaby, B. C., October 2005 (report).

[154] W. Birkfellner, F. Watzinger, and F. Wanschitz, “Calibration of tracking systems in a surgical environment,” *IEEE Trans Med Imag,* vol. 17, pp. 737-742, Oct 1998.

[155] D. D. Frantz, A. D. Wiles, S. E. Leis, and S. R. Kirsh, “Accuracy assessment protocols for electromagnetic tracking systems,” *Phys Med Biol,* vol. 48, pp. 2241-2251, Jul 2003.

[156] A. V. Gonzales, P. Cinquin, J. Troccaz, A. Guerraz, B. Hennion, and P. e. al., "TER: a system for robotic tele-echography", in *Medical Image Computing and Computer-Assisted Intervention (MICCAI)*, The Netherlands, 2001, pp. 326-334.

[157] C.-S. Tseng, C.-C. Huang, and C.-S. Chen, “Development of an image-guided robotic system for surgical positioning and drilling,” *Robotica,* vol. 25, pp. 375-383, May-June 2007.

[158] C. Mavroidis, J. Flanz, S. Dubowsky, P. Drouet, and M. Goitein, “High performance medical robot requirements and accuracy analysis,” *Robotics and Computer-Integrated Manufacturing,* vol. 14, pp. 329-338, Oct-Dec 1998.

[159] B. W. Mooring, Z. S. Roth, and M. R. Driels, *Fundamentals of Manipulator Calibration*, New York, 1991.

[160] P. R. Detmer, G. Bashein, T. Hodges, K. W. Beach, E. P. Filer, D. H. Burns, and D. E. Strandness, Jr., "3D ultrasonic image feature localization based on magnetic scanhead tracking: in vitro calibration and validation," *Ultrasound Med Biol,* vol. 20, pp. 923-936, Jan 1994.

[161] A. Hartov, S. D. Eisner, M. S. David, W. Roberts, K. D. Paulsen, L. A. Platenik, and M. I. Miga, "Error analysis for a free-hand three-dimensional ultrasound system for neuronavigation," *Neurosurgical Focus,* vol. 6, 1999.

[162] D. C. Barratt, A. H. Davies, A. D. Hughes, S. A. Thom, and K. N. Humphries, "Accuracy of an electromagnetic three-dimensional ultrasound system for carotid artery imaging," *Ultrasound Med Biol,* vol. 27, pp. 1421-1425, Oct 2001.

[163] G. Cloutier, S. D. Qanadli, P. Teppaz, L. Allard, Z. Qin, F. Cloutier, and L.-G. Durand, "A multimodality vascular imaging phantom with fiducial markers visible in DSA, CTA, MRA, and ultrasound," *Med Phys,* vol. 31, pp. 1424-1433, June 2004.

[164] R. Khadem, C. Yeh, M. Sadeghi-Tehrani, and M. R. Bax, "Comparative tracking error analysis of five different optical tracking systems," *Comp Aid Surg,* vol. 5, pp. 98-107, Jun 2000.

[165] A. Hernandez, O. Basset, P. Chirossel, and G. Gimenez, "Spatial compounding in ultrasonic imaging using an articulated arm," *Ultrasound Med Biol,* vol. 22, pp. 229-238, Jan 1996.

[166] K. F. Dajani, "Analysis of carotid and femoral stenosis and lesions with three-dimensional ultrasound," PhD Thesis, The University of Toledo, United States, Ohio, USA, 2000.

[167] L. Zollo, B. Siciliano, A. De Luca, E. Guglielmelli, and P. Dario, "Compliance control for an anthropomorphic robot with elastic joints: theory and experiments," *Trans ASME J Dyn Sys, Meas Contr,* vol. 127, pp. 321-328, Sept 2005.

[168] R. L. Maurice, J. Ohayon, Y. Fretigny, M. Bertrand, G. Soulez , and G. Cloutier, "Noninvasive vascular elastography: theoretical framework," *IEEE Trans Med Imag,* vol. 23, pp. 164-180, Feb 2004.

[169] J. Guerrero, E. Salcudean, A. McEwen, B. A. Masri, and S. Nicolaou, "System for deep venous thrombosis detection using objective compression measures," *IEEE Trans Biomed Eng,* vol. 53, pp. 845-854, May 2006.

[170] A. T. Hirsch, Z. J. Haskal, N. R. Hertzer, C. W. Bakal, M. A. Creager, J. L. Halperin, L. F. Hiratzka, W. R. Murphy, J. W. Olin, J. B. Puschett, K. A. Rosenfield, D. Sacks, J. C. Stanley, L. M. Taylor, Jr., C. J. White, J. White, R. A. White, E. M. Antman, S. C. Smith, Jr., C. D. Adams, J. L. Anderson, D. P. Faxon, V. Fuster, R. J. Gibbons, S. A. Hunt, A. K. Jacobs, R. Nishimura, J. P. Ornato, R. L. Page, and B. Riegel, "ACC/AHA Guidelines for the Management of Patients with Peripheral Arterial Disease (lower extremity, renal, mesenteric, and abdominal aortic): a collaborative report from the American Associations for Vascular Surgery/Society for Vascular Surgery, Society for Cardiovascular Angiography and Interventions, Society for Vascular Medicine and Biology, Society of Interventional Radiology, and the ACC/AHA Task Force on Practice Guidelines (writing committee to develop guidelines for the management of patients with peripheral arterial disease)--summary of recommendations," *J Vasc Interv Radiol,* vol. 17, pp. 1383-1397; Sep, 2006.

[171] A. T. Hirsch, Z. J. Haskal, N. R. Hertzer, C. W. Bakal, M. A. Creager, J. L. Halperin, L. F. Hiratzka, W. R. Murphy, J. W. Olin, J. B. Puschett, K. A. Rosenfield, D. Sacks, J. C. Stanley, L. M. Taylor, Jr., C. J. White, J. White, R. A. White, E. M. Antman, S. C. Smith, Jr., C. D. Adams, J. L. Anderson, D. P. Faxon, V. Fuster, R. J. Gibbons, J. L. Halperin, L. F. Hiratzka, S. A. Hunt, A. K. Jacobs, R. Nishimura, J. P. Ornato, R. L. Page, and B. Riegel, "ACC/AHA 2005 guidelines for the management of patients with peripheral arterial disease (lower extremity, renal, mesenteric, and abdominal aortic): executive summary a collaborative report from the American Association for Vascular Surgery/Society for Vascular Surgery, Society for Cardiovascular Angiography and Interventions, Society for Vascular Medicine and Biology, Society of Interventional Radiology, and the ACC/AHA Task Force on Practice Guidelines (Writing Committee to Develop Guidelines for the Management

of Patients With Peripheral Arterial Disease) endorsed by the American Association of Cardiovascular and Pulmonary Rehabilitation; National Heart, Lung, and Blood Institute; Society for Vascular Nursing; TransAtlantic Inter-Society Consensus; and Vascular Disease Foundation," *J Am Coll Cardiol,* vol. 47, pp. 1239-1312, Mar 2006.

[172] S. D. Boskovic, and A. N. Neskovic, "Atherosclerosis plaque regression," *Med Pregl,* vol. 59, pp. 38-45, Jan-Feb 2006.

[173] M. Cartellieri, F. Vorbeck, and J. Kremser, "Comparison of different 3D navigation systems by a clinical user," *Acta Arch Otolaryngol,* vol. 258, pp. 38-41, Jan 2001.

[174] P. Abolmaesumi, S. E. Salcudean, W.-H. Zhu, M. R. Sirouspour, and S. P. DiMaio, "Image-guided control of a robot for medical ultrasound," *IEEE Trans Rob Autom,* vol. 18, pp. 11-23, Feb 2002.

[175] P. Arbeille, G. Poisson, P. Vieyres, J. Ayoub, M. Porcher, and J. L. Boulay, "Echographic examination in isolated sites controlled from an expert center using a 2-D echograph guided by a teleoperated robotic arm," *Ultrasound Med Biol,* vol. 29, pp. 993-1000, July 2003.

[176] S. Dandekar, Y. Li, J. Molloy, and J. Hossack, "A phantom with reduced complexity for spatial 3-D ultrasound calibration," *Ultrasound Med Biol,* vol. 31, pp. 1083-1093, Aug 2005.

[177] P.-W. Hsu, R. W. Prager, A. H. Gee, and G. M. Treece, "Rapid, easy and reliable calibration for freehand 3D ultrasound," *Ultrasound in Medicine & Biology,* vol. 32, pp. 823-835, Jun 2006.

[178] F. Lindseth, G. A. Tangen, T. Lango, and J. Bang, "Probe calibration for freehand 3-D ultrasound," *Ultrasound Med Biol,* vol. 29, pp. 1607-1623, Nov 2003.

[179] N. Pagoulatos, D. R. Haynor, and Y. Kim, "A fast calibration method for 3-D tracking of ultrasound images using a spatial localizer," *Ultrasound Med Biol,* vol. 27, pp. 1219-1229, Sep 2001.

[180] P. W. Hsu, R. W. Prager, A. H. Gee, and G. M. Treece, "Real-time freehand 3D ultrasound calibration," *Ultrasound Med Biol,* vol. 34, pp. 239-251, Feb 2008.

[181] L. G. Bouchet, S. L. Meeks, G. Goodchild, F. J. Bova, J. M. Buatti, and W. A. Friedman, "Calibration of three-dimensional ultrasound images for image-guided radiation therapy," *Phys Med Biol,* vol. 46, pp. 559-577, Feb 2001.

[182] J. F. Polak, *Peripheral Vascular Sonography*, 2nd , Philadelphia: Lippincott Williams & Wilkins, 2004.

[183] F. Lindseth, J. Bang, and T. Lango, "A robust and automatic method for evaluating accuracy in 3-D ultrasound-based navigation," *Ultrasound Med Bio,* vol. 29, , pp. 1439-1452, Oct 2003.

[184] D. F. Leotta, J. F. Primozich, K. W. Beach, R. O. Bergelin, and D. E. Strandness, Jr., "Serial measurement of cross-sectional area in peripheral vein grafts using three-dimensional ultrasound," *Ultrasound Med Biol,* vol. 27, pp. 61-68, Jan 2001.

[185] D. F. Leotta, P. R. Detmer, and R. W. Martin, "Performance of a miniature magnetic position sensor for three-dimensional ultrasound imaging," *Ultrasound Med Biol,* vol. 23, pp. 597-609, Dec 1997.

[186] K. M. Kanal, J. M. Kofler, and D. S. Groth, "Comparison of selected ultrasound performance tests with varying," *Med Phys,* vol. 25, pp. 642-647, May 1998.

[187] F. Rousseau, P. Hellier, M. M. J. Letteboer, W. J. Niessen, and C. Barillot, "Quantitative evaluation of three calibration methods for 3-D freehand ultrasound," *IEEE Trans Med Imag,* vol. 25, pp. 1492-1501, Nov 2006.

[188] E. Von Lavante, and J. A. Noble, "Segmentation of breast cancer masses in ultrasound using radio-frequency signal derived parameters and strain estimates," in *IEEE International Symposium on Biomedical Imaging: From Nano to Macro,* Paris, France, 14-17 May 2008, pp. 536-539.

[189] X. Wen, S. E. Salcudean, and P. D. Lawrence, "Detection of brachytherapy seeds using ultrasound radio frequency signals," in *Medical Imaging 2006: Ultrasonic Imaging ans Signal Processing*, San Diego, CA, United States, 12 Feb 2006, pp. 61470J-1-8

[190] D. F. Leotta, J. F. Primozich, K. W. Beach, R. O. Bergelin, K. D. Gibson, and D. E. Strandness, Jr., "Cross-sectional area changes in peripheral vein grafts monitored by three-dimensional ultrasound imaging," *in IEEE Ultrasonics Symposium,* San Juan, Puerto Rico, 22-25 Oct 2000, pp. 1865-1868.

[191] D. F. Leotta, and R. W. Martin, "Three-dimensional spatial compounding of ultrasound scans with weighting by incidence angle," *Ultrasonic Imaging,* vol. 22, pp. 1-19, 2000.

[192] C. D. Barry, C. P. Alliott, N. W. John, P. M. Mellor, P. A. Arundel, D. S. Thomson, and J. C. Waterton, "Three-dimensional freehand ultrasound: image reconstruction and volume analysis," *Ultrasound Med Biol,* vol. 23, pp. 1209-1224, 1997.

[193] M. Lecart, M. H. R. Cardinal, Q. Zhao, G. Soulez, and G. Cloutier, "In vitro in-stent restenoses evaluated by 3D ultrasound," *Med Phys,* vol. 36, pp. 513-522, Feb 2009.

[194] R. Collins, G. Cranny, J. Burch, R. Aguiar-Ibanez, D. Craig, K. Wright, E. Berry, M. Gough, J. Kleijnen, and M. Westwood, "A systematic review of duplex ultrasound, magnetic resonance angiography and computed tomography angiography for the diagnosis and assessment of symptomatic, lower limb peripheral arterial disease," *Health Technol Assess,* vol. 11, pp. 1-184, May 2007.

[195] G. J. Landry, G. L. Moneta, L. M. Taylor, Jr., J. M. Edwards, and R. A. Yeager, "Comparison of procedural outcomes after lower extremity reversed vein grafting and secondary surgical revision," *J Vasc Surg,* vol. 38, pp. 22-28, Jul 2003.

[196] D. F. Leotta, J. F. Primozich, K. W. Beach, R. O. Bergelin, R. E. Zierler, and D. E. Strandness, Jr., "Remodeling in peripheral vein graft revisions: serial study with three-dimensional ultrasound imaging," *J Vasc Surg,* vol. 37, pp. 798-807, Apr 2003.

[197] D. F. Leotta, J. F. Primozich, C. M. Lowe, L. N. Karr, R. O. Bergelin, K. W. Beach, and R. E. Zierler, "Measurement of anastomosis geometry in lower extremity bypass grafts with 3-D ultrasound imaging," *Ultrasound Med Biol,* vol. 31, pp. 1305-1315, Oct 2005.

[198] K. W. Lee, N. B. Wood, and X. Y. Xu, "Ultrasound image-based computer model of a common carotid artery with a plaque," *Med Eng Phys,* vol. 26, pp. 823-840, Dec 2004.

[199] J. Bax, D. Cool, L. Gardi, K. Knight, D. Smith, J. Montreuil, S. Sherebrin, C. Romagnoli, and A. Fenster, "Mechanically assisted 3D ultrasound guided prostate biopsy system," *Med Phys,* vol. 35, pp. 5397-5410, Dec 2008.

[200] V. Lagerburg, M. A. Moerland, M. van Vulpen, and J. J. W. Lagendijk, "A new robotic needle insertion method to minimise attendant prostate motion," *Radiotherapy and Oncology,* vol. 80, no. 1, pp. 73-77, July 2006.

[201] E. Dombre, G. Duchemin, P. Poignet, and F. Pierrot, "Dermarob: a safe robot for reconstructive surgery," *IEEE Trans Rob Autom,* vol. 19, pp. 876-884, Oct 2003.

[202] M. A. Janvier, Soulez, G., Allard, L., Cloutier, G., "Validation of 3D reconstructions of a mimicked femoral artery with an ultrasound imaging robotic system", *Med Phys*, vol. 37, pp. 3868-3879.

[203] L. Allard, G. Soulez , B. Chayer, Z. Qin, and G. Cloutier, "Multimodality vascular imaging phantoms: a new material for the fabrication of pathilogical 3D vessel geometries," *Med Phys,* vol. 36, pp. 3758-3763, Aug 2009.

[204] P. J. Besl, and H. D. McKay, "A method for registration of 3-D shapes," *IEEE Trans Patt Anal Mach Intel,* vol. 14, pp. 239-256, Feb 1992.

[205] B. K. P. Horn, "Closed-form solution of absolute orientation using unit quaternions," *J Opt Soc Am A,* vol. 4, pp. 629-642, Apr 1987.

[206] F. Rengier, T. F. Weber, F. L. Giesel, D. Bockler, H. U. Kauczor, and H. von Tengg-Kobligk, "Centerline analysis of aortic CT angiographic examinations: benefits and limitations," *Am J Roentgenology,* vol. 192, pp. W255-63, May 2009.

[207] Y. Kato, H. Sano, K. Katada, Y. Ogura, M. Hayakawa, N. Kanaoka, and T. Kanno, “Application of three-dimensional CT angiography (3D-CTA) to cerebral aneurysms,” *Surgical Neurology,* vol. 52, pp. 113-122, Aug 1999.

[208] S. Lessard, P. Bigras, and I. A. Bonev, “A New Medical Parallel Robot and Its Static Balancing Optimization,” *J Med Dev,* vol. 1, pp. 272-278, Dec 2007.

[209] B. L. Davies, "Robotic surgery: at the cutting edge of technology," in *7th International Workshop on Advanced Motion Control,* Maribor, Slovenia, 3-5 July 2002, pp. 15-18.

[210] D. Daney, Y. Papegay, and A. Neumaier, "Interval methods for certification of the kinematic calibration of parallel robots," in *IEEE International Conference on Robotics and Automation, New Olreans ,* LA, USA, April-1 May 2004, pp. 1913-1918.

[211] M. A. Meggiolaro, and S. Dubowsky, "Analytical method to eliminate the redundant parameters in robot calibration," in *IEEE International Conference on Robotics and Automation,* San Francisco, CA, USA, 24-28 April 2000, pp. 3609-3615.

[212] M. A. Meggiolaro, P. C. L. Jaffe, and S. Dubowsky, “Achieving fine absolute positioning accuracy in large powerful manipulators,” in *IEEE International Conference on Robotics and Automation,* vol. 4, 10-15 May 1999, pp. 2819-2824.

[213] D. C. Barratt, A. H. Davies, A. D. Hughes, S. A. Thom, and K. N. Humphries, “Optimisation and evaluation of an electromagnetic tracking device for high-accuracy three-dimensional ultrasound imaging of the carotid arteries,” *Ultrasound Med Biol,* vol. 27, pp. 957-968, Jul 2001.

[214] B. J. W. Waarsing, M. Nuttin, and H. Van Brussel, "Behavior-based mobile manipulation inspired by the human example," in *IEEE International Conference on Robotics and Automation,* Taipei, Taiwan, 14-19 Sept 2003*,* pp. 268-73.

[215] D. F. Leotta, “An efficient calibration method for freehand 3-d ultrasound imaging systems,” *Ultrasound MedBiol,* vol. 30, pp. 999-1008, Jul 2004.

[216] E. C. Pua, M. P. Fronheiser, J. R. Noble, E. D. Light, P. D. Wolf, D. von Allmen, and S. W. Smith, “3-D ultrasound guidance of surgical robotics: a feasibility study,” *IEEE Trans Ultr, Ferr Freq Contr,* vol. 53, pp. 1999-2008, Nov 2006.

[217] R. D. Howe, and Y. Matsuoka, “Robotics for surgery,” *Annu Rev Biomed Eng,* vol. 1, pp. 211-40, Nov 1999.

[218] R. H. Taylor, and D. Stoianovici, “Medical robotics in computer-integrated surgery,” *IEEE Trans Robd Autom,* vol. 19, pp. 765-781, Oct 2003.

[219] C. Bertolotti, Z. Qin, B. Lamontagne, L. G. Durand, G. Soulez, and G. Cloutier, “Influence of multiple stenoses on echo-Doppler functional diagnosis of peripheral arterial disease: a numerical and experimental study,” *Ann Biomed Eng,* vol. 34, pp. 564-74, Apr 2006.

[220] A. Landry, J. D. Spence, and A. Fenster, “Measurement of carotid plaque volume by 3-dimensional ultrasound,” *Stroke,* vol. 35, pp. 864-869, Apr 2004.

[221] S. W. Hughes, T. J. D'Arcy, D. J. Maxwell, W. Chiu, A. Mllner, J. E. Saunders, and R. J. Sheppard, “Volume estimation from multiplanar 2D ultrasound images using a remote electromagnetic position and orientation sensor,” *Ultrasound Med Biol,* vol. 22, pp. 561-572, Nov 1996.

[222] S. W. Hughes, T. J. D'Arcy, D. J. Maxwell, J. E. Saunders, S. Chinn, and R. J. Sheppard, “The accuracy of a new system for estimating organ volume using ultrasound,” *Physiological Measurement,* vol. 18, pp. 73-84, Feb 1997.

[223] K. Sumiyama, N. Suzuki, and H. Tajiri, “A linear-array freehand 3-D endoscopic ultrasound,” *Ultrasound Med Biol,* vol. 29, npp. 1001-1006, Jul 2003.

[224] W. Bachta, and A. Krupa, "Towards ultrasound image-based visual servoing," in *Conference on International Robotics and Automation,* Orlando, FL, USA, 15-19 May 2006 pp. 4112-4117.

[225] A. Krupa, "Automatic calibration of a robotized 3D ultrasound imaging system by visual servoing," in *Conference on International Robotics and Automation*, Orlando, FL, USA, 15-19 May 2006, pp. 4136-4141.

[226] F. Baowei, N. Wan Sing, S. Chauhan, and K. Chee Keong, "The safety issues of medical robotics," *Reliability Eng Syst Safety,* vol. 73, pp. 183-192, Aug 2001.

[227] G. D. Hager, C. Wen-Chung, and A. S. Morse, "Robot feedback control based on stereo vision: towards calibration-free hand-eye coordination," in *IEEE International Conference on Robotics and Automation,* San Diego, CA, USA, 8-13 May 1994, pp. 2850-2856.

[228] I. Rekleitis, D. Meger, and G. Dudek, "Simultaneous planning, localization, and mapping in a camera sensor network," *Rob Auton Syst,* vol. 54, pp. 921-932, Nov 2006.

[229] J. Fischer, M. Eichler, D. Bartz, and W. Strasser, "A hybrid tracking method for surgical augmented reality," *Comput Graph,* vol. 31, pp. 39-52, Jan 2007.

[230] K. Aminian, and B. Najafi, "Capturing human motion using body-fixed sensors: outdoor measurement and clinical applications," *Computer Animation Virt Worlds,* vol. 15, pp. 79-94, May 2004.

[231] T. R. Nelson, D. H. Pretorius, A. Hull, M. Riccabona, M. S. Sklansky, and G. James, "Sources and impact of artifacts on clinical three-dimensional ultrasound imaging," *Ultrasound Obstet Gynecol,* vol. 16, pp. 374-383, Sep 2000.

[232] D. F. Leotta, and R. W. Martin, "Three-dimensional spatial compounding of ultrasound scans with incidence angle weighting," in *IEEE Ultrasonics Symposium,* Caesars Tahoe, NV, USA, 17-20 Oct 1999, pp. 1605-1608.

[233] P. Jannin, J. M. Fitzpatrick, D. J. Hawkes, X. Pennec, R. Shahidi, and M. W. Vannier, "Validation of medical image processing in image-guided therapy," *IEEE Trans Med Imaging,* vol. 21, pp. 1445-1449, Dec 2002.

APPENDIX I

US image characteristics

US images (B-mode) are characterized by the frequency of the US wave formed by the transducers, beam focusing and lense shape. The resolution of the US image and the attenuation of the US beam depend on these elements. As a general rule, a high-frequency US beam provides a better image resolution than a low-frequency beam. Conversely, the depth of beam penetration is better at lower US frequency. In large anatomical regions such as the abdomen, a lower frequency US wave ranging from 3.5-5 MHz is used to image structures at significant depth [30]. A higher US frequency is employed within the range of 7.5-10 MHz to image details situated at the skin periphery [30].

An US image is also dependant on the propagation medium, where the speed of sound varies widely in different materials [30]. The US frequency itself is not affected by changes in the sound of speed as the acoustic beam propagates through various media, but its wavelength depends on the medium. Usually, medical US scanners assume a speed of sound of 1540 m/sec for soft tissues and US wave form interactions (i.e., absorption, reflection, refraction, scattering and attenuation) that are determined by the acoustic properties of matter (i.e. acoustic impedance) [30]. Acoustic images are formed by US pulses that are reflected back to the receiver, where changes in time delay causes a texture of gray scale in the US image.

The US beam produced by the transducers propagates as a longitudinal wave into the medium and has characteristic properties that define the spatial resolution seen in US images [30]. The axial, lateral and elevational (slice thickness) dimensions define the minimal volume element in the US scan (see Fig. A.1). The axial resolution is described as the ability to discern closely spaced objects that lie in the direction of the beam, whereas the lateral resolution is depicted as the ability to distinguish small adjacent structures perpendicular to the beam's direction. The slice thickness is a measure of the beam dimension in the elevational direction (i.e., perpendicular to the image plane).

Line density, focus of the beam and artefacts are other factors that influence greatly the image quality of an US image [30]. Line density represents the spatial sampling of the

US beam that decreases with depth in sector and phase arrays but remains constant with depth for linear arrays. Generally, a large number of lines will provide a higher US image quality but compromises the frame rate. The line density can be increased in a selected region of an image with a 'write' zoom feature that can rescan details with better resolution [30]. In addition, the US beam exhibits a distinct shape pattern of a converging beam out to a distance specified by the geometry and frequency of the transducer (the near field) and a diverging beam beyond that point (the far field) (see Fig. A.1b). In a focused beam, the narrowest beam width (i.e., lateral resolution) lies at the focus depth in the scan plane and the focal zone is defined as the region over which the width of the beam is less than two times the width at the focal distance (see Fig. A.1b). Transmit focusing, where the US beam is focused at multiple depths can improve the lateral resolution in a larger region of the image because the number of focal zone is increased [30]. However, an improvement in the lateral resolution or focusing at a certain range is always accompanied by a loss of resolution in the region beyond the focal zone. Incorrect display of anatomy or noise during imaging can also degrade the diagnostic value of the US image. Different speed of sound at the boundary of two tissues can produce artefacts in the US image. They appear as misallocated or missing anatomy, high intensity changes and multiple equally spaced boundaries (i.e., reverberation) with decreasing amplitude along a straight line caused by refraction. Principally, these characteristics represent the most limitations to expect with 2D-US image.

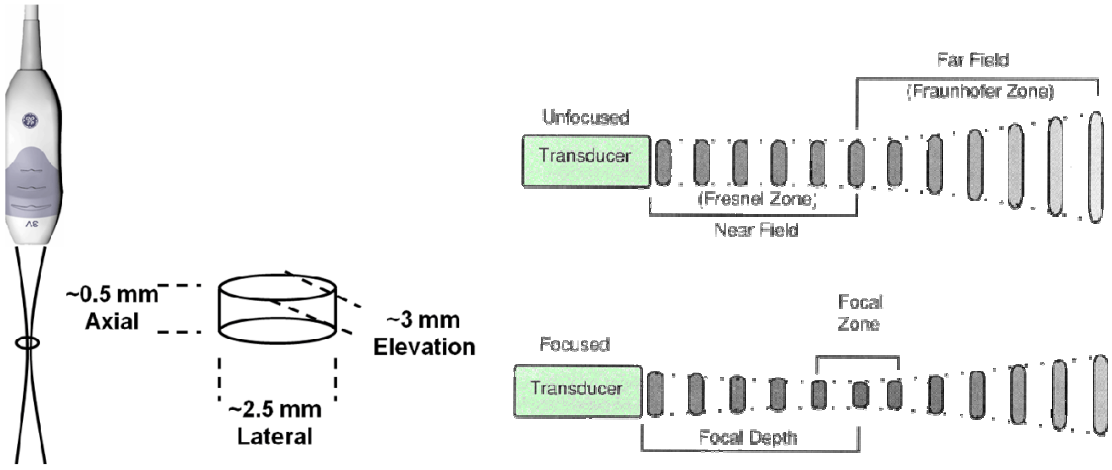

a) b)

Figure A.1 a) Resolution of the US beam in 3D space. b) The US beam pattern: focused and unfocused.[31]

[31] Source: a)http://www.escardio.org/communities/EAE/3d-echo-box/3d-echo-atlas/technical-hints/PublishingImages/Technical-factors/Axial-lateral-elevation.gif (Accessed: 10/03/2010). b) http://www.sprawls.org/ppmi2/USPRO/25USPROD08.png (Accessed: 10/03/2010).

APPENDIX II

Conference proceedings

This appendix contains 3 conference proceedings papers published for 3 different respective scientific communities. They are presented in sequential order and their references are provided below.

Janvier M.-A., Mercure É., Godbout B., Chayer B., Allard L., Bigras P., Deguise J., Soulez G. and Cloutier G., 'Evaluation of a robot's optimal performance for medical 3D-US imaging', *8th International Conference on Medical Image Computing and Computer Assisted Intervention (MICCAI)*, Palm Springs, USA, 2 pages, online, October 26th-30th 2005.

Janvier M.-A., Destrempes F., Soulez G. and Cloutier G., 'Validation of a new 3D-ultrasound imaging robotic system to detect and quantify lower limb arterial stenoses', *29th Annual International Conference of the IEEE Engineering in Medicine and Biology Society (EMBC)*, Lyon, France, pp.339-342, August 23rd-26th 2007.

Janvier M.-A., Soulez G. and Cloutier G., 'Evaluation of a 3D reconstructed lower limb vessel geometries with an ultrasound robotic imaging system', *IEEE International Ultrasonics Symposium (UFFC)*, Rome, Italy, pp. 598-601, September 20th-23rd 2009.

APPENDIX III

Authors and editors authorizations

This appendix contains the authorization from authors and journal editors to present the paper in the thesis.